Progress in electron- and ion-interferometry

2010 Rep. Prog. Phys. 73 016101

(http://iopscience.iop.org/0034-4885/73/1/016101)

Rep. Prog. Phys. **73** (2010) 016101 (43pp) doi:10.1088/0034-4885/73/1/016101

Progress in electron- and ion-interferometry

Franz Hasselbach

Institut für Angewandte Physik der Universität Tübingen, Auf der Morgenstelle 10, D-72076 Tübingen, Germany

E-mail: franz.hasselbach@uni-tuebingen.de

Received 18 May 2009, in final form 2 October 2009
Published 23 December 2009
Online at stacks.iop.org/RoPP/73/016101

Abstract

In the 1970s the prominent goal was to overcome the limitations of electron microscopy caused by aberrations of electron lenses by the development of electron holography. In the meantime this problem has been solved, not only in the roundabout way of holography, but directly by correcting the aberrations of the lenses. Nevertheless, many quantitative electron microscopical measurement methods—e.g. mapping and visualization of electric and magnetic fields—were developed within the context of holography and have become fields of their own. In this review we focus on less popular electron interferometric experiments which complement the field of electron holography. The paper is organized as follows. After a short sketch of the development of electron biprism interferometry after its invention in 1954, recent advances in technology are discussed that made electron biprism interferometry an indispensable tool for solving fundamental and applied questions in physics: the development and preparation of conventional and single-atom field electron and field ion sources with their extraordinary properties. Single- and few-atom sources exhibit spectacular features: their brightness at 100 keV exceeds that of conventional field emitters by two orders in magnitude. Due to the extremely small aberrations of diode field emitter extraction optics, the virtual source size of single-atom tips is on the order of 0.2 nm. As a consequence it illuminates an area 7 cm in diameter on a screen at a distance of 15 cm coherently. Projection electron micrographs taken with these sources reach spatial resolutions of atomic dimensions and in-line holograms are—due to the absence of lenses with their aberrations—not blurred. Their reconstruction is straightforward. By addition of a carbon nanotube biprism into the beam path of a projection microscope a lensless electron interferometer has been realized. In extremely ultrahigh vacuum systems flicker noise is practically absent in the new sources. In the context of holography, methods have been developed to record holograms without modulation of the biprism fringes by waves diffracted at the edges of the biprism filament. This simplifies the reconstruction of holograms and the evaluation of interferograms (taken, e.g. to extract a spectrum by Fourier analysis of the fringe system) significantly. A major section is devoted to the influence of electromagnetic and gravito-inertial potentials and fields on the quantum mechanical phase of matter waves: the Aharonov–Bohm effect, the inertial Aharonov–Bohm effect and its realization, the Sagnac effect and Sagnac experiments with atoms, superfluid helium, Bose–Einstein condensates, electrons and ions and their potential as rotation sensors are discussed. Möllenstedt and Wohland discovered in a crossed beam analyzer (Wien filter) an optical element for charged particles that shifts wave packets longitudinally that transverse a Wien filter on laterally separated paths. This new optical element rendered it possible to measure coherence lengths and the spectrum of charged particle waves by visibility- and Fourier-spectroscopy, to perform a 'Welcher Weg' experiment, to re-establish seemingly lost longitudinal coherence in an interferometer for charged particles and to realize a decoherence free quantum eraser. A precision test of decoherence according to a proposal from Anglin and Zurek and biprism interferences with helium atoms close the section on first-order coherence experiments. The topics of the last section are Hanbury Brown–Twiss correlations and an antibuching experiment of free electrons.

This article was invited by David J Cockayne.

Contents

1. Introduction: early developments in particle diffraction, interferometry and holography

Diffraction and interferometry of particles, in particular of electrons, have been firmly established for the past 80 years. As early as 1925 Elsasser [1] realized that Nature provided us in single crystals almost perfectly aligned interferometers also for matter waves. Experimental difficulties caused a two year delay between Elsasser's suggestion and the experimental realization in 1927 by Davisson and Germer [2]. For their diffraction experiment of electrons, periodically arranged nickel atoms of a single crystal were used. It was the first experimental proof of the wave–particle duality hypothesis established theoretically in duc de Broglie's thesis in 1924 [3] and of Schrödinger's, Heisenberg's and Dirac's revolutionary theories governing the microscopic world: quantum mechanics. In 1930 Estermann and Stern [4] already reported diffraction of neutral helium atoms by lithium fluoride crystals and in 1940 the first diffraction experiment of electrons by macroscopic obstacles was successfully realized by Boersch [5, 6] in an electron microscope. Unknowingly, Boersch's diffraction patterns, produced simply by defocusing his microscope under conditions of high coherence of the illuminating beam, were the first in-line holograms taken. In 1949 and 1951 Dennis Gabor introduced in three fundamental papers [7–9] his 'microscopy by diffracted wavefronts' or 'diffraction microscopy' in order to overcome the limitations of the electron microscope caused by geometric aberrations of the electron lenses in a roundabout way. The projection method of diffraction microscopy as originally proposed by Gabor proved to have the disadvantage of requiring very long exposure times of the order of 30 min of the holograms. Even today's state-of-the-art microscopes are not stable enough to allow these long exposure times. It has been replaced by the 'transmission method' of Haine and Dyson [10] which consists simply of taking a defocused image of the microscopic object. The experimental realization of this type of electron holography in the hands of Haine and Mulvey was extremely successful: state of the art in 1951 was according to their own words [11]. 'In our experiments, by paying careful attention to mechanical stage design and general instrument stability both mechanical and electrical, we have so far been able to obtain a resolution of 5–6 Å in the diffraction image.' And Cosslett reported at the same conference about Haine and Mulvey's experiments. 'It is claimed that a resolution of about 10 Å has been obtained already, the limitation at

the moment being as much in the reconstruction procedure as in the actual electron microscopy' and 'It is encouraging that this new method has already reached the same level of resolution as straight electron microscopy, but it appears that it is liable to be limited in the end by much the same factors: the instabilities of the instrument, rather than the aberrations of the lenses. But if these mechanical and electrical problems can be solved, it holds out a clear prospect of circumventing spherical aberration and so allowing a resolution of atomic order to be achieved' [15]. It is worth mentioning here that this remarkable success had been reached nearly ten years before the invention of the laser. The reconstruction of the holograms had to be done using light from an arc lamp monochromatized by interference filters [12–14].

At the same time work was in progress in the United States and Germany to build an electron interferometer in close analogy to the interferometers of light optics. To make a long story short, the group around Marton tried to realize a beam splitter by the use of diffraction on thin crystal lamellae [16–20] (amplitude splitting) and Möllenstedt and Düker succeeded in 1954 in the development of the biprism for electrons [21–24] (wave front splitting). The latter became the standard versatile beam splitter of variable strength in electron interferometers and electron holography microscopes while the time for Marton's delicate amplitude splitting device had become ripe when large pieces of perfect single crystals of germanium and silicon were produced for semiconductor devices and became available on the market in the early 1960s. By using the anomalous transmission of these crystals for x-rays, which was discovered by Borrmann in 1941 [26], Bonse and Hart [27] realized their famous x-ray interferometer. On the basis of these ideas Bonse and Rauch successfully developed the perfect crystal neutron interferometer [33]. It turned out to be the most versatile instrument for neutrons and unveiled many mysteries of quantum physics from the 1970s until today [28–32, 34].

It is interesting to recall that Möllenstedt's group in Tübingen not only invented the electron biprism but also succeeded in 1959 in realizing the first double- and multiple slit interferences with electrons [35, 36] with home-made miniaturized double- and multiple slit systems. Jönsson's double slit experiment was awarded to be the most beautiful experiment ever made in physics in 2002 [37].

The developmental phase of electron interferometry was followed by one concerned with its application for measurement purposes and questions of purely fundamental interest: Fresnel diffraction by circular diaphragms, by Faget and Fert [24, 25], determination of mean inner potentials [38] in solids, interference microscopy [39] or the phase shifts of electron waves by a magnetic flux [40–42] enclosed between the coherent beams were typical applications [43–46, 78] in these early days. The Brno group, Komrska, Drahos, Delong and Vlachova, contributed a consistent theoretical interpretation of the electron interference phenomena produced by an electrostatic biprism and demonstrated the validity of their model by impressive experimental interference patterns [47–50].

At the end of the 1960s Möllenstedt and Wahl's, Tonomura's and Tomita *et al* and Munch's effort to realize off-axis holography was successful [51–54]. At about the same time high brightness, highly coherent field emission cathodes were introduced into electron microscopy by Crewe [56, 55]. Simultaneously, the first electron interferometer with such a field emitter was built by Brünger [60] in Tübingen and applied to measure contact potentials [61]. This new, by many orders of magnitude brighter and more coherent electron source opened the gateway to develop a new generation of electron microscopes and interferometers, triggered the development of electron holography and the realization of experiments which were absolutely inconceivable with the old thermionic cathodes. In atom interferometry Leavitt and Bills succeeded to see single slit diffraction patterns of a thermal atomic potassium beam in 1969 [62]. Another landmark in the development of electron microscopy and electron interferometry in the early 1970s was the increasing availability of image intensifiers for civil research. In 1968 Herrmann *et al* observed with such an image intensifier the build-up of electron diffraction patterns out of single electrons [63]. In 1976 Pozzi *et al* [64] for the first time and in 1977 my student Wohland in Tübingen [65] demonstrated—in his just finished electron biprism interferometer, equipped with a home-made channel plate image intensifier—the evolution of electron interference patterns in time. The electron impact on the fluorescent screen seems to happen at random locations. However, when by the time some thousand electrons have been accumulated it becomes evident that they do not arrive at random locations but create a fringe pattern. In 1979 we observed the build-up of electron interferences at very low voltages also in our new miniaturized ultrahigh vacuum (UHV) electron interferometer and presented the new interferometer and the results at the German Conference on Electron Microscopy in Tübingen [66, 67]. Image intensifiers became a standard feature of modern electron microscopes in the 1980s and in turn the mystery of quantum interference proved by the build-up of interference fringes out of single events was reproduced in most of the laboratories around the world working on electron interferometry and holography, e.g. the Tonomura group [68] and many others. Already in 1984 we demonstrated the build-up process of electron interference fringes with our miniaturized interferometer for a whole week live to the public at the Hannovermesse [73, 74] and in 2004 in a tent at the physics exhibition 'Highlights der Physik' of the German Physical Society in Stuttgart. I want to stop here this short and by far not thoroughgoing overview. For details of developments in the field of electron interferometry until about 1987 please refer to the excellent review articles of Missiroli *et al* [69] and Tonomura [70] and the references therein. In this review we concentrate on electron interferometry and must exclude the closely related field of electron holography which has become a research topic of its own.

1.1. The Möllenstedt and Düker electron biprism (wavefront splitting)

A positively charged, electrically conductive biprism wire about 1 μm in diameter situated in the middle between two

electrodes on earth potential (figure 1) splits the wavefront which is emitted by source *s* (a demagnified thermionic source or a field emission cathode with its very small virtual source size *s*) into two parts. Since the positive charge of the biprism filament attracts the two wavefronts, they seem to emerge from the two virtual sources Q_1 and Q_2 separated by a distance *c*. Behind the biprism the wavefronts overlap and within this region form electron biprism fringes which can be detected, e.g. by magnifying the fringe system electron microscopically. Two conditions have to be fulfilled to observe biprism fringes. Firstly the spatial coherence condition, i.e. the width *s* of the source has to be sufficiently small. Secondly, the coherence length, namely the energy width of the electron source must be small enough, which is not a problem for all electron and ion emitters currently in use in electron microscopes and ion interferometers.

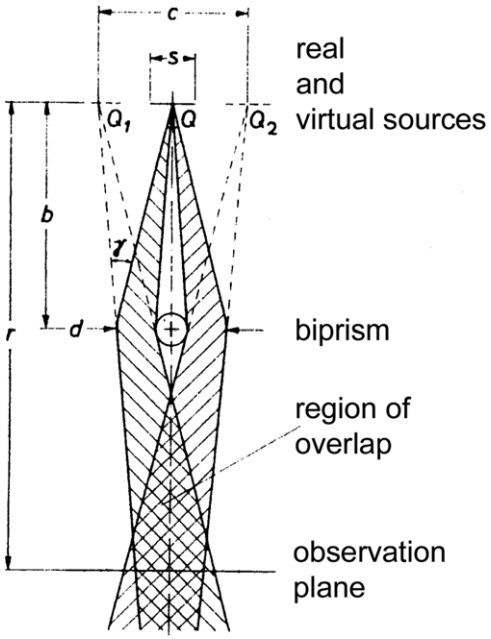

Figure 1. The electrostatic biprism. *b*: distance between source Q and biprism wire; *r*: distance between source Q and plane of observation; *c*: distance between the two virtual sources Q_1 and Q_2; *d*: the width in the plane of the biprism that has to be illuminated coherently; *s*: width of the source.

1.2. A glance at the development of electron biprism interferometers until the end of the 1980s and recent advances

Three pictures of biprism electron interferometers are given in figure 2. The first on the left-hand side (lhs) is the legendary instrument of Möllenstedt and Düker, in the middle a view of our miniaturized low voltage instrument on a turn-table (which was rotated up to 1 Hz to prove the Sagnac effect for electron waves) and on the right-hand side (rhs) the 1 MV biprism holography instrument/interferometer of Tonomura and co-workers [71]. While the first two aforementioned instruments were mainly designed as pure electron interferometers (they use astigmatic lenses and therefore are limited in recording to electron holograms in two dimensions), the 1 MV machine of Tonomura *et al* is a high resolution electron microscope with integrated biprism interferometer mainly intended for use as electron holography instrument. Today, in a large number of laboratories around the world, commercial holography electron microscopes in the 100–500 kV range equipped with biprisms are in use.

The origin of progress in electron interferometry since 1970 is mainly due to the availability of electron field emitters as high brightness cathodes, image intensifiers, highly stable power supplies, electronic image processing systems, and, for conventional electron interferometers, which are constructed according to customary principles approved in electron microscopes, active and passive vibration isolation systems.

The most serious drawbacks of conventional electron interferometers are their enormous sensitivity to mechanical vibrations and alternating magnetic stray fields. In order to

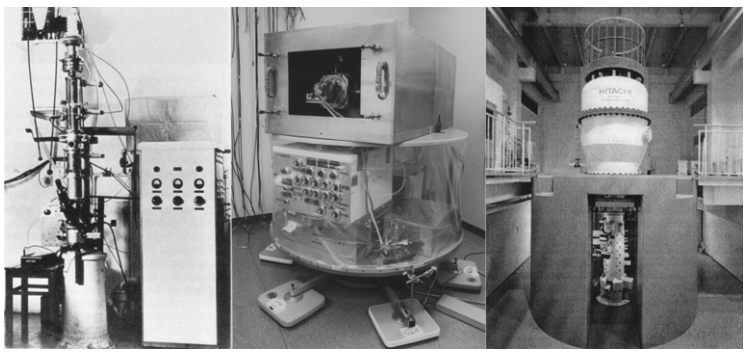

Figure 2. On the lhs an image of the first biprism interferometer of Möllenstedt and Düker is given. This first version of the instrument worked with rotationally symmetric lenses. Düker's interference fringes out of his PhD thesis which are presented in figure 12 were taken with the second version which used cylindrically symmetric lenses in order to gain intensity. In the middle the rotating Sagnac electron interferometer is presented. The interferometer is inside the MUMETAL® box which improves the shielding of the interferometer against varying low frequency magnetic fields of the order of 1 Hz caused by the rotation in the earth magnetic field. The plastic foil around the turn-table reduces the air flow around the electronics and in turn, thermal drift. The scales are used to balance the rotating masses. On the rhs the 1 MV field emission transmission electron microscope/holography instrument of the Tonomura group at the Hitachi Advanced Research Laboratory is given. (Reproduced from [71], copyright 2003, with permission from the Japanese Society of Microscopy.) By Lorentz microscopy, e.g. vortices in superconductors were studied. For interferometric and holographic experiments beam paths including up to three biprisms are available in this instrument (see section 2.6).

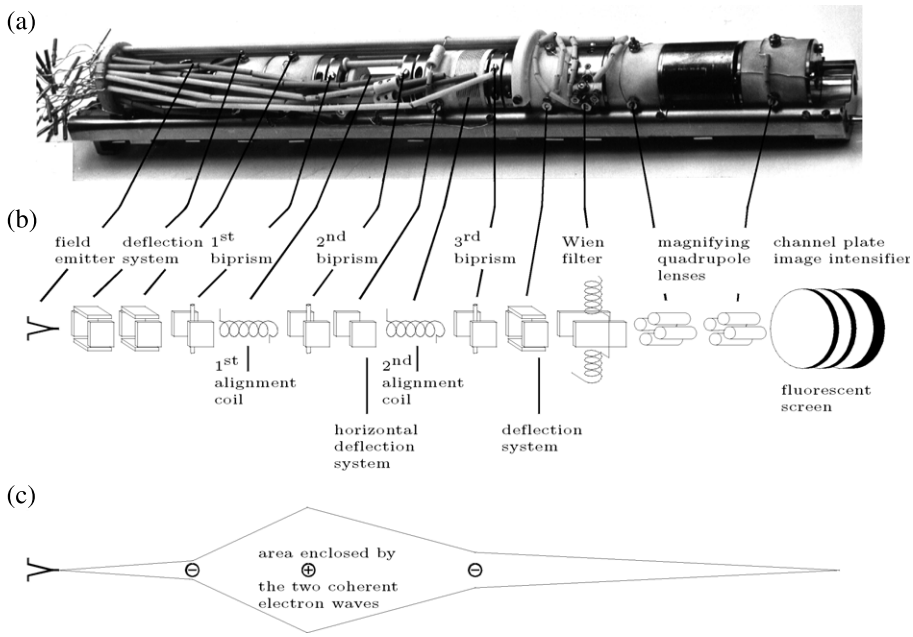

Figure 3. Miniaturized biprism interferometer. (*a*) As an example, the view of the optical components (28 mm in diameter) of our Sagnac interferometer is given. They are tightly fixed on a miniaturized optical bench (total length 30 cm) consisting of two precision ceramic rods. The image intensifier is about 20 cm away from the second magnifying quadrupole lens. (*b*) Schematic set-up. (*c*) Beam path. By three biprisms, charged negatively, positively and again negatively (–,+,–) larger enclosed areas between the coherent beams can be realized, e.g. for an Aharonov–Bohm or Sagnac experiment. In our Sagnac experiment which is discussed later, we used an arrangement of two biprisms (–,+).

overcome these deficiencies a new type of electron biprism interferometer was developed.

Analysis of the construction of conventional interferometers uncovers the following causes for their extremely high sensitiveness to mechanical vibrations and alternating stray fields: the lack of rigidity of these interferometers—equivalent to a relatively low mechanical resonance frequency—is the cause of their extreme sensitivity to mechanical vibrations. This lack of rigidity is due to the large dimensions and high masses of the interferometers—they are comparable to those of electron microscopes or are modified electron microscopes—and due to the fact that they consist of individual electron optical components, e.g. electron gun, demagnifying lenses, biprism holders, objective and projective lenses only loosely connected to each other. All these components are usually aligned by rotary feedthroughs which have an additional detrimental effect on mechanical stability and furthermore prevent from effectively shielding magnetic ac stray fields. Therefore it was the primary goal to design the new interferometer as rigid as possible, i.e. to raise the mechanical eigenfrequency of the assembly to a value as high as possible: then, external vibrations coming along the building floor cause to vibrate the interferometer as a whole of course, but the relative positions of its components are not influenced. In turn the visibility of the interference fringes is not impaired. The consequence of these considerations is that the dimensions as well as the weight of the interferometer have to be reduced drastically. The mechanical alignment of the interferometer while operating, e.g. by rotary feedthroughs has to be abandoned in favor of prealigned high precision optical components. Fine alignment has to be done exclusively by electromagnetic deflection systems and coils. The new design of an electron interferometer that overcomes these deficiencies is given in figure 3.

A full length paper with construction details of the rugged, miniature UHV electron biprism interferometer was published in 1988 only [67], shortly before we successfully realized proving the rotational phase shift of electron waves (Sagnac effect) [72, 75] with an interferometer of the new type. This experiment was the rigorous verification that all goals were reached with the new interferometer design and seemingly inconceivable investigations (e.g. a biprism interferometer for ions using matter waves [190, 191, 193] with sub-picometer wavelength) not only became possible in special laboratories but can now be realized in any environment.

2. Advances in technology

2.1. Development of bright, highly coherent sources of electrons and ions for charged particle interferometry and holography

The extraordinary high brightness of field emitters and its advantages for electron microscopy and electron interferometry were well known, at least since the invention of field electron and field ion microscopy by Müller [298] and co-workers, already in the 1950s. But, the introduction of this technology into microscopy and interferometry was not ripe until UHV became routinely available, not only in glass technology but in experimental set-ups out of metal. The first electron biprism interferometer using a field electron emitter in UHV was realized, as already mentioned, by Brünger [60] in Tübingen. The breakthrough of field emission in

electron microscopy and electron interferometry is marked by its introduction by Albert Crewe into scanning electron microscopy [55, 56]. His very first pictures with atomic resolution in a conventional scanning electron microscope from 1973 (see e.g. [59]) mark a milestone in the development of electron microscopy and interferometry. In the last three decades thermionic field emission sources without and with an emission supporting substance, e.g. ZrO, have become, due to their reliability and ease of operation, the standard choice of electron source in most commercial high resolution electron microscopes and electron holography instruments. However, these types of electron sources do not provide the ultimate possible brightness and/or are sometimes more complicated than cold field emitters, which were refined in the last two decades and ultimately developed into tips with a few atoms or only a single atom at the tip apex. Therefore we want to concentrate in this section on these more exotic field emitters with very promising features for electron interferometry, ion interferometry, microfabrication and micro-machining and other special applications.

The first step to produce a field emitter tip is to etch an oriented tungsten single crystal of about 0.1 mm diameter into a fine tip with a radius of curvature of about 50 nm (preferably (3 1 0), (1 0 0) or (1 1 1) orientation in order to obtain a high emission in axial direction of the single crystal). After cleaning this tip by heating at 10^{-10} bar in an electron field emission microscope the typical micrograph of a clean tungsten single crystal field emission pattern is observed. To use such a field emitter without further processing is not recommended when the highest possible brightness is indispensable for the experiment. A clean tungsten tip emits electrons into a large angle on the order of 20° while only electrons emitted in angles of less than $(10^{-2})^\circ$ are accepted by electron optical instruments. Therefore, in order to achieve a confinement of the emission into small angles of 2° or less by manipulating the surface morphology of the tip, the following procedures have been developed:

- optimizing of cold field electron emitters by remolding (initiated by thermal self-diffusion in an electric field);
- oxygen induced sharpening of field emitter tips;
- sharpening of field emitter tips by sputtering with heavy ions;
- preparation of ultrasharp single- or few-atom tips;
- noble metal coated W(1 1 1) single-atom tips;
- 'super-tip' field electron and gaseous field ion sources (GFIS):
  - (a) (super-)tips produced by surface self-diffusion intiated by H_2^+ or He^+ ion impact at elevated temperatures of the tip;
  - (b) thermodynamically stable, pyramidal, single-atom super-tips formed by faceting of noble metals on W(1 1 1);
- novel applications of carbon nanotubes: as electron field emitters, for coherent and intense electron multibeam generation and as electron biprism.

Albert Crewe used in his famous scanning microscope with atomic resolution [57–59] a remolded field emission electron source [55, 56, 246] at room temperature. In the *remolding process* the initially rounded state of the field emitter tip is transformed into a faceted one by a temperature variation of the tip while a strong electric field is simultaneously applied to the tip. Surface migration of atoms is made possible due to elevated temperature and, because, due to the strong electric field, the atoms acquire a dipole moment and drift in a direction along the field gradient. This reforming process of the tip works independent of the direction of the electric field applied to the tip. In order to avoid a sudden and uncontrollable onset of field emission of the tip, the process is usually performed with a *positively* charged tip. The progress in the remolding procedure is again and again controlled by switching the tip polarity from positive to negative and observing the electron field emission pattern [280]. When a bright single spot pattern is achieved, the remolding process was successful and the cathode is ready to be used. Remolding is performed *in situ* and can be applied many times to reshape the cathode (if the tip has not become too blunt when accidentally damaged) since the process is reversible. It has been shown that it is even possible to automate the remolding process of a field emitter in an electron optical instrument if there exists the possibility to switch the electron optics into such a condition that during the remolding process at least a part of the field emission pattern can be observed. A simple image processing system [247] then allows computer controlled remolding.

2.1.1. Oxygen induced sharpening of field emitter tips and sputtering with heavy ions. These [248] are further choices to prepare field emitters. Modifying field emitter tips by heating them in oxygen atmosphere and removing the oxide by subsequently heating again in a vacuum was already reported by Müller [249] in 1938. This process has been improved, e.g. by Veneklasen and Siegel [250], Binh *et al* [251] and Kim *et al* [252]. In their search for stable, high intensity field ion sources Kubby and Benjamin Siegel [253] used ion milling for sculpting the surface contour of polycrystalline and oriented tungsten tips. They showed that on the initially parabolic surface of the etched tip, a protrusion with much smaller radius of curvature is produced by the sputtering process. The field emission pattern of such a microtip on a more blunt tip emits charged particles (both electrons and H_2 field ions) not only into a single spot but the spot is additionally confined into a much smaller angle enclosing a few degrees to a fraction of a degree only—caused by the modified distribution of the electric field in front of such tips—with the consequence of a large gain in brightness.

2.1.2. Ultrasharp single-atom tips. They were developed by Fink [281, 282] in order to overcome the problem of convolution, intrinsic in all scanning tunneling micrographs taken with standard tips, which end in a large number of atoms. Apart from this benefit for scanning tunneling microscopy their additional application as nearly ideal point sources for field electrons and field ions was realized. The angular emission cone of these sources is about 0.5° for ions and 2°

for electrons, respectively. The confinement of the emission current into such small angles is caused by the fact that the micro-protrusions are artificially built up on comparatively blunt (1 1 1) oriented tungsten tips. The local distribution of the electric field in front of such a tip confines the charged particles which leave the surface of the mono-atomic protrusion in larger angles into the just mentioned small angles. With a trimer tip, i.e. a tip ending in three atoms, stable total currents as large as 10 μA of electrons could be drawn without destruction of the tip. The atomic size emission area, the small angular divergence, the high brightness and the corresponding high coherence opened a gateway for new experiments especially in electron and ion interferometry, electron holography, low voltage projection microscopy, and improved the resolution of the topografiner of Young *et al* [317]—which is a precursor of the scanning tunneling microscope—by two orders of magnitude to 3 nm. The topografiner is a scanning, non-contacting instrument for measuring the microtopography of metallic surfaces. Its prototype achieved a resolution of 3 nm perpendicular to the surface and 400 nm in the plane of the surface. It consisted of a fine electron field emisson tip which is brought close to a conducting surface while a constant current is being passed through the emitter. The voltage between the emitter and the surface is amplified and applied to the piezoelectric element on which the emitter is mounted. This forms a servo system which keeps the emitter at a constant distance above the surface. The piezo voltage corresponds to the altitude of the surface. Two additional piezo elements scan the emitter over the specimen surface and generate a topographic map. Characteristic for the topografiner—as for the tunneling microscope—is that the probe does not contact and in turn damage the surface. At large spacings between the probe and the surface the measured field emission current is in agreement with the Fowler–Nordheim theory. When moved within 3 nm from the surface it is compatible with Simmon's theory of metal–vacuum–metal tunneling [318].

2.1.3. Preparation of single-atom tips. In order to obtain tips as sharp as possible, Fink has chosen the (1 1 1) tungsten surface to be the apex plane of the tip. This plane is small in size due to its relatively high surface free energy and is the best starting point for the preparation of a single-atom tip. In the first step, by field evaporation a defect-free surface is created and then successively single atoms at the edges are field evaporated until a plane containing only three atoms is reached. The last atom on top of this trimer is deposited out of the gas phase by a tungsten evaporator. Each step of construction of a single-atom tip must be controlled by imaging the surface status of the tip apex, layer by layer in the field ion imaging mode in order to be able to advance to the next step. The angular divergence of such a monoatomic point source amounts to less than 0.5° for ion and 2° for electron emission. The preparation of these tips is a tedious process and needs a lot of experience. The detailed procedures are described in [281, 282].

In his 1986 paper, Fink [281] already mentions that single-atom tips can be created—however, not in a routine way—by self-diffusion of W atoms by annealing at roughly 1500 K and stopping the evolution after a time on the order of few seconds just at the right moment. Binh and Garcia [284] developed this method into their field-surface-melting technique: an electric field is applied to a W(1 1 1) tip or a non-oriented Au tip at temperatures of about one-third of the bulk melting temperature. The W protrusions produced end in one atom and are of approximately 2 nm in height on top of W-based tips of 70–100 nm radius. These sources can emit *coherent metallic ion and electron beams*.

Surface melting is governed by the two parameters temperature T and electric field strength F. The temperature T acts over the whole body, while F acts only on the surface atoms (either their permanent and/or induced dipole moments) and reduces the activation barrier for surface diffusion. On a perfectly flat, densely packed surface the reduction of this activation barrier is negligible. However, when the surface is rough with steps and vacancies the atoms at these irregularities encounter higher forces. In a region of the surface with only a few defects the few moving atoms will smooth out the surface roughness. In an area with a large number of defects the reduction of the activation barrier by the electric field will be much higher, field surface melting will occur and nano-protrusions can be formed, and due to the field enhancement on top of such a protrusion, single-atom tips may be generated. For an appropriate choice of strength of the electric field F and temperature T of the tip it is possible that the topmost atom is field evaporated and simultaneously this topmost atom is replaced by another one. This combination of field evaporation and field surface melting leads to a *continuous stable metal ion emission*. Beam intensities of about 10^5–10^6 W ions s^{-1} with a beam opening of about 2° were realized. After cooling and reversing the electric field, high-brightness electron beams of up to 0.1 μA collimated to 4° are available.

Another method of field-enhanced diffusion growth of nanotips is given in the paper by Nagaoka *et al* [254]. It works in full analogy with the just described method. The difference is that the formation of the tips takes place at room temperature and the material of the nano-protrusion consists of adsorbates which are gathered by the high electric field. The total energy distribution (TED) of these tips differs from the normal Fowler–Nordheim theoretical curve and shows two peaks. The reason for this behavior is given in the next paragraph.

In his 1988 paper [282] on single-atom tips Fink raises the question whether the TED of electrons from single-atom tips *which are confined inside the field emitter before emission into a volume of atomic dimensions differs* from the spectra recorded for macroscopic tips where the electrons are confined on the apex of the tips to not less than about 3 nm. Binh *et al* found in 1992 [283] that the TEDs of their single-atom tips which were prepared by using the field-surface-melting method consisted of well-separated peaks which shifted linearly with increasing extraction voltage (figures 4(*a*) and (*b*)). Additionally, their full width at half maximum (FWHM) was independent of the extraction voltage and the spectra could not be fitted with the classical equation for the tunneling current from a metal. All these features are not present for conventional macroscopic tips. Controversial discussions arose since at least four other groups observed ordinary field emission behavior for ultra sharp (1 1 1)-oriented

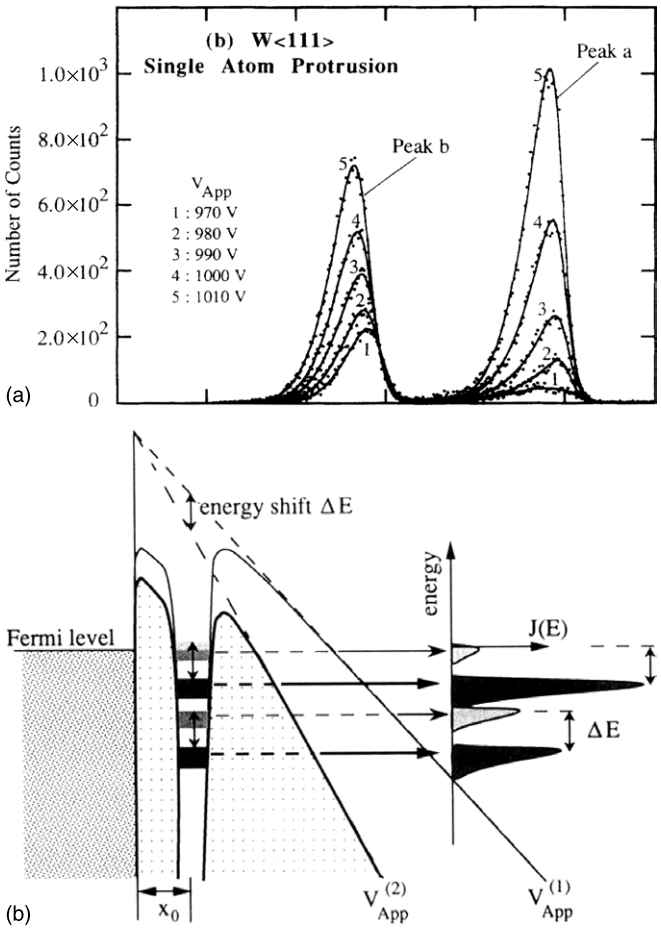

Figure 4. (*a*) Typical TEDs of electrons emitted from single-atom protrusions with increasing extraction voltage. The two peak structure becomes more and more pronounced as the length of the protrusion increases. (*b*) The linear shift of the spectra with increasing extraction voltage can be understood by considering the simplified model of field emission from single-atom tips for two values of the extraction voltage V_{App}. The lightly shaded bands and spectra (on the rhs) correspond to the lower extraction voltage $V_{App^{(1)}}$. The black ones are the same bands after they were shifted by increasing the extraction voltage to $V_{App^{(2)}}$. For details see [283]. (Reproduced from [283], copyright 1992, with permission from the American Physical Society.)

tips. New evidence for multiple-peaked TEDs from single-atom tips using the build-up process of Binh *et al* was reported by Yu *et al* [285] in 1996.

The puzzle about the TEDs was resolved by a theoretical paper of Gohda and Watanabe [286]. They found that multiple peaks become more and more pronounced as the size of the single-atom terminated protrusion becomes more extended in length, e.g. consists of 14 atoms instead of 5 atoms. The well-separated peak below the Fermi level observed by Binh *et al* can be attributed to the difference in size of their single-atom terminated tips and is caused by the existence of localized states at the topmost atom and the local potential barrier reduction in front of the topmost atom. In their reply on the 'comment on field-emission spectroscopy of single-atom tips' Binh *et al* write 'We are not surprised with their experimental results because the height of the protrusion is the crucial parameter in determining the emission characteristics...', which was confirmed by the results of Gohda and Watanabe.

2.1.4. Generation of thermodynamically stable single-atom tips. Another, rather promising direction in the development of single-atom tips was initiated by the experimental investigations of Crewe *et al* [57], Madey *et al* [290, 291, 295], Williams and Bartelt [293] on the stability of ultrathin metal films on W(1 1 0), W(1 1 1) and Mo(1 1 1) surfaces and the theoretical studies of ultrathin film-induced faceting on W(1 1 1) and Mo(1 1 1) surfaces covered with Pd, Pt and Au by Chen and Che *et al* [292, 294].

It is well known that metallic bcc (1 1 1) surfaces undergo faceting when certain *gases* are adsorbed. Recently, such an overlayer induced faceting has been observed also for various *metallic* overlayers on bcc substrates (figure 5). The energetics of the adsorption is crucial for the growth of pseudomorphic layers of different fcc metals, e.g. Au, Pd and Pt on W(1 1 1) and Mo(1 1 1) [294]. Since the [2 1 1] direction makes the smallest angle with [1 1 1]—and in turn the smallest increase in surface area (6% only)—it is natural for the (1 1 1) surface to facet to (2 1 1), i.e. into pyramids exposing three equivalent facets of {2 1 1} surfaces, provided that {2 1 1} has lower surface energy and that the energy anisotropy is large enough to compensate for the increase in surface area. That is, by adding a monolayer of, e.g. Pt on a clean W(1 1 1) surface this system becomes thermodynamically unstable and at elevated temperature the mobility of the surface atoms increases. In turn the Pd-covered W(1 1 1) surfaces facet upon annealing into Pd-covered W(2 1 1) facets since (2 1 1) is now lower in energy even after taking into account the area increase due to faceting. The pyramids are made up of the W atoms coated with a monolayer of Pt atoms (the increase in the surface energy for {0 1 1} faceting on a bcc(1 1 1) surface is 22%. Therefore it occurs sometimes in addition to the energetically more favorable {2 1 1} faceting).

The experiments on faceting described till now were performed on planar surfaces, not on sharp tips ending in an (1 1 1) plane. This faceting process suggests the creation of atomically perfect three-sided pyramids a few nanometers in size ending in a single atom on the (2 1 1) face of a W field emitter tip. In contrast to the field and thermally induced tip forming processes, the new procedure has the advantage that thermodynamically stable single-atom tips, which are spontaneously formed by annealing, are the result. The procedure is very simple, and—due to the natural thermodynamic driving force of faceting—the tip can be routinely regenerated many times by removing the top few layers by field evaporation and annealing at 1000 K for a few minutes. Details of the creation and the characterization process of such tips were published from 2001 on by the group of Tien T Tsong [255, 257]. The state of the art is presented in [258]. In the early days the W(1 1 1) tip was covered by a Pd monolayer which was deposited by evaporation of well-degassed Pd *in situ*. The state of the art is now to deposit Pd or Pt on the W(1 1 1) single-crystal tips in a liquid process by electroplating followed by a final vacuum process: thermal annealing to about 1000 K for 10–20 min *in situ* until the emission angle of the electrons shrinks into an angle of about 5°–6°. The long annealing time is necessary since by electroplating a rather thick noble metal layer is deposited on

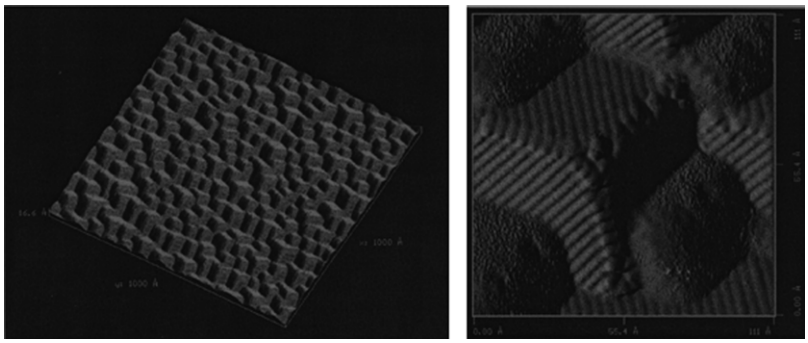

Figure 5. Scanning tunneling microscopy (STM) image of a completely faceted W(1 1 1) surface induced by an ultrathin Pd film (∼1.2 ML) upon annealing to 1075 K for 3 min, forming three-sided pyramids with {2 1 1} facets. The dimensions are 1000 × 1000 Å^2 and the vertical scale is 16.6 Å. On the rhs a STM image of a faceted Pd–W(1 1 1) surface with a coverage of ∼1.5 ML. The dimensions are 110 × 110 Å. The atomic row and trough structure demonstrates the bcc{2 1 1} facets. (Reproduced from [295], copyright 1999, with permission from Elsevier.)

the tip. The noble metal atoms migrate to the shank of the tip until a monolayer is left. Then the three-sided pyramidal tip with {2 1 1} facets is spontaneously formed. A formidable advantage of the new type of field emitter tips is that the vacuum process can be performed either *in situ* in the electron optical instrument or in a special preparation chamber. From this chamber the fully prepared tip can be transferred through air into the final instrument.

The brightness of such an electron source at 100 keV is estimated to be on the order of 10^{13} A m^{-2} sr^{-1} at a beam current of ∼1 nA, which is at least an order of magnitude larger than that of conventional field emission electron sources. However, in the energy spread, which was measured for a Rh–W(1 1 1) tip, an additional shoulder at 0.8 V below the Fermi level is present, which reminds us of the behavior of the single-atom tips of Binh *et al* [283]. The emission of electrons from the tips is highly stable. Step like spikes only occur when an atom is adsorbed near the topmost atom of the tip.

Only recently field emission spectra of single-atom tips, trimer and decamer tips with such thermodynamically stable nanopyramids with three {2 1 1}-faceted sides at the tip apex out of Pd, Pt, Ir or Rh at 55 K have been measured in detail by Rokuta *et al* [273] in comparison with a spectrum of a tungsten microtip. These current spectra did not include either peculiar features attributable to resonant tunneling or electric field penetration. They showed no significantly narrow energy width and behaved rather like conventional metallic field emitters at low electric fields as explainable within the Fowler–Nordheim theory. For single-atom tips and trimers humps appear in the spectra. Anyway, the Fermi level peak remains dominant in any spectra regardless of the coating material, the electric field or the termination of the tips. The field depending growth of the humps is in accordance with the predictions of Gohda's theory [286–288].

2.1.5. Carbon nanotube field electron emitters. Shortly after the discovery of carbon nanotubes it was suggested they have potential as an electron field emitter. The energy distribution from multiwalled carbon nanotubes (MWCNTs) has been measured [297] and was found to be extraction voltage dependent with a FWHM ranging from below 200 mV up to about 800 mV. The stability of emission is remarkable when compared with conventional cold field emitters; however, the emission characteristics proved to be strongly sample dependent. This may be the reason that carbon nanotube electron sources have not yet found broad applications in electron interferometry and electron microscopy. High brightness luminescent elements, x-ray tubes, cathode ray lamps and flat displays are already on the market [296]. Active research is going on to produce nanotube electron sources and arrays of sources reproducibly with the desired features which make them suitable for high resolution electron beam instruments.

2.1.6. GFIS for ion interferometry, ion optical applications and micro-machining. The field ion microscope (FIM) invented by Müller in 1956 [298] was the first optical instrument which achieved atomic resolution. The atoms of an imaging gas are ionized in front of a fine tip which is on a high positive potential and cooled down to a few tens of kelvins. Field ionization is achieved by tunneling of an electron of an imaging gas atom into a protruding atom of the metallic tip. The imaging gas atom becomes an ion and is accelerated in the high electric field apart from the tip toward the viewing screen. Every single protruding atom of the tip surface forms an image spot on the screen. The beautiful field ion images (figure 6) showed for the first time that the surface of the metallic tips corresponds one to one to the hard ball model which crystallographers had constructed to help our imagination.

The working principle of the FIM is the basis also for the GFIS [299, 300] which were developed from the early 1980s until now. The idea behind the development of GFIS is to take a FIM and change its features in such a way that field ions are produced not in front of all or a large number of surface atoms of the tip but *all field ions are formed in front of a few or even a single atom* of the tip. The intrinsic atomic resolution capability of the FIM guarantees that all field ions seem to originate from a virtual source with a lateral extension on the order of a single atom or less ensuring excellent lateral coherence. These extraordinary features of the ultimate GFIS are the product of a very low spherical aberration of the electric field directly in front of the tip and the narrow

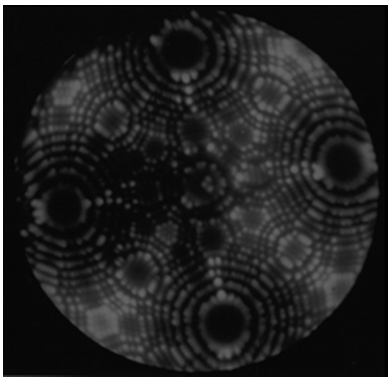

Figure 6. Field ion micrograph of a [0 0 1] oriented single crystalline tungsten tip with three atoms on the (0 0 1) face on the apex of the tip [301].

energy distribution of about 1 eV only, generated by the field ionizing process in combination with the small total current in the ion beam which avoids detrimental anomalous broadening [304–306] of the energy spectrum of the field ions and the corresponding loss in longitudinal coherence.

A first hint on how to realize a single ion-emitting spot appeared in the study of the initiation of electrical discharges in a vacuum by Cavaillé and Drechsler [302, 303]. It led to the hypothesis of the existence of surface self-diffusion by ion impact, i.e. as a result of bombardment of the tungsten surface, e.g. by hydrogen ions, tungsten surface atoms are rendered mobile and protrusions are built up under the influence of the electric field. In turn, bright spots in field ion micrographs are observed. The substance of the protrusions was identified as tungsten, because the bright spots disappeared in the absence of an electric field only at temperatures exceeding 1200 K where thermal surface diffusion of tungsten occurs. The next goal on the way to GFIS was to grow a small but relatively high protrusion on a relatively blunt field emitter tip in order to reach the goal that field ionization of the imaging gas takes place only in front of this protrusion. The first GFIS of this type were developed by Schwoebel and Hanson [307–310] followed by the group around Kalbitzer [311–316]. They intended to replace the liquid metal sources in focused ion beam (FIB) systems. The ion optical performance and in turn the beam focus diameter of these systems would, due to the low energy spread of ∼1 eV, the small virtual source size on the order of 3 nm and values of brightness of 10^9 A cm^{-2} sr^{-1} of the GFIS, outperform systems with liquid metal ion sources (LMIS). More details on the growth of protrusions—in Kalbitzer's terminology 'supertips'—and their current stability and the handling of these sources are available in the cited literature. A supertip grown on an (1 1 1) base tip has been imaged by the Kalbitzer group by FIM with atomic resolution [316]. It is not amorphous but consists of a nanocrystallite of a few nanometers in diameter and a height of about six atomic layers. The ultimate development of a GFIS would be to use—likewise as for field electron emission—a noble metal covered W(1 1 1), faceted single-atom tip developed by Kuo *et al* [258]. The ionization of the imaging gas takes place in front the topmost atom of a pyramid with three {2 1 1} surfaces. These thermodynamically stable single-atom tips have the potential to become the ideal ion sources for field ion beam (FIB) systems. Compared with LMIS their source size is two orders of magnitude smaller. Their emission angle is on the order of less than 1° only and the total emission current several orders of magnitude smaller than that of LMIS. Thus the effect of Coulomb interaction is negligible. In turn, the energy spread as for the older types of GFIS will be much lower than that of LMIS. The brightness of these sources estimated from their Ne ion emission is on the order of 1×10^{11} A m^{-2} sr^{-1} which may be improved by two or three orders according to Kuo *et al* [258]. Metal-field ion sources are expected to become possible as well. The features of noble metal-W(1 1 1) faceted single-atom electron and ion sources are compared with already available sources in tables 1 and 2 which are reproduced from the just mentioned article of Kuo *et al*. The outstanding features of the GFIS are the reason that the key benefits of *scanning ion microscopy* compared with the scanning electron microscope [275] have been rediscovered and a high resolution instrument with such an ion source is in development. First results by Scipioni *et al* and Morgan *et al* may be found in [276, 277]. Details of the GFIS and of the scanning ion microscope of these authors are given in their US Patents [278, 279]. According to these Patents the preparation of their GFIS seems to involve techniques similar to those given in this section of this review.

2.2. Coherence and noise characteristics of the new electron field emitters

2.2.1. Longitudinal coherence. While the energy width of a field emitter on the order of an electronvolt would allow one to observe many thousand fringes in an electron biprism interferometer, the lateral dimensions of the source limits the number of visible fringes to a much smaller number than that given by the longitudinal coherence. Nonetheless highly monochromatic electron beams are of interest in electron interferometry, electron wave based spectroscopies (see section 3.5.2.) and are helpful in many experiments. Refraining from using a monochromator, cooling the field emitter is a choice to obtain a narrower energy width of the emitted electrons [262, 261]. Another choice is the highly monochromatic electron beams which are predicted to be emitted from a superconductor into vacuum [260]. Such a source of electrons has been realized for the first time recently by combining a cryo-field emission gun with a niobium tip at 4.2 K at extremely high vacuum and an electron energy analyzer by Oshima and co-workers [259]. At 4.2 K an extra sharp peak from the Bose–Einstein condensed Cooper pairs appears superimposed just at the Fermi energy on the Fowler–Nordheim spectrum. Below the superconducting transition temperature of 9.2 K of niobium the height of this peak increases with decreasing temperature. The peak is extremely sensitive to adsorbates. Even at vacuum pressures of 10^{-10} Pa the peak intensity tends to reduce with time, and finally disappears, i.e. the tail of the superconducting wave function penetrates through the clean apex to the vacuum but not through contamination layers. The measured energy spread of the electrons of ∼20 meV (by BCS theory ⩽0.1 meV is expected)

Table 1. Characteristics of various electron sources: LaB^6, Cold Field Emission tungsten (CFE W) and Single-ATom (SAT) source. (Reproduced from [258] p 8980, copyright 2006, with permission from the Japanese Journal of Applied Physics.)

Electron source	Unit	LaB_6[a]	CFE W[a]	Sat
Log brightness	$A\,m^{-2}\,sr^{-1}$	10	13	16[b]
Crossover size	μm	10	0.01	0.0002
Energy spread	eV	1.5	0.3	0.4[b]
Vacuum	Pa	10^{-4}	10^{-8}	10^{-8}
Maintenance		—	Frequent flashing ~5000 K	Repeated annealing ~1000 K
Lifetime	h	500	$\geqslant$1000	~100 regenerations

[a] Adopted from Williams D B and Carter C B 1996 *Transmission Electron Microscopy* (New York: Plenum) p 77.
[b] Oshima C *et al* 2005 *e-J Surf. Sci. Nanotechnol.* **3** 412.

Table 2. Characteristics of various ion sources: plasma source, liquid metal source (LMIS), gaseous field ion source (GFIS) and single-atom tip (SAT). (Reproduced from [258] p 8982, copyright 2006, with permission from the Japanese Journal of Applied Physics.)

Ion source	Unit	Plasma source	LMIS	GFIS[a] (H_2, 2×10^{-2} Torr)	SAT[b] (Ne, 2×10^{-2} Torr)
Semiangle	°	—	30	45	1
Ang. intensity	$\mu A\,sr^{-1}$	3×10^{-3}	20	1	2
Source size	nm	$\sim 3 \times 10^4$	100[c]	~1	~0.2 (single atom)
Brightness	$Am^{-2}\,sr^{-1}$	1×10^6	6×10^8	3×10^{11}	1×10^{13}

[a] Angular intensity is calculated from the sensitivity of 5×10^{-5} A sr^{-1} $Torr^{-1}$, obtained in Orloff J H and Swanson L W 1975 *J. Vac. Sci. Technol.* **12** 1209. This value is valid when an Ir normal tip is used in a hydrogen atmosphere over the range 3×10^{-4}–2×10^{-2} Torr.
[b] Angular intensity is estimated from the sensitivity of 8.5×10^{-5} A sr^{-1} $Torr^{-1}$.
[c] This value was assumed in Ward J W and Seliger R L 1981 *J. Vac. Sci. Technol.* **19** 1082.

is either due to the energy resolution of the spectrometer or to imperfections of the niobium tip. This electron source is not yet ripe for application, but hopefully can be developed into an ultra monochromatic source in future.

2.2.2. Spatial coherence. Oshima and co-workers took a projection microscope working at about 100 eV consisting of a polycrystalline tungsten field emitter tip, a fluorescent screen and a micro-biprism positioned with a 3D-adjusting system at a very small distance in front of the field emitter [263, 264] (see figure 10 in section 2.4). The electrostatic biprism consisted of a multiwalled carbon nanotube (MWCNT) which is deposited on a holey carbon grid and divides the electron wavefront and, at the same time, deflects the two wavefronts so that they overlap. As a result high quality interference fringes are produced on the fluorescent screen without any magnifying lenses. From the visibility curves the value of the transverse coherence ξ_T in the plane of the fluorescent screen is obtained. For different emission sites on the tip ξ_T varied in the range 10–20 mm, which yields, via the van Cittert–Zernicke theorem, effective source sizes of 0.4–0.7 nm. For the conventional tips with a tip radius of 50 nm Cho *et al* notice 'that the virtual source sizes have surprisingly small values, which indicated that the tips are partially coherent sources'. And 'in this regard, we point out that the reduced coincidence rates observed by Kiesel *et al* [361] could originate from anticorrelation during coherent tunneling'. After cooling down the tip to 78 K, the number of visible fringes increases as well as their visibility. ξ_T increases to 70 mm or more. Oshima and co-workers ascribe this to the fact that the inelastic mean free path ξ_{in} of the conduction electrons in tungsten increases with decreasing temperature because of the reduction of phonon scattering which is responsible for an even smaller effective source size. Hopefully, the experiments which are in preparation at 5 K will shed even more light on this up-to-date physics problem.

Oshima *et al* continued their research with a newly developed low temperature field emission system [269] dedicated for the development of ultra coherent electron beams in 2004. It consisted of a combination of a preparation chamber and a very sophisticated low temperature field electron emission microscope (FEM) allowing the following modes of operation down to 5.5 K: field electron microscopy (FEM), projection microscopy (PM), field ion microscopy (FIM) and scanning tunneling microscopy (STM). With this system Oshima and co-workers observed interference fringes of electrons in *field emission patterns* of MWCNTs (figure 7(*a*)) at 60 K [267]. A field ion microscopical (FIM) investigation of the end caps of the nano tubes showed four tiny protrusions 1–2 nm in diameter (figure 7(*c*)). Consequently, these four protrusions emit electrons. One expects four bright spots on the fluorescent screen. Remarkably, just in the middle between these expected bright spots lines appear which were identified by Oshima *et al* as Young's interference fringes figures 7(*a*) and (*b*). The reason for this observation is that the end caps of the carbon nanotubes are so small and consequently, the four micro-protrusions are so close to each other that the coherent electronic states near the Fermi level spread over the emission area of neighboring emission sites, the

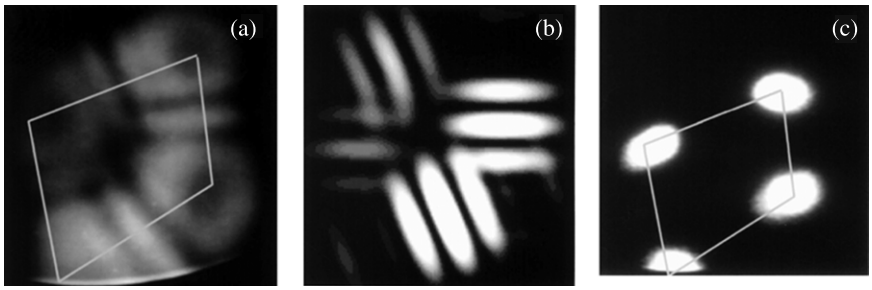

Figure 7. (*a*) Field electron emission patterns of MWCNTs at 60 K. An analysis of the end caps of the MWCNT by field ion microscopy (*c*) showed four tiny protrusions on these end caps which are responsible for four electron emission sites visible in (*a*) and (*b*). The bright lines which are clearly visible in between the spots are Young's interference fringes. In (*b*) the calculated interference pattern under the assumption that the four sites are coherently emitting electron waves is presented. (Reproduced from [267], copyright 2002, with permission from the American Physical Society.)

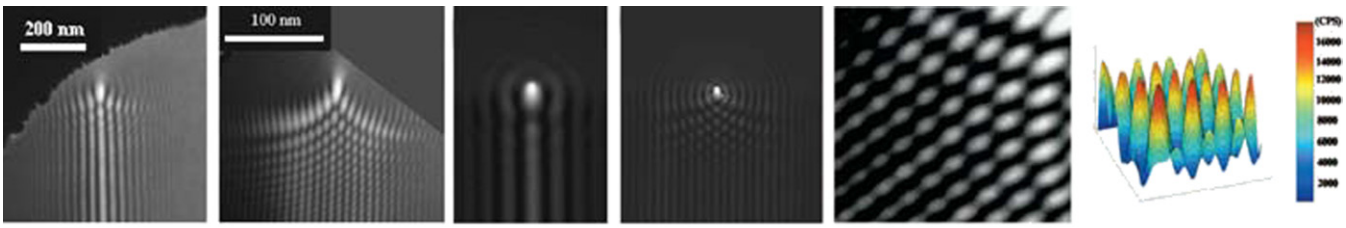

Figure 8. Real (*a*), (*b*) and calculated (*c*), (*d*) defocused electron projection images of carbon nanotubes at 77 K including their end caps are presented at low (*a*) and high (*b*) magnifications. The characteristic candle-like patterns at the ends are clearly visible and are readily described by the scalar diffraction theory. Promising applications of the large number of coherent spots (given in (*e*) and (*f*)) in future e-beam lithography systems and electron interferometers are obvious. (Reproduced from [270], copyright 2007, with permission from the American Institute of Physics.)

(This figure is in colour only in the electronic version)

emission sites emit electrons coherently and in turn interfere with each other. This effect has been considered in 1990 by Summhammer *et al* [268].

Field electron emission *projection images* of MWCNTs taken at 77 K in figure 8 show biprism fringes on both sides of the MWCNTs and at the end of the nanotube a 'candle-like' pattern made up of diffraction spots [270]. At low magnification the fringes seem to go around the end cap (figures 8(*a*) and (*c*)). When the nanotube would end not in a sharp tip, but in a hemisphere with the diameter of the MWCNT, the fringes would go around this hemisphere. The candle-like pattern made up of single dots appears when the hemisphere is replaced by a conducting hyperboloid surface. These diffraction patterns can be readily described by the scalar diffraction theory [271]. The visibility of the coherent spots in such a multibeam array produced by the apex of the nanotube was on the order of $\leqslant 0.8$ and the intensity in the spots was homogeneous. At a total current of the illuminating e-beam of a few microamperes such a multibeam generator can generate multiple coherent beams of $\leqslant 1$ nA in each single beam which might be focused onto sub-nanometer spots using a state-of-the-art electron lens. Therefore, the high coherency of the individual beams in the multibeam and the coherence of the beams to each other open promising applications in future e-beam lithography systems and electron interferometers.

2.2.3. Low frequency flicker noise and shot noise current fluctuations of field emission. In state-of-the-art cold field emitter electron guns, the noise and current fluctuations are dominated by flicker noise and are on the order of a few percent. Cho *et al* [272] study in their new extreme high vacuum (XHV) field emission microscope at vacuum down to 7.5×10^{-10} Pa the noise characteristics of W(1 1 1) tips at 90 K. For field emission electron sources widely in use, the operation pressure is in direct relation to the intensity of the flicker noise. The gas molecules in the residual gas in vacuum cause the fluctuations of the field emission current through surface kinetics such as diffusion, adsorption, desorption, etc. The excellent vacuum in the XHV-FEM was obtained by extremely careful choice of the materials, prebaking and degassing the components in a vacuum furnace, removing surface oxide layers from the tungsten tips by heating and by electron bombardment in vacuum. A special extractor electrode cut from a thin tungsten foil is heated to 1650 °C, degassed and emits electrons which are accelerated and strike nearby parts and degas the surfaces by stimulated desorption. During field emission the apex of the field emitter has only surfaces in its sight that are cooled down to liquid nitrogen temperature. The residual gas in the well-degassed XHV-FEM was composed of more than 99% of hydrogen. As a result at a vacuum of 7.5×10^{-10} Pa the saturation of an initially clean surface due to the adsorption of residual gas molecules needs much more that 1000 min and, having in mind the large amount of hydrogen adsorption after that time, one may expect large flicker noise. Nonetheless, at a current of 2 nA it was 0.1% only compared with 1–3% in a conventional FEM. For the initially clean surface the fluctuation of the current was 0.01%

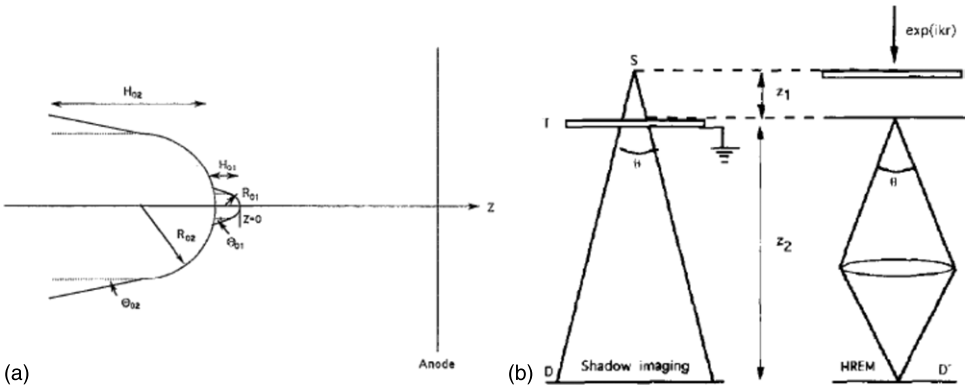

Figure 9. (*a*) Nanotip model used for ray-tracing calculations: $R_{01,02}$ radii of curvature, $H_{01,02}$ height of nano-protrusion and tip, $\theta_{01,02}$ shank angles. (*b*) The schematic set-up of a point projection microscope is given. It consists of the field emission tip S and the specimen on earth potential which simultaneously acts as an anode of the system. The shadow image formed at D is out of focus by z_1. (Reproduced from [324], copyright 1993, with permission from the American Institute of Physics, and from [337], copyright 1993, with permission from Elsevier.)

only which is comparable with the corresponding shot noise, both measured at a bandwidth of 5 Hz. The goal of this work is to determine the FE current fluctuations caused by inherent properties of ultra sharp atomic size field emitters—e.g. caused by ballistic or resonant tunneling, tip geometry or correlations due to the Pauli exclusion principle and Coulomb interaction [274]—without disturbances by other noise sources.

Martinez and Polatdemir [256] propose *an experiment to measure the tunneling time of particles (electrons)* by using an electron biprism interferometer. One of the coherent beams tunnels through a symmetric barrier. The barrier height is chosen such that its transparency is 50%. Under the assumption that the tunneling time leads to a phase difference for the transmitted electron beam, its value could be calculated from the corresponding fringe shift. According to the proposal, the experimental parameters for this experiment are extremely demanding: e.g. the accelerating voltage of the electrons must be on the order of 15 meV, their energy width lower than 1 meV, not to speak about the extreme sensitivity of such a low voltage interferometer (which has not yet been developed) to magnetic ac stray fields and the corresponding Aharonov–Bohm (A–B) phase shifts. The low brightness at these voltages and flicker noise of the field emitter will be other obstacles. The latter could possibly be overcome by using an XHV-FEM gun as described in the last paragraph [272] and the extremely small energy width of the beam could be realized by using the monochromatic electron emission from the macroscopic quantum state of a superconducting field emitter [259].

2.3. Electron optical properties of nanometer-sized field emission electron sources and lensless low-voltage point projection electron imaging (in-line holography)

By using a nanotip as a field electron source in a point projection microscope Fink *et al* [320] were the first to achieve atomic resolution in micrographs of gold crystals in this type of microscope. Additionally, the theoretical study of Garcia and Rohrer [325] and the experiments of Fink [282] and of the JCH Spence group [322–324] proved another extraordinary feature of nanotip sources: they found that a nanotip illuminates an area some centimeters in diameter on a viewing screen about 15 cm from the tip coherently. Certainly, these properties of nanotip sources are quite different from those of conventional field emission sources: the virtual source size of a conventional comparatively 'blunt' annealed field emitter tip with a radius of about 60 nm is about 3.5 nm. It emits at an extraction voltage of 1 kV a current of 100 nA which corresponds to an average brightness of 4.6×10^5 A cm^{-2} sr^{-1}. Nanotips are morphologically more complicated. They consist of a conventional, 'blunt' field emission tip with a nanometer-sized protrusion on top of it ending in a single or a few atoms with a diameter on the order of 1 nm and a height of 3 nm (figure 9(*a*)). The average brightness of a single-atom terminated nanotip was found to be 3.3×10^8 A cm^{-2} at 470 V extraction voltage and 2.15 μA of emission current, an improvement of two orders of magnitude over existing cold field emission electron sources. The corresponding effective source size is 0.6 nm. At a lower extraction voltage of 150 V when the single atom exclusively participates in the field emission process the effective source size reduces to about 0.3 nm. These experimental results were published by Spence *et al* in 1993 [322, 324]. Atomic resolution obtained in point projection Fourier images [320, 321] and field ion images prove that the virtual source size of the nanotips is on the order of 0.3–0.6 nm, i.e. more than an order of magnitude smaller than of conventional field electron emitters. These very promising new features of the sources and their morphologically complex structure motivated the Spence group to calculate the size and aberrations of the virtual source (first-order electron optical properties) and the transverse beam coherence for nanotip structures and compare them with the data for planar emitters and conventional field emission tips [324, 322]. By tracing the electron trajectories emitted from different positions on the tip with different take-off angles and starting energies they analyzed statistically the electron optical properties of nanotip sources. Their nanotip model is given in figure 9(*a*) and consists of a nanometer-sized protrusion with a height of 3 nm and a radius of 1 nm on top of a base tip with an end radius of 100 nm. The shank angles of the nano-protrusion and the base tip are 30° and 10°, respectively. In order to calculate the brightness of electron sources and the resolution

available in point projection transmission microscopy, in-line holography and Fourier imaging the following parameters were assumed (see figure 9(*b*)). A very short tip-to-specimen/anode distance of 300 nm—which is a typical distance in projection microscopy, in order to reach magnifications sufficient for atomic spatial resolution—was chosen for the calculations, which gave field strengths on the order of 5 V nm^{-1} at the tip apex, sufficient for field emission from tungsten, at a potential difference between tip and anode of 100 V only. The region between anode and viewing screen is field free. The initial energy of the emitted electrons was assumed to be between 0.15 and 0.25 eV, characteristic values for field electron emission from tungsten at room temperature. The emission probabilities were calculated from the Fowler–Nordheim theory with the explicit numerical evaluation of the electric field strength along the tip surface and assuming a work function of tungsten of 4.5 eV. The calculations take into account only classical interactions with the potential field. Quantum- and space-charge effects are neglected, yet the electron optical properties of nanometer-sized cathode structures are accurately predicted.

The Gaussian image plane is defined by the intersection of paraxial back-propagated rays with the optical axis z. Spherical- and chromatic-aberration coefficients are obtained by back-propagating non-paraxial rays and analyzing the angular- respectively energy-deviation dependence of the radial displacement r_i of that ray in the Gaussian image plane. This plane is behind the tip, the extension of the current density distribution within r_i is virtual. The spherical aberration coefficients of 3rd and 5th order C_{s3} and C_{s5} referred to the object space are determined by a least squares fit of the experimentally obtained r_{is} to

$$r_{is} = M(C_{s3} \sin \alpha_0^3 + C_{s5} \sin \alpha_0^5), \tag{2.1}$$

where M is the linear magnification which was found to be $M = 0.531$. The values obtained for C_{s3} and C_{s5} are 0.177 nm and 0.094 nm, respectively.

By the same procedure the chromatic-aberration coefficient C_c was found by tracing back electrons emitted at small take-off angles α_0 with various initial energy deviations δE_0 from the nominal energy E_0 and fitting them to the experimental values of r_{ic} to

$$r_{ic} = M C_c (\delta E_0 / E_0) \sin \alpha_0. \tag{2.2}$$

Here, once again M is the linear magnification. The chromatic-aberration coefficient C_c for this nanotip was found to be 0.142 nm.

These aberration constants which refer to the final beam energy calculated from the electric field distributions in front of conventional field emission tips and nanotips seem uncommonly small compared with the aberrations of the best electron lenses used in electron microscopes. The well-known fact in electron optics that the aberrations scale down with the dimensions of the lenses is the reason for the tiny aberration coefficients of nanotips: in front of a field emission tip/nanotip 99% of the field strength is concentrated within an extension of a few nanometers around the tip apex and effectively forms a micro-lens with nanometer dimensions. The lateral coherence width of such a tip in the specimen plane of a point projection microscope is larger than the width of the intensity distribution even under the assumption that the emission process is completely incoherent. For the same reason for low voltage electron interferometry a diode system as an electron source is the best choice since it guarantees the smallest effective (virtual) source size and in turn the best lateral coherence [67].

It is well beyond the scope of the present discussion to give all details of the full length paper on 'the aberrations of emission cathodes...' by Scheinfein *et al* [323] here and the reader is referred to the original literature.

Another fundamental feature intimately connected with beam brightness and coherence is the concept of degeneracy [326]. The beam degeneracy δ is given by the ratio of the actual brightness of a source to the theoretical maximum brightness B_{max} (maximum occupation number per cell in phase space). By Pauli's exclusion principle the maximum occupation number per cell is two for fermions of opposite spins [328, 329]. Unlike photon sources for which the degeneracy can be as large as about 10^4 for a 1 mW He–Ne laser and on the order of 10^{40} for 50 Hz ac current from a power plant [326], the maximum fermion degeneracy is unity, i.e. every cell in phase space is occupied only by one electron of a certain spin direction. This is liable for the fact that for fermions an upper limit of maximum brightness B_{max} exists. In an experimental study of the Fresnel edge fringes in a point projection microscope Spence *et al* show that not only the electron optical parameters of their field emission source can be extracted but also the degeneracy can be measured from a quantitative observation of Fresnel fringes [330]. Compared with conventional field emitters the few- and single-atom field emission sources are large step forward in electron and ion interferometry, Fourier imaging and lensless electron holography. Hopefully, they find their way into commercial electron microscopy and holography instruments in the near future [327].

2.3.1. Lensless low energy in-line electron holography and transmission projection microscopy. They are—besides applications in scanning tunneling microcopy—the first applications of Fink's nanotips [282, 319, 320]. The specimen and its vicinity is illuminated by an ultrasharp field electron emitter. Owing to the sub-micrometer distance between emitter tip and the specimen, firstly, extraction voltages and in turn electron energies as low as 2–80 eV can be achieved and secondly, the magnification given by the macroscopic distance D divided by the sub-micrometers tip–sample distance is sufficiently high for resolving atoms. Indeed, transmission point projection images of a thin gold film show at electron energies between 150 and 300 eV the gold lattice atomically resolved. A remarkable consequence of the nearly complete coherence and absence of aberrations of these electron sources is that the point projection images formed downstream are practically unaberrated with a focus defect of z_1 (figure 9(*b*)) (its value and the magnification can be easily determined by taking two images at different magnifications [336]). For an opaque sample (e.g. a holey carbon foil at 300 eV [336]) in the plane of observation of a projection microscope (figure 9(*b*))

the transmitted (reference) beam and the electron waves scattered by the edges of the specimen superimpose and form a Fraunhofer far-field in-line hologram. The opaque edges of the specimen are surrounded by Fresnel edge fringes. Eventually, if the specimen contains, e.g. two adjacent pin holes, the electron waves emerging from them may superimpose in the observation plane and form equidistant parallel Young's fringes [332, 336].

The great advantage of this form of holography and transmission point projection microscopy is that no electron lenses with their aberrations are needed which would blur the holograms. In turn, there is no need to correct the holograms, numerical reconstruction is straightforward. From point projection in-line holograms the outer shape of the opaque object structures can easily be retrieved [338], e.g. by light optical holographic reconstruction methods or digital reconstruction algorithms. Thanks to the low energy of the electrons, in the holograms high phase contrast is achieved even for light atoms (e.g. carbon) and radiation damage seems to be a minor problem [334] at least for a restricted class of organic compounds [337].

The imaging of biomolecules at very low energies of the electrons in the range of 2 eV to about 50 eV is a very special and promising application of lensless shadow imaging. The range of electrons in solids reaches its minimum at about 50 V, i.e. specimens of a few nanometers in thickness are practically opaque. Below 50 eV their range increases sharply, the bimolecular specimens become transparent again, and a significant fraction of the elastically scattered electrons traverse the sample and convey useful information about the sample structure to the channel plate detector. Inelastic scattering events result in radiation damage. Below 50 eV fewer excited states of the molecules are available and below 10 eV neither plasmons nor inner shell ionization are possible avoiding a large amount of radiation damage. For partially transparent thin samples when multiple scattering becomes significant the interpretation becomes difficult and—in order to retrieve internal atomic structures—in addition to holographic reconstruction, multiple scattering band structure and LEED-type calculations are indispensable. Spence [335] summarizes the problematics of application of this type of holography with the following words: 'We emphasize that electron holography cannot allow one to 'see inside' a crystal. All reconstruction methods deal with free-space propagation, whereas the propagation of electrons in crystals or molecules is governed by the Schrödinger equation, which includes dynamical dispersion effects due to variation of potential within the sample. Nevertheless, holograms recorded at low voltage are sensitive to the coordinates of the atoms along the beam path, so that trial and error reconstruction methods might be used to obtain three-dimensional optical potential from the holograms'. A profound analysis of this complicated situation is given in the papers of Spence and co-workers [333, 337].

2.4. A lensless electron interferometer with carbon nanotube biprism filaments

MWCNTs were discovered in 1991 by Sumio Iijima in the NEC Fundamental Research Laboratory in Tsukuba when he studied the soot created in an electrical discharge between two carbon electrodes. Due to their outstanding mechanical (e.g. extremely high elastic Young's modulus) and electronic properties nanotubes are an exciting area of condensed-matter physics with many applications in future (MWCNTs appear to be ballistic conductors having nearly the same conductance of $G_0 = 2e^2/h$, i.e. they are predicted to have a minimum resistance of about 6500 Ω, independent of their length).

Electron biprism interferometry has already benefited from the availability of carbon nanotubes: the conventional electron optical biprism with a quartz filament of a diameter on the order of 500 nm is substituted by micro-biprism consisting of a MWCNT with a diameter of a few nanometers fixed on a sub-micrometer scale hole [264–266]. In order to see fringes, in an electron biprism interferometer both edges of the biprism filament must be illuminated coherently, i.e. the lateral coherence condition must be fulfilled. By using a field emitter with only a few atoms at its apex, the virtual source illuminating the nanobiprism is sub-nanometer in size and illuminates a nanobiprism at an extremely short distance of a few hundred nanometers coherently. By adding to this source–biprism arrangement a fluorescent screen at a distance of about 15 cm we get an electron biprism interferometer without the need of any electron lenses for magnification of the biprism fringes. The contrast of the fringes is not degraded by lens aberrations but exclusively defined by the lateral coherence which is given by the size of the illuminating source. By choosing a sufficiently high energy of the electrons, the requirement of longitudinal coherence is readily fulfilled. Such an interferometer has been constructed and successfully put into operation by Cho *et al* in 2004 [263] and is presented in figure 10.

With this interferometer they measured an unexpected increase in spatial coherence of an electron beam for decreasing temperature of the field emitter (see figures 10(*b*) and (*c*)). Details and the results of their investigation were discussed already in section 2.2.2 on spatial coherence.

2.5. Manipulation of the paths of charged particles by multi-biprism and biprism–lens combinations in such electron interferometers

The very first experiment after the invention of the biprism was the beautiful experimental proof of the Aharonov–Bohm effect (A–B effect) by Möllenstedt and Bayh [44, 78]. In this experiment a confined magnetic flux generated by a micro-coil of about 14 μm in diameter penetrates an enclosed area between the coherent beams behind the biprism without touching the beams. In an electron biprism interferometer with a single biprism filament the distance between the two coherent beams is on the order of the diameter of the biprism filament, i.e. about 1 μm. In order to realize the large distance on the order of 60 μm needed for the coil between the beams Möllenstedt and Bayh used a triple biprism arrangement (figure 11(*a*)): the first, negatively charged biprism filament bends the beams apart from each other, the second, positively charged one bends them toward each other again and the third one reduces the angle of superposition of the two beams in

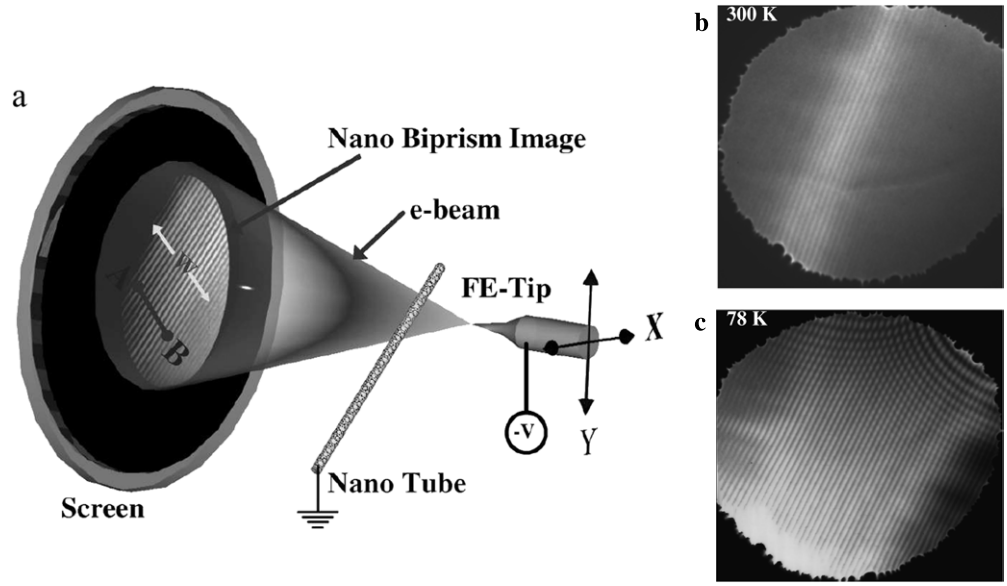

Figure 10. (*a*) Nanotube-biprism interferometer. The field emitter is aligned by a piezo tube to the MWCNT biprism. Because the emitter–MWCNT distance is much smaller (on the order of 50 nm) than the MWCNT–screen distance (16.5 cm) no lens for magnification of the interference fringes is necessary. The width W of the fringe field directly gives the coherently illuminated width (perpendicular to the fringes) in the plane of the fluorescent screen. The wavelength of the electrons is on the order of 1 Å and the spacing of the fringes on the screen about 0.4 mm. (*b*) On the rhs interference fringes taken at room temperature and 78 K are presented. (*c*) The larger number of fringes visible at 78 K and their higher contrast is due to an increased spatial coherence at low temperature. (Reproduced from [263], copyright 2004, with permission from the American Physical Society.)

order to achieve larger distances of the interference fringes. More advanced with respect to the possible distance between the beams are the optical set-ups with a combination of biprisms and lenses. With the set-up given in figure 11(*b*) 50 μm and with that in figure 11(*c*) up to 300 μm have been realized [79, 80]. Another great advantage of the beam path given in figure 11(*c*) is that the distance of the interference fringes can be chosen by a suitable voltage at the second biprism independently of the separation of the coherent beams. A deficiency of the beam paths described up to now is that the amplitudes of the two plane waves leaving the biprism are not constant but modulated caused by the interference with the diffracted waves emerging from the two edges of the biprism filament. The way to avoid this is given in the next paragraph.

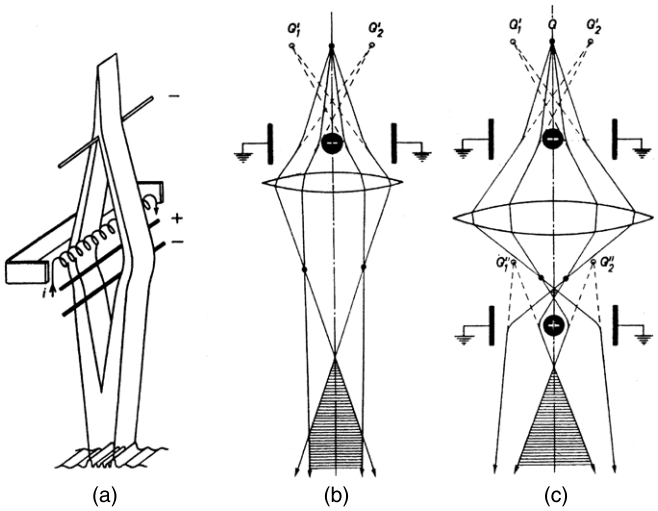

Figure 11. Wide separation of the coherent beams: (*a*) Möllenstedt and Bayh achieved 60 μm of separation of the coherent beams by using the triple biprism arrangement [44, 78] given in (*a*). Near the second biprism they inserted a magnetic flux generating micro-coil 14 μm in diameter and observed the A–B effect. (*b*) By using biprism-lens combinations: a negatively charged biprism bends the beams apart from each other. Superposition of the beams is achieved by the focusing action of an electron lens. (*c*) Now the overlap of the beams is achieved by an additional, positively charged biprism filament. The advantage of this beam path is that the distance of the fringes can be chosen independently of the separation of the beams.

2.6. Suppression of the unwanted intensity modulation of the biprism fringes caused by diffracted waves emitted at both edges of the biprism filament

The biprism filament splits the wave front which emerges, e.g. from an electron field emitter into two parts, one the right and one the lhs. From the edges of the biprism filament additionally, diffracted waves emerge into a small angle in the forward direction and interfere with the not diffracted plane wave front. In turn, they modify the amplitude of these wave fronts slightly (see the three micrographs on top of figure 12). This modulation leads to the characteristic intensity modulation of the fringe field which is observed in every electron interferometer working with a single biprism (figure 12, micrographs on the bottom) mainly near both borders of the biprism fringes. This modulation caused by Fresnel diffraction at the edges of the biprism complicates the quantitative evaluation of electron interferometric or electron holographic experiments (see, e.g. [81]). Only recently have methods been developed in the context of electron holography to record holograms and interferograms 'without' Fresnel

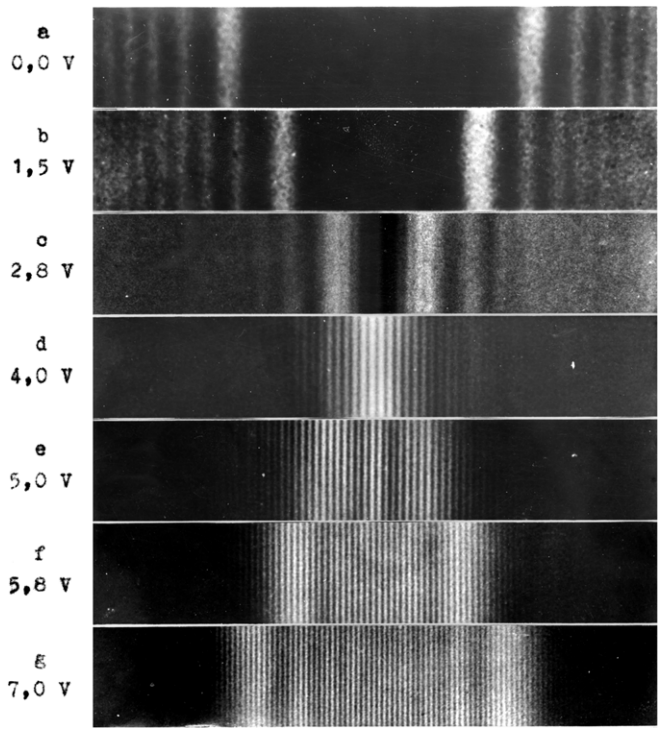

Figure 12. The first electron biprism interference fringes (reproduced from Heiner Dükers PhD thesis of 1955, energy of the electrons 20 keV, the biprism voltage is given on the lhs). In the three pictures at the top, the shadow of the biprism filament is seen in the middle and on the lhs and rhs the two wave fronts are seen. Their intensity is clearly modulated by the diffracted waves at both edges of the biprism filaments. This leads to the characteristic intensity modulation of the biprism fringes which are generated when the biprism voltage is increased and the intensity modulated wavefronts overlap (the four pictures at the bottom).

fringes [82–88, 90]. Thus holograms can be reconstructed and interferograms evaluated using these new optical systems without the artifacts and additional difficulties caused by Fresnel fringes (see, e.g. [81]). These new optical systems (see, e.g. [87]) additionally allow one to control independently all interference parameters, e.g. the fringe spacing s_{obj} is adjusted by varying the potential of the first biprism filament and the width of the interference region W_{obj} by the potential on the second biprism. The optical set-up of the new biprism–lens–biprism system is given in figure 13(*A*).

The salient point which is liable for the suppression of the intensity modulation of the interference fringe system is the fact that the plane *where the first biprism is located and the waves diffracted by both edges of this biprism filament are generated, are exactly focused onto the second image plane* (figure 13(*A*)) eliminating Fresnel fringes in principle (to electron microscopists it is well known that an electron micrograph is focused exactly by adjusting the excitation of the objective lens so that diffraction fringes just vanish). Additionally, since the second biprism filament is located inside the shadow of the first one, no diffraction at the edges of this biprism filament takes place: Fresnel fringes are not generated at all (see figure 13(*A*)). The fringe spacing s_{obj} and the width of the interference region W_{obj} projected on the specimen plane are given by [86, 87]

$$s_{\mathrm{obj}} = \frac{1}{M_{\mathrm{l}} \cdot M_{\mathrm{u}}} \frac{a_2 D_{\mathrm{l}} \lambda}{2[\alpha_{\mathrm{l}}\alpha_2(D_{\mathrm{l}} - L_{\mathrm{l}}) + \alpha_{\mathrm{u}} b_2 D_{\mathrm{u}}]}, \tag{2.3}$$

$$W_{\mathrm{obj}} = \frac{1}{M_{\mathrm{l}} \cdot M_{\mathrm{u}}} 2\alpha_{\mathrm{l}} L_{\mathrm{l}} - \frac{1}{M_{\mathrm{u}}} d_{\mathrm{u}}. \tag{2.4}$$

As W_{obj} is independent of the upper deflection angle α_{u}, s_{obj} and W_{obj} can be controlled independently. When the lower biprism filament is located in the crossover point of the magnifying lens ($D_{\mathrm{l}} = L_{\mathrm{l}}$), s_{obj} also becomes independent of the lower deflection angle α_{l} (equation (2.3)).

This avoids artifacts in the reconstruction of holograms and will simplify the evaluation of Fourier spectroscopic measurements of electron spectra in future (see section 3.5.2). As an application of such an 'intensity modulation free' interference field Harada *et al* [87] measured the spatial coherence at the specimen position (figure 13(*B*)) according to Speidel and Kurz [89] and the modulation transfer function (MTF) of a CCD camera system by recording the contrast of the fringes versus their spatial frequency (figure 13(*C*)).

The possibility of realizing a *large enclosed area between the coherent beams* with the new 'Fresnel diffraction free' optical systems by charging the first of the two biprisms of the system not positively, but *negatively* has already been investigated experimentally with respect to applications in electron holography (see, e.g. figure 2(*d*) in [86]). A study with the goal to realize an enclosed area as large as possible is highly desirable. A large enclosed area is crucial for high sensitivity rotational and accelerational sensing with matter waves (electron, ion and atomic interferometers). These will outperform the sensitivity of conventional mechanical and multiple circuit optical Sagnac interferometers by many orders of ten (see section 3.2).

An even more flexible system using three biprisms has been tested recently. Details are not presented here but may be found in the the original papers [90, 91].

3. Experiments on the influence of electromagnetic and gravito-inertial potentials and fields on the quantum mechanical phase of matter waves

According to *classical* electrodynamics of Faraday and Maxwell, electromagnetic effects are fully described by the field strengths. Potentials were merely considered as convenient mathematical tools for solving electromagnetic problems. It was realized already in 1949 by Ehrenberg and Siday [40] and ten years later by Aharonov and Bohm [41] that in quantum mechanics the electromagnetic fields do not completely describe all electromagnetic effects on charged particles. According to these authors in a doubly connected region where the electromagnetic fields locally vanish but not the potentials, coherent electron waves traveling from a source to a fixed final point acquire a phase difference which is constant on all different possible paths irrespective of the spatial distribution of the potentials (potential field distribution) in the field-free space. This fact can be interpreted on the one hand as a force-free interaction with local scalar- or

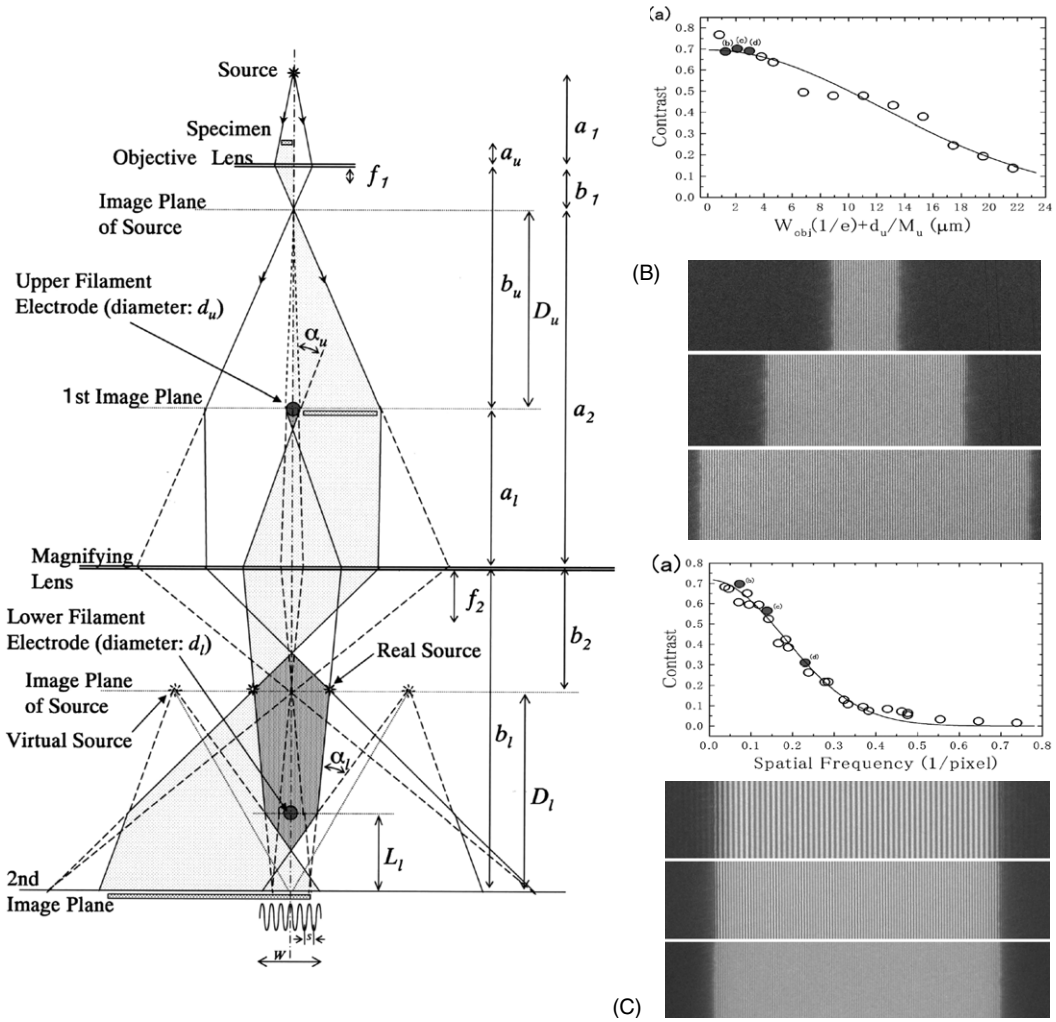

Figure 13. (*A*) The magnifying lens is imaging the plane where the upper biprism and a focused image of the specimen are located in the second image plane. This makes the system very flexible. To achieve complete and independent control of both parameters the fringe spacing s_{obj} and the width of the interference region W_{obj} the lower filament electrode is positioned at the crossover point of the magnifying lens, i.e. $D_l = L_l$ (see also, e.g. figure 2 (*b*) in the paper of Harada *et al* [86]). In order to avoid generation of diffracted waves at the edges of the second biprism it is located in the shadow area of the first one. (*B*) As an application, the coherence function of the 1 MV field emission electron microscope at the specimen position was measured with the new system. Spatial coherence was evaluated by changing the interference distance with fixed fringe spacings. All interference fringes were set at 10 pixels/fringe and recorded by a CCD camera. The solid Gaussian curve in (*B*) (*a*), reveals excellent spatial coherence up to about 5 μm (micrographs (*b*), (*c*), (*d*) correspond to the solid circles in (*a*)). The fringe contrast of 20% even at a distance of about 20 μm is remarkable. (*C*) Fringe contrast versus spatial frequency of interference fringes as an example of a measurement of a modulation transfer function. Open circles are experimental results and the solid line is the Gaussian fit. Three solid circles highlighted by letters (*b*), (*c*) and (*d*) correspond to the micrographs at the bottom of (*C*). (Reproduced from [87], copyright 1994, with permission from the American Institute of Physics.)

vector-potential fields or, on the other hand, as a non-local interaction with an enclosed magnetic flux. The classical electric and magnetic fields do not contain nor act on the quantum mechanical parameter 'phase' and consequently are, according to Wu and Yang [76], not a complete description of electromagnetism. It is shown in their paper, that not the phase—which is not an observable as already proved in the early publications by Rang in 1964 [96, 97]—but the phase factor (phase difference) leads to physical effects even if the charged particles moved only in field free regions. Not the phase but the phase factor is the only physically measurable and in turn meaningful parameter. The A–B effect demonstrates that the potentials have an efficacy in quantum mechanics which is definitely not a property of electric fields. The central point of this section will be to clarify by means of some experiments the quantum mechanical and classical contributions of electromagnetic *and* gravito-inertial potentials and fields to phase differences which are observed in matter wave interferometers. While Aharonov and Bohm [41] triggered with their perplexing non-local influence of enclosed electromagnetic fluxes an extensive literature on the action of electromagnetic potentials and fields in quantum mechanics (see, e.g. [43, 44, 93, 94, 117–123] and citations there-in), a comparatively small number of theoretical and experimental studies on the influence of gravito-inertial fields and potentials on the quantum mechanical phase factor exists. In this review we will concentrate in the next section on these experiments and papers.

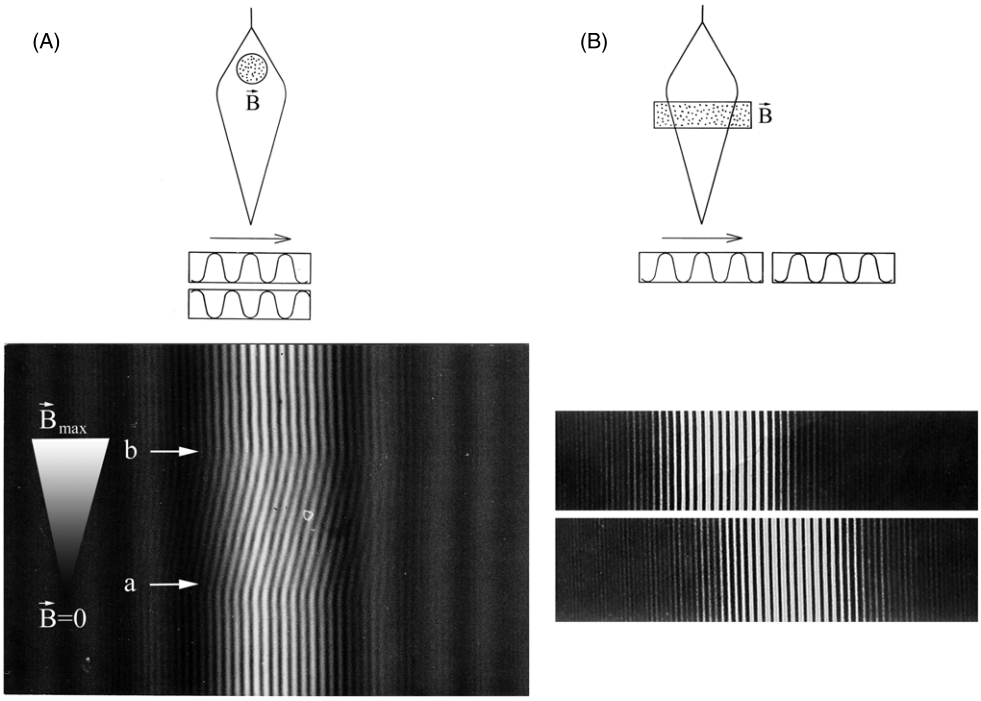

Figure 14. The A–B effect. (*A*) The magnetic flux $\vec{B}$ is concentrated in between the coherent beams without touching them. When the magnetic flux increases continuously (figure (*A*), bottom) from value *a* to *b*, the envelope of A–B interference field remains stationary. Only the interference fringes inside the stationary interference field travel as a consequence of the A–B phase shift continuously from the left to the right for increasing enclosed flux. The traveling of the fringes can therefore be observed only live on the fluorescent screen but not on a photographic plate. (A phase shift of even multiples π does not change the appearance of interference field at all which is important for the observation of flux quantization in superconductors.) (figure (*A*), bottom) was taken by moving a narrow slit—which is oriented perpendicular to the fringes—in fringe direction across the photographic plate while the flux was increased continuously from *a* to *b*. (figure (*B*), bottom) The influence of magnetic fields on biprism interferences. A small homogeneous magnetic field below the biprism in the direction of the biprism wire overlaps also the beam paths and deflects ($\Longrightarrow$) the whole fringe field to the right. The fringe field does not change its appearance (figure (*B*), bottom), due to the fact that the A–B phase shift caused by the enclosed magnetic flux compensates—exactly in pace—the path length differences occurring due to the deflection.

3.1. The electromagnetic and inertial A–B effect

Due to the formal identity between the forces in electromagnetic fields $\vec{F}_{\rm em}$ (3.1) on the one hand and the forces in gravito-inertial fields $\vec{F}_{\rm gi}$ (3.2) on the other, the situation in gravito-inertial fields is completely isomorphic to an electromagnetic field and immediately leads to corresponding phase shifts in the gravito-inertial case.

$$\vec{F}_{\rm em} = q\vec{E} + q(\vec{v} \times \vec{B}) \quad \text{(electromagnetic)}, \tag{3.1}$$

$$\vec{F}_{\rm gi} = m\vec{g} - m(\vec{\omega} \times (\vec{\omega} \times r)) + 2m(\vec{v} \times \vec{\omega}) \quad \text{(gravito-inertial)}, \tag{3.2}$$

where q is the charge, $\vec{E}$ the electric and $\vec{B}$ magnetic field and $\vec{v}$ the velocity. $m\vec{g}$ in equation (3.2) means the gravitational force, the second term the centrifugal force and the third one the Coriolis force.

A characteristic feature of phase shifts which are *exclusively caused by potentials* is that there is no force on the particles and consequently, when we, e.g. observe a fringe system in a biprism interferometer, no lateral deflection of the envelope and the entire pattern of interference fringes takes place. Only the fringe pattern inside the envelope changes continuously with changing enclosed magnetic flux. This is vividly demonstrated in the beautiful experiment on the A–B effect of Möllenstedt and Bayh (figure 14(*A*)) [78, 44]. In their set-up by varying the current through a coil the enclosed magnetic flux and in turn the vector potential $\vec{A}$ were varied continuously provoking a continuous phase shift of the interference fringes within the envelope of the fringe pattern.

When the electromagnetic (gravito-inertial) fields do *not* vanish on the doubly connected paths of charged (non-charged) particle waves (figure 14(*B*)), e.g. in a biprism interferometer, forces are exerted, their trajectories and in turn the system of interference fringes are deflected laterally. It is remarkable that one always observes the same interference field irrespective of the deflection angle: that is, the fringes remain at constant positions within the interference field. This happens even though a path length difference between the separated wave packets is introduced by the deflection, which should give rise to a corresponding phase shift. The fact that this is not the case means that the phase shift caused by the change of the path length is exactly compensated by some counteracting effect. This compensating effect is the A–B phase shift [93, 43]. For an electric deflection field, it is the scalar A–B phase shift; for a magnetic field, it is the 'conventional' A–B phase shift induced by the vector potential $\vec{A}$ (see figure 14). Ehrenberg and Siday [40] realized already in 1949 that these phase shifts exist and that they are, in fact, absolutely essential for the fact that electron optics works: i.e. that electron optical components

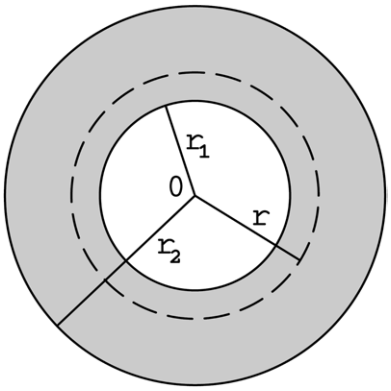

Figure 15. The Aharonov–Carmi 'Gedankenexperiment'. A 'rotonaut' fixed in his ring shaped laboratory between r_1 and r_2 rotating with angular velocity $\dot{\theta}_0$ is releasing particles relative to his lab with initial $r \geqslant r_1 \leqslant r_2$ with velocity v_0.

can be used for image formation in electron microscopy, lithography, etc.

As already mentioned, considering equations (3.1) and (3.2) we expect a full analogy of the phase shifts originating in path length differences caused by deflections and phase shifts by potentials for electromagnetic and gravito-inertial potentials and fields [124–126] even for relativistic matter beams [127]. The last terms of the equations mentioned above, immediately show that the Lorentz force on a charged particle corresponds in the mechanical case to the 'fictious' velocity dependent Coriolis force exerted on a particle with mass m in a rotating frame [128]. This fact lets us presume that a 'force-free' vector potential field caused by a rotation leads to an inertial phase shift (a 'rotational phase shift' in its purest form) given by

$$\Delta\Phi_{\text{inertial}} = (2m/\hbar)\int \vec{\omega}\cdot \mathrm{d}\vec{\sigma} \Longleftrightarrow \Delta\Phi_{\text{A–B}} = (e/\hbar c)\int \vec{B}\,\mathrm{d}\vec{\sigma}, \tag{3.3}$$

where the surface integral is over the oriented area enclosing the rotational flux. It corresponds exactly to the A–B phase shift $\Delta\Phi_{\text{A–B}}$ caused by an enclosed magnetic flux given on the rhs of (3.3) when $2m\vec{\omega}$ is substituted by $(e/c)\vec{B}$.

Aharonov and Carmi proposed to realize the gravito-inertial analog of the A–B phase shift in a Gedankenexperiment described in their paper on 'Quantum aspects of the equivalence principle' [124]: they consider a 'laboratory' confined to an arbitrarily narrow ring of radii r_1 and r_2 centered at O in figure 15. If the laboratory is rotated with angular velocity $\dot{\theta}_0$ around O, and the physicist fixed in that lab observes the motion of particles which he releases (with initial r_0 and v_0 relative to his lab), he will conclude that there are two types of non-zero forces acting in his lab (explained as 'centrifugal' and 'Coriolis' by the stationary observer). The centrifugal force is describable through the gradient of a scalar potential, and the velocity dependent Coriolis force via the curl of a vector potential. In principle these forces could be compensated just inside the ring by introducing appropriate gravitational fields $g_{\mu\nu}$. Another, and as we will see, very convenient choice to render the test particles inside the ring force free is to compensate the inertial forces by suitable electrical ones. As we will see, the above inertial forces can be canceled if charged particles with the same ratio e/m are used in the experiment. Radial electric fields cancel the centrifugal and uniform magnetic fields perpendicular to the plane cancel the Coriolis force. The physicist on the ring would then tend to conclude that he is in an inertial system. Since we assume that the $\vec{B}$ fields are confined to the ring only, the inertial fields in the interior of the ring r_1 remain uncompensated and provide a rotational flux which produces (forceless, in the ring) potentials A_μ outside the circle r_1. The physicist on the ring would observe that $\oint \vec{A}\cdot \mathrm{d}\vec{l}$ is non-zero and would detect this shift in the interference pattern as predicted by Aharonov and Bohm [41]. This could be done by the physicist, to double check whether his lab is indeed inertial (and he would find that it is not).

Unknowingly, exactly this experimental proof of the inertial A–B effect has been performed by Zimmermann and Mercereau with Cooper pairs [130] already 8 years before the paper of Aharonov and Carmi appeared. Zimmermann and Mercereau set into rotation a superconducting quantum interferometer (SQUID) and published their result under the title 'Compton wavelength of superconducting electrons'. They measured a phase shift which is numerically exactly identical to the Sagnac phase shift for Cooper pairs—which is not surprising when one knows, e.g. the paper of Werner and Brill [93]—and remarked 'this type of experiment is somewhat similar to the Michelson Sagnac experiments with light. The physical source of the phase shift differs, but the formal expressions are identical'. In hindsight it proved to be unfortunate to include into the title only the term 'Compton wavelength' and not also 'Sagnac phase shift' which was the reason that their result remained largely unknown and is not even mentioned in the 'classical' review paper of Post [129] and further reviews on the Sagnac effect which were published before 1993 when the paper on the Sagnac effect of electrons appeared [75] with a hint at the Mercereau–Zimmermann experiment.

A re-analysis by Semon [149] of the experiment of Zimmermann and Mercereau in the light of the Aharonov–Carmi paper [124] made evident that in a rotating superconducting quantum interference device the rotation induces electric and magnetic fields that exactly compensate the centrifugal and Coriolis forces on the Cooper pairs [131–135] while the enclosed rotational flux in the non-conducting enclosed area remains un-compensated, i.e. Mercereau and Zimmermann observed in their superconducting rotating quantum interferometer (SQUID) for the first time the *inertial A–B phase shift* induced by the enclosed rotational flux which is numerically identical with 'Sagnac' phase shift.

In all the Sagnac experiments with matter waves, which will be presented in the next section, the fields extend over the region of the trajectories of the particles. Then, in addition to the rotational fringe shift within the stationary envelope of the pattern due to the enclosed flux, there will be a deflection of the whole interference field including its envelope by an amount a classical electron would be shifted due to the curvature of the electron trajectories by the Lorentz force. As already explained in figure 14(B) on the A–B effect such a field produces a displacement of the fringes which

exactly keeps pace with the phase shift of the beams by the enclosed rotational flux, so that the deflected fringe system appears to remain not displaced relative to the envelope of the pattern (see also [140]). As a consequence, rotation can be measured quantitatively either by recording the phase shift in a A–B like experiment, where the fields are compensated, or by measuring the lateral shift of the system of interference fringes when the fields are not compensated (Sagnac-type experiment).

3.2. Sagnac experiments

3.2.1. Sagnac effect. In the parlance of theory of relativity, the effect of rotation on space–time, as can be measured in two beam interferometers in which the beams enclose a finite area, is called the Sagnac effect. Due to the fact that for matter waves, their wave nature is essential for the understanding of the Sagnac effect, quantum theory is another indispensable ingredient for the understanding of this effect. Nevertheless, the effect for light was proposed and an expression for the phase shift derived on the basis of the ether theory by Sir Oliver Lodge in 1893 [164, 165] and measured in 1913 by Georges Sagnac—an ardent advocate of ether theory—in the context of classical physics. In 1961 Heer [137] was the first to propose that also for matter waves the rotational phase shift is proportional to $\vec{A} \cdot \vec{\Omega}$ in an interferometer of projected area $\vec{A}$ rotating with an angular velocity $\vec{\Omega}$. These facts were the origin of controversial discussions and attempts to elucidate the physical origin of the rotational phase shift from the first experiments [164–174] until today. A condensed version of the history of this discussion is given in Stedman's review article [181], Malykin's paper [175] and his methodological note entitled [176] 'The Sagnac effect: correct and incorrect explanations'. In short for correct explanations at high rotation rates and when gravitational field effects are to be taken into account general theory of relativity is indispensable. Special theory of relativity is sufficient in the absence of gravitational fields, where there is no space curvature since non-inertial frames of reference can be described in terms of special theory of relativity in the most general way, for arbitrary accelerations and not only for kinematic events [187]. As already mentioned, quantum mechanics is an indispensable ingredient to understand the Sagnac effect. It is remarkable that non-relativistic quantum mechanics is sufficient to get the correct results due to a peculiarity in the behavior of non-relativistic quantum mechanics under Galilean transformations which distinguishes it from Galilean invariant classical theories: in non-relativistic quantum mechanics the phase of the wave function is not invariant under Galilean transformations [213, 214].

Until today, the most fascinating property of the Sagnac effect is the fact that it gives us the possiblity to measure an absolute rotation by an experiment which is conducted entirely within the rotating frame of reference.

Milestones in the development of Sagnac interferometry were the first proposal of an interferometrical detection of a rotation by Sir Oliver Lodge in 1893 [164, 165], the famous experiments of Franz Harress [167], Georges Sagnac [168–170] and the phase shift caused by the Earth's rotation in a very large light optical interferometer by Michelson and Gale in 1925 [136, 166, 171]. After the invention of the laser Sagnac interferometry experienced a dramatic increase in precision as well as in width of application [183]. Today, the rotation rate of the Earth Ω_E can be measured with an accuracy of $\sim 10^{-8}$ by Sagnac interferometry which is only one order below the fluctuations of the Earth rotation rate. At the moment, the most precise time consuming and complex method to measure these fluctuations is by very long baseline interferometry (VLBI) [184]. Hopefully, this accuracy will be accessible in the very near future with compact, Sagnac type instruments: ring lasers [160, 181], atom interferometers [182, 186], superfluid condensates and hereafter Bose–Einstein condensates. The foundations of high precision matter wave Sagnac gyrometers based on the generation of quantized vortices in superfluid ^{4}He and ^{3}He were laid by Avenel and Varoquaux [150–152, 155, 156] and Packards group [153] at the end of the 1980s and the middle of the 1990s. The state of the art of these gyrometers may be found in [154, 157–159, 177, 178] and, e.g. in the review paper [158].

In addition, Bose–Einstein condensates are very promising candidates for future precision Sagnac gyrometers, though some prerequisite elements for BEC interferometric rotation sensing are still lacking, e.g. proper wave guide loops [161] with in-guide coherent atomic beam splitter(s) to split and superimpose the coherent beams again in order to produce interference fringes. A key achievement on the way to a continuously operating atom laser and the realization of rotation/inertial sensors is the pumped single mode atom laser made from a Bose–Einstein condensate presented by John Close's team in 2007 [162].

Only recently both the ac and dc Josephson effects in a Bose–Einstein condensate with a single junction were observed [163]. In such quantum interference device working in the dc mode BEC condensed atoms should be able to sense rotation analogous to Cooper pairs in the superconducting quantum interference device used by Mercereau and Zimmermann in 1965 [130].

3.2.2. Sagnac experiments with matter and charged matter waves. As already mentioned, the first calculation which predicted the phase difference *for matter waves* between paths with an enclosed area on a rotating platform and the proposal of the corresponding experiment—more precisely, the particle equivalent of the Michelson and Gale's earth rotation experiment [136] and the Sagnac experiment—was presented by one of the pioneers of the ring laser technology, Heer [137, 138] at a Conference of the American Physical Society in 1961, before the predominantly cited proposal of Page in 1975 [139]. The latter proposal came just in time with the application of the 1974 invented interferometer for neutrons based on the Borrmann effect by Rauch *et al* [33]. The first experiments on the gravitationally induced phase differences of neutrons—including the neutron Sagnac effect—observed by the Missouri group (Colella, Overhauser and Werner) in 1975 [141] and the group around Rauch from Vienna were the beginning of a beautiful series of experiments

on the fundamentals of quantum mechanics with neutrons (see, e.g. [32, 34, 142–144]). The remarkable fact that the phase difference caused by rotation is proportional to the quantum energy of the electromagnetic radiation respectively to the total energy of the particles involved—which is the key for the extraordinary sensitivity achievable in matter wave gyroscopes (and accelerometers) with particles of large mass (neutrons, atoms) and charged particles (electrons and ions)—was not sufficiently stressed in these early experiments, presumably due to the progress in rotation sensing with ring lasers in the 1970s [147]. Therefore, the first publications on ultra high sensitivity achievable with matter-wave interferometers employing low-velocity heavy particles appeared only in the middle of the 80s [145, 146, 148]. In his excellent theoretical overview Clauser [146] calculates and predicts the—in the meantime largely realized—capabilities of rotational [160, 186, 188, 189] and accelerational [189] sensors with matter–wave interferometers employing low-velocity neutral atoms, and compares the sensitivities which can be achieved theoretically with state-of-the-art conventional mechanical and multiple circuit optical interferometers at that time. For example, a matter-wave interferometer working with a neutral sodium beam with a velocity of $50\,\mathrm{m\,s^{-1}}$ is more sensitive to rotation by a factor of $R_{\mathrm{gyro}} \sim 10^{10}$ compared with an optical interferometer at $\lambda = 500\,\mathrm{nm}$ and to acceleration by a factor $R_{\mathrm{accel}} \sim 10^{17}$. Clauser's overview ends with an extended discussion of possible configurations of such matter-wave gyroscopes and accelerometers including their experimental problems and obstacles. Today's state of the art may be found in [185, 186, 188, 189].

3.3. Sagnac experiments with ions and the outlook for new quantum gyroscopes

An ion biprism interferometer has been realized already a decade ago [193, 191] with the goal to develop it into a highly sensitive gyrometer [145, 190], to realize inertial and gravitational sensors of unprecedented precision on the one hand and on the other hand to test aspects of interaction of scalar and vector potentials (A–B effects) with these *composite charged particles* in relation to their inner structure which is fundamental for the understanding of gauge invariance. An advantage of ion interferometry compared with atom interferometers is that powerful optical components are available and need not be developed as for atom interferometers. In particular, compared with atom optics large enclosed areas are relatively easily attainable with the optical components at hand for charged particles. Even better, as we will see in the next paragraph, for charged particles an optical component is available that allows to shift coherent wave packets longitudinally relative to each other and thereby re-establish longitudinal coherence if it seemingly has been lost, e.g. caused by velocity differences on spatially different paths. In interferometers the overlap of the wave packets in the interference plane may be lost due to different path lengths from the source to the interference plane or due to different group velocities of the packets caused by local potential differences on parts of both paths (see section 3.4.2).

A short term goal in Sagnac interferometry is the proof of the fluctuations in the Earth's rotation rate Ω_{E} (fluctuations of the length of day) accessible at the $1 \times 10^{-9}\Omega_{\mathrm{E}}$ level [185] while on four orders shorter time scales tests of general relativity [200], e.g. proof of frame dragging by rotating matter (Lense–Thirring effect) will [179, 195–199] become available. A new class of—not yet realized—relativistic gravitational effects of quantum interference of electrons was proposed by Jeeva Anandan in 1984 already: to measure the gravitationally induced Schiff–Barnhill effect, the rotationally induced London moment and the modification of the A–B type of phase shifts, due to the general relativistic coupling of the electromagnetic field to the gravitational field [180].

Last but not least, the most challenging goal is the development of quantum gyroscopes using not uncorrelated particles but entangled ones. It has been shown [194], that such a quantum gyroscope ought to be about 10^8 times more sensitive to rotations than the standard one. This type of gyroscope would make it possible to measure the rotation rate of the universe Ω_{u} [201] which is, according to Gödel, on the order of $\Omega_{\mathrm{u}} \simeq 4 \times 10^{-19}\,\mathrm{rad\,s^{-1}}$.

3.3.1. Sagnac experiment with electrons. Clearly in the 1980s, from a fundamental point of view, an essential gap that remained to be closed in the domain of Sagnac interferometry was the realization of a Sagnac experiment with free charged fermions. The neutron interferometric experiments had shown coupling of the neutron mass to both gravitational [202, 141] and accelerational fields [203, 144, 204] at exactly the same value, thereby proving the validity of the classical principle of equivalence in the quantum limit. Although expected from theory, it is of fundamental interest and by no means trivial that the presence of charge, with its coupling to the electromagnetic field being so many orders of magnitude stronger, does not influence the electron's coupling to the accelerational field. It therefore seemed worthwhile to test—within the error margins—this fundamental assumption directly by using charged fermions in vacuum (and thereby avoiding the conceptual difficulties arising from using Cooper pairs, i.e. bosons, interacting with a solid state device).

A very intuitive view of the Sagnac effect of matter waves can be given in terms of the well-known twin paradox: it is well known (and experimentally proven with π-mesons traveling at high speeds and experiments with flying clocks [206–211]) that ageing is less in high speed travel because of the relativistic time dilatation phenomenon: a pair of particles (corresponding to wave packets) traveling clock- and counterclockwise with speeds $v+\Omega r$ and $v-\Omega r$ around a rotating disk show different times on arrival at the detector located at their starting point on the disk. Their time difference corresponds to a phase difference, the Sagnac phase shift $\Delta\phi$:

$$\Delta\phi = \frac{2E}{\hbar c^2}\vec{\Omega}\vec{A}. \tag{3.4}$$

This explanation of the Sagnac effect for massive particles demonstrates that the origin of the effect is relativistic. It is remarkable that the Sagnac phase difference is independent of the speed of the signals and depends on the angular velocity and the enclosed area only. While all variables return

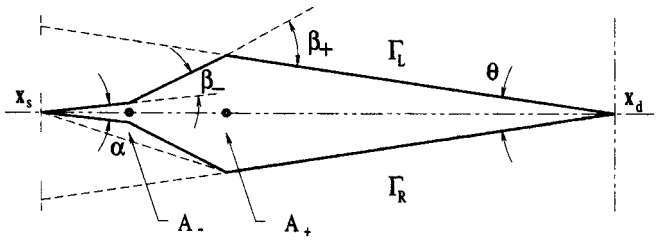

Figure 16. Geometry of the area enclosed by the separated classical paths Γ_L and Γ_R of the stationary interferometer. These paths were recombined at the surface of the primary interference, $x_d(\xi)$, where their angular convergence was θ. The distance from the cathode tip to the first biprism filament was a ∼36 mm; from the first to the second biprism filament $l = 40$ mm, and from the second biprism filament to $x_d(\xi)L \sim 100$ mm. Coherent beam separations were 20–60 μm.

to their original values after encircling the area, the phase does not (phase anholonomy) and gives rise to a shift of the interference fringes. In the parlance of geometrical and topological anholonomies (Berry phases) the Sagnac effect for massive particles is due to an age anholonomy when the twins are replaced by interfering particles [212]. In contrast, in classical physics, due to the assumption of an absolute time, the calculated arrival times of the particles at the detector in the inertial and rotating frame are identical. It is remarkable that *non-relativistic* quantum mechanics predicts the Sagnac phase difference correctly, which demonstrates that non-relativistic quantum mechanics is not in all respects a Galilean invariant theory [213, 214].

To perform the Sagnac experiment the whole electron interferometer was fixed on a turntable and put into CW and CCW rotation with exactly the same rotation rate in each experiment in order to avoid different centrifugal forces on the interferometer which could falsify the phase shift measured by the interferometer. The experiment was repeated at different rotation rates up to 1 Hz. Note that the beam path in the present Sagnac experiment is given in figure 16. It differs from conventional Sagnac interferometers where the starting and interference plane coincide, i.e. the beams travel a full closed loop. In the present experiment the beams travel semicircular paths only before they interfere. The values of the phase shift are 50% of the value given in equation (3.4). Our experiment was performed on the seventh floor of the building. No vibration damping was provided. The wavelength of the electrons was about 0.01 nm. The duration of one experiment was typically about 6 min. The phase difference caused by the CW and CCW rotation was ⩽6% of a fringe width. In order to limit the error bar in the experiment to less than 15% the sum of all errors (mechanical and electrical instabilities, drift) must not exceed 1% of a fringe width during the total duration of an experiment of 6 min. It turned out that the limiting factors of the rotating Sagnac interferometer were not mechanical nor electrical instabilities but the instability of the field emission. A summary of the result of the Sagnac experiment is given in figure 17 and a picture of the Sagnac interferometer for free electrons is given in figure 2.

As already mentioned, in all Sagnac experiments (neutrons, electrons, atoms) with exception of the experiment of Zimmermann and Mercereau with Cooper pairs [130]

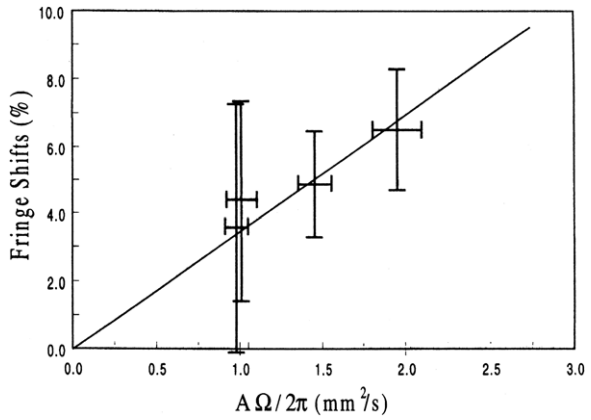

Figure 17. Sagnac phase differences for CW–CCW rotation in % of a fringe width for variations in the product of the rate of rotation $\Omega/2\pi$, and the corrected area enclosed by the interfering beams, A_{cor}. The solid line gives the theoretical prediction. The horizontal limits of error given in the diagram are due to the uncertainty in determining the enclosed area $\vec{A}$. All the details of the experiment may be found in [75] and [72] (the latter in German). A re-analysis of the experiment in 1997 [215] yielded a corrected expression for the projected area $\vec{A}$ and gave small numerical corrections to the previous work [75].

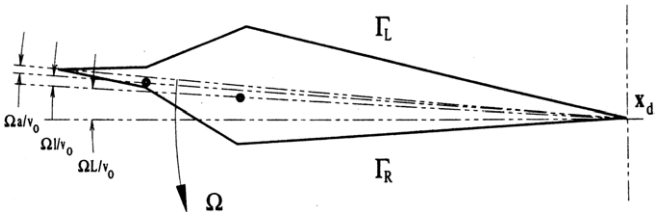

Figure 18. Geometry of the rotating interferometer as viewed from the inertial frame of reference (see text).

(they therefore call their measured inertial A–B phase shift a 'Sagnac-like' phase shift), the deflection of the interference field caused by the Coriolis forces in the rotating system has been measured which is numerically identical with the inertial A–B phase shift caused by the enclosed rotational flux. In the literature most of the time no distinction is made between these in essence disparate phase shifts. The one is caused by a force-free rotational flux and the other by the forces in the rotating frame of reference.

The re-analysis of the Sagnac experiment with electrons from an *inertial frame of reference* [215] makes explicit the central role of the *electrostatic A–B* phase shift caused by the electric potential distribution of the electrostatic biprisms. It becomes evident that the Sagnac phase shift measured in a biprism interferometer with charged particles differs significantly in physical origin from a similar experiment with neutrons: it is shown that kinematic phase perturbations, i.e. perturbation of the particle speeds by the Doppler effect and changes of the physical length of the path segments, make a negligible contribution to the observed phase shift. Likewise, magnetic fields caused by the, in the inertial frame of reference, moving biprisms make no contribution to the observed phase as the enclosed magnetic flux vanishes. Unique to the Sagnac experiment with electrons is that the rotationally induced phase shift is of electrostatic origin: figure 18 gives

the geometry of the *rotating interferometer as viewed from the inertial frame of reference*. During the propagation of the electrons from the field emission tip to the first biprism filament, the interferometer rotated through $\Omega a/v_0$ radians where a is the distance between the field emitter tip and the first biprism. Consequently, the impact parameter of the first, negative biprism for both paths Γ_L and Γ_R is perturbed. Similarly, in the time of propagation between the biprism filaments, the interferometer is rotated through $\Omega l/v_0$ radians where l is the distance between the biprisms. Likewise, the impact parameter of the positively charged biprism becomes perturbed. A further rotation of $\Omega L/v_0$ occurred before the classical paths are recombined in the interference plane $\boldsymbol{x}_d$ at distance L from the second biprism. Consequently, the *electron waves on both paths interact with different potentials and acquire different electrostatic (A–B) phase shifts*. Both the fringe system and the envelope are being translated together across the detector surface. With all the other contributions to the phase shift vanishingly small, the calculated phase shift recovers the formula for Sagnac phase shift. The Sagnac phase shift arises in this picture from perturbations of the electric potentials encountered by electrons when propagating through the rotating Sagnac interferometer, while in the experiment with neutrons of Werner *et al* [203] the Sagnac phase shift arises from rotationally induced path length differences.

3.4. The influence of electromagnetic potentials and fields on trajectories and phase of electron wave packets

3.4.1. The Wien filter: a wave packet shifting device for charged particles. In 1979, Möllenstedt and Wohland discovered in a Wien filter (crossed electric and magnetic fields, 'crossed field analyzer') a wave packet shifting device and measured the coherence length of electron waves [92, 95]. After completing his diploma thesis [65] in my group in 1977, Wohland was given his task for his PhD thesis by Möllenstedt. Möllenstedt had the idea of trying to combine a crossed beam analyzer (Wien filter), which was exclusively used at that time for analyzing electron energy spectra, with an electron biprism interferometer. The crossed beam analyzer was inserted into the biprism interferometer behind the electron optical biprism where the paths of the coherent waves were separated by some micrometers. Wohlands interferometer was a conventional one with a thermionic cathode of low brightness working with electrons of 20–30 keV and electrostatic lenses. It was already equipped with an image intensifier (which consisted of two channel plates in cascade, a fluorescent screen and a highly sensitive television camera) which he also had developed in his diploma thesis.

The first results with Wohland's combination of his biprism interferometer with a crossed beam analyzer were very disappointing. Nothing happened with the interference fringes when he increased the excitation of the crossed field analyzer. Neither did the fringes move nor an influence on the contrast was seen. Wohland tried to improve his interferometer without any success. After frustrating months, on some evening he switched off his interferometer under conditions of high contrast of the interference fringes with excited crossed beam analyzer. Next morning, after switching on the interferometer again the contrast of the fringes was—contrary to expectation—rather low. By analyzing the situation he found out that his high voltage supply had become defective and instead of producing 20 kV it delivered only about 2 kV. Amazingly, by varying the excitation of the crossed beam analyzer he was now able at a low voltage of 2 kV to improve and reduce the contrast of the interferences by varying the excitation of the Wien filter. After extensive tests his interpretation of the effect, namely that by the crossed field analyzer the overlap of the coherent electron waves can be adjusted, turned out to be right. For the first time it had become possible to measure the coherence lengths of electron waves directly [92, 95]. The failure of his high voltage supply turned out to be a lucky strike—similar to the implosion of the ultrahigh vacuum system in Davisson and Germer's experiment—to prove the wave nature of electrons in 1927 for the first time [2]. Wohland's discovery opened a gateway for new experiments and is of fundamental importance for electron interferometry especially at low energies.

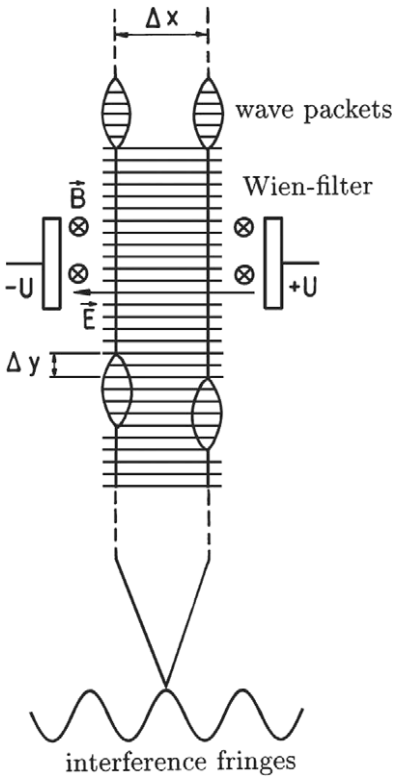

Figure 19. The influence of a Wien filter in its compensated state on two spatially separated electron wave packets. The lhs wave packet travels inside the Wien filter on a more negative potential than the rhs one, i.e. with a lower group velocity.

A brief outline of the action of the Wien filter on electron wave packets is given in figure 19. A Wien filter consists of crossed electric and magnetic fields, both perpendicular to the beam path. The Wien filter is said to be in its *compensated state* when the electric and magnetic force on the charged particles just cancel each other, i.e. the trajectories of the particles are not affected by the electromagnetic fields in the Wien filter. For the

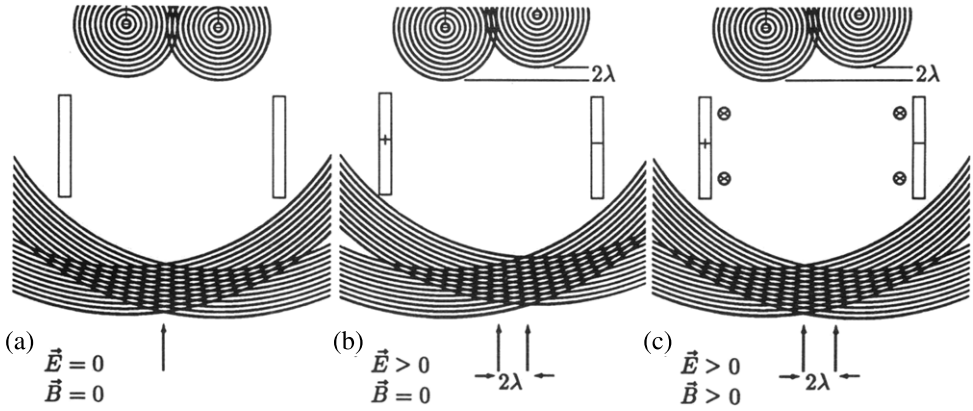

Figure 20. The two step process to reach the compensated state of the Wien filter. Electron wave packets emerging from two coherent sources traverse the Wien filter. (*a*) The Wien filter is switched off. A fringe pattern symmetric to the axis is observed. (*b*) As a first step the electric field is increased. Now, inside the Wien filter the packet on the rhs propagates on a more negative potential with a lower group velocity compared with that on the lhs. This is simulated in the figure by moving backwards the right-hand source by 2 wavelengths. As a consequence, the central maximum of the pattern is deflected by exactly 2 fringe widths to the right in (*b*). (*c*) Then, the magnetic field is increased until the deflection of the pattern is compensated. The wave packets now leaving the compensated Wien filter are shifted longitudinally by exactly 2 wavelengths, caused by the different group velocities of the wave packets traveling on the lhs and rhs inside the Wien filter.

case of the compensated Wien filter it can be shown easily (see, e.g. [98–100]) that the phase shifts exerted by the electric and magnetic potentials[1] are opposite to each other and of exactly the same magnitude. To state it differently, the electron optical index of refraction equals 1 (to first order) inside and outside the Wien filter. Therefore, in figure 19 the planes of equal phase[2] (e.g. crests) of the electron waves, represented by the horizontal lines, and the phase velocity are not affected at all by the electromagnetic fields in the *compensated* Wien filter, irrespective of its excitation.

That means, when we increase the excitation of the Wien filter while always staying in its compensated state, we observe in the observation plane a stationary field of interference fringes, *but*, with increasing excitation of the Wien filter fringe contrast is decreasing continuously. This is due to the fact that the electron wave packets travel on paths of different electric potentials with different group velocities inside the Wien filter. This leads to a longitudinal shift of the wave packets at the exit plane and consequently to a reduced contrast of the interference fringes[3]. For longitudinal shifts larger than the coherence length, fringe contrast vanishes. The contrast or, in the terminology of Michelson, the visibility V of the fringes as a function of the longitudinal shift x is defined by

$$V(x) = \frac{I_{max}(x) - I_{\min}(x)}{I_{\max}(x) + I_{\min}(x)} = G_1 \cdot G_2 \qquad (3.5)$$

and equals the product of the spatial (G_1) and temporal (G_2) coherence functions [101]. For coherence length measurements the fringe spacings are chosen so large by a suitable voltage on the biprism filament that $G_1 = 1$.

It is important to emphasize the fact that the *Wien filter in its compensated state is not a phase shifter*. The wave packets are shifted longitudinally in a stationary 'phase wave sea'. The phase of the wave packets is not affected at all when traveling through the electromagnetic fields in a compensated Wien filter.

3.4.2. Refinement of a Wien filter to a high precision device for shifting coherent wave packets longitudinally relative to each other. The construction of Wohland's Wien filter did only allow to vary its excitation in coarse steps corresponding to a longitudinal shift much larger than a wavelength. He therefore calculated the experimental value of the longitudinal coherence out of the electric and magnetic fields applied to his Wien filter at its excitation for just vanishing fringe contrast [92, 95]. This method is afflicted with faults larger than 10% (caused by errors of the strength of the fields, the influence of the not exactly known fringing fields and the geometrical data of the Wien filter). In order to overcome this drawback, the newly designed Wien filter allows one to adjust both electromagnetic fields independently in very subtle steps on the order of a percent of a wavelength. This very high precision is achieved when it is aligned to its compensated state by the following two step process (figure 20) [98, 100, 102, 105]: at first, both the magnetic and electric fields are zero (figure 20(*a*)). The full overlap of the wave packets corresponds to maximum fringe contrast. A fringe pattern symmetric to the axis is observed. Now we increase in a first step the *electric field* only. The

[1] Electric and magnetic A–B phase shifts [94]. The magnetic flux enclosed by the coherent beams creates a certain phase shift which is exactly compensated by the phase shift which arises due to the fact that the coherent wave packets travel inside the Wien filter on paths of different electric potentials. In essence, by taking into account the well-known experiments which prove the magnetic A–B effect, we have here an indirect proof of the existence of the electric (scalar) A–B effect [100].

[2] The lines of constant phase in all schematic diagrams do not represent reality but only one of an infinite number of possible equivalent descriptions due to the gauge freedom of the vector potential. Quantum mechanically, phase differences and the corresponding fringe spacings only are elements of reality [96, 97].

[3] The electric potential difference on the two paths increases with increasing excitation of the Wien filter. The acceleration and deceleration of the wave packets to the value inside the Wien filter occurs in the electric fringing fields of the Wien filter condenser.

Table 3. Coherence length measurements of field emitted electrons. The corresponding energy widths (ΔE_{FWHM}) were calculated (c) out of the coherence length respectively measured by visibility spectroscopy (m). For details, see text.

Author	Acceleration voltage (V)	Contrast ca	Fringes N_{fringes}	Coherence length L_c $L_c = N_{\mathrm{fringes}} \cdot \lambda_{\mathrm{de\ Broglie}}$ (nm)	ΔE_{FWHM}
Wohland 1981 [95]	5025	∼10%	5500	960	0.34 eV (c)
Gauch 1983 [105]	4000	$1/e$	21 800	420	0.43 eV (c)
Schäfer 1989 [106]	2000	20%	11 180	300	0.61 eV (m)
Wachendorfer 1993 [107]	2400	20%	12 320	310	0.59 eV (m)
Bauer 1995 [108, 109]	1700	10%	21 300	640	0.29 eV (c)
Bauer 1995 [108, 109]	1700	10%	39 620	1189	0.16 eV (c)

Wien condenser works as a deflection element. It produces a displacement of the interference field, say, by two fringe widths to the right (figure 20(*b*)). During the deflection from 0–2λ the 0th order fringe remains always in the middle of the fringe system: the *phase shift* caused for all path length differences $\Delta_1 = 0$–2λ from the two virtual sources to the 0th order fringe at the center of the deflected pattern is exactly compensated by different indices of refraction (different phase velocities of the coherent waves on their path to the 0th order fringe) or in another terminology, by different electrical A–B phase shifts. Otherwise the fringes within the envelope of the deflected pattern would be shifted in relation to the undeflected one and look differently (see also figures 14(*A*) and (*B*)).

The different arrival times caused by the path length difference and different group velocities of both wave packets inside the Wien filter add up to 4λ and are not compensated. Consequently, the overlap of the wave packets at the center fringe of the deflected pattern is reduced by an amount corresponding to 4 wavelengths with the corresponding effect on the contrast of the pattern. In the next step, the magnetic field of the Wien filter is increased until the deflection due to the electric field is just compensated. The electrostatic and the magnetic A–B phase shifts are opposite and equal in value and exactly compensate each other.

However, the longitudinal shift of two fringe widths or two wavelengths of the wave packets due to the different group velocities in the electric field survives. Consequently, the contrast of the fringe pattern after this two step process corresponds to a reduced overlap of the wave packets by two wavelengths. In order to measure the coherence length, this two step process is repeated until the contrast of the interference fringes reduced—according to the definition chosen—to 10%, $1/e$ or vanishes. Two times the number of fringes times the wavelength is the coherence length of the ensemble of electrons.

Let me mention here that *this measurement method works without any knowledge about the field strengths and (in)homogeneities of the electromagnetic fields in the Wien filter, not to mention that of the fringing fields. It therefore is intrinsically extremely precise and enables us to measure the longitudinal shift exerted by the Wien filter with a precision of the order of 1% of a wavelength or less*. This high precision was a prerequisite to realize Michelsons visibility technique and Fourier spectroscopy for charged matter waves.

3.5. Applications of the Wien filter

3.5.1. Measurement of coherence lengths of electron waves. In order to measure coherence lengths, the wave packets and their identical replicas are superimposed with different longitudinal shifts until the contrast C of the interference fringes is reduced to, e.g. $1/e$, 20% or 10% [103, 104] (according to different definitions of the coherence length).

Table 3 summarizes the results: in the first column the authors are given. The second contains the acceleration voltage of the electrons followed by the contrast limit C used by the specific author to calculate his coherence length. Fringes with contrast lower than C were neglected. The coherence lengths are the products of the total number of fringes with $C \geqslant$ this contrast limit, times the wavelength. The FWHM of the spectral distribution has been measured by visibility spectroscopy (m) respectively calculated (c) from the measured coherence lengths assuming symmetrical Gaussian distributions of the spectral lines.

The coherence length measurement of Wohland [92, 95] refers on a thermionic cathode emitting a spectrum symmetric to the center frequency. The other results relate to cold field emitters with their asymmetric spectra (concerning the symmetry of the spectra see also the remarks in the section on Fourier spectroscopy). The FWHM of the spectra given in table 3 were calculated (c) out of the coherence lengths respectively measured by visibility spectroscopy (m). In both cases the assumption of a symmetric spectrum enters into the calculation. We are aware, since the spectra of field emitted electrons are asymmetric, this is, strictly speaking, not correct.

In the last two rows of table 3 *the increase in coherence length by monochromatization of an electron beam* has been demonstrated experimentally [108, 109]. The experimental setup (figure 21) consists of an interferometer equipped with a first Wien filter for monochromatization and a second one working as a wave packet shifter.

3.5.2. Interferometric measurement of charged particle spectra à la Michelson and Rubens and Wood (visibility and Fourier spectroscopy). Classical charged particle spectrometers are based on the fact that particles with different energies follow different individual trajectories. Different arrival sites in the plane of observation correspond to different energies of the particles. The quantum mechanical counterpart of such a classical measurement is to extract the particle spectrum from the corresponding spread of the de Broglie

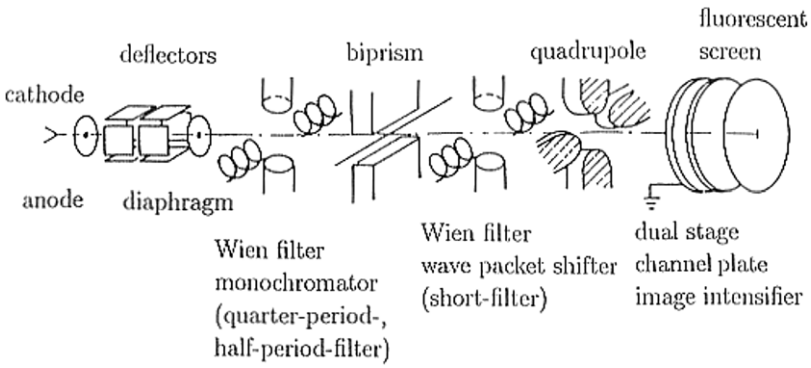

Figure 21. Set-up for measuring the coherence lengths as a function of the energy width of the electron beam. The first Wien filter acts as a monochromator, the second one as a wave packet shifting device.

wavelengths of the ensemble of particles which make up the wave packet. By wave front or amplitude division two coherent wave packets are generated. Then, a steady alteration in the difference in path length is introduced between the two interfering streams of electron wave packets. The flux of radiation as a function of the path difference between the beams arriving at the detector contains a constant term and an oscillating one, the interferogram. The interferogram, i.e. the contrast and the spacings of the interference fringes as a function of the path length difference between the beams, characterizes the incident spectrum that produces it, and is analyzed to yield the unique spectral distribution of the radiation reaching the detector. The salient point, of this type of spectroscopy compared with trajectory based spectrometers is that imperfections of the optical components have no influence on the observable quantity, the interference fringes of the matter waves. Consequently, their aberrations do not affect and limit the attainable resolution of this new type of charged particle spectrometer. The advantages of this technique cannot be summarized better than Michelson did in his seminal papers [110–112] on this subject in 1892, at that time for photons: 'The principal object of the foregoing work is to illustrate the advantages which may be expected from a study of the variations of clearness of interference fringes with increase in difference of path. The fundamental principle by which the "structure" of a line or a group of lines is determined by this method is not essentially different from that of spectrum analysis by the grating, both depending, in fact, on interference phenomena; but in consequence of the almost complete freedom from errors arising from defects in optical or mechanical parts, the method has extraordinary advantages for this special work'.

In his experiments Michelson did take into account only the visibility of the interference fringes $V(x)$ as a function of the path length difference x:

$$V(x) = \frac{I_{\max}(x) - I_{\min}(x)}{I_{\max}(x) + I_{\min}(x)} = G_1 \cdot G_2 \qquad (3.6)$$

and neglected the slight variations of their spacings. G_1 and G_2 are the spatial respectively temporal coherence functions. Spectral lines that appeared as singlets in ordinary spectrometers revealed, due to the better resolution of his visibility spectrometer, in fact as doublets or multiplets. However, neglecting the slight variations of the average fringe distances as a function of the longitudinal shift in the interferogram restricted Michelson's visibility technique to spectra symmetric about the center frequency. The complete information encoded in an interferogram was for the first time used by Rubens and Wood for spectral analysis in the far infrared region [113] of the electromagnetic spectrum.

3.5.3. The interferogram. Features of the spectrum of the radiation (the FWHM, the symmetry of the spectral line) are encoded in the interferogram in a characteristic way. This is demonstrated in the following computer simulation of an interferogram (figure 22). In figure 23 an experimental electron interferogram corresponding to the simulated one of figure 22 is given.

The interferograms shown in figures 22 and 23 correspond to a spectrum consisting of a symmetric doublet of lines of equal intensity. The envelope of the contrast of the fringes is determined by the widths of the lines, while the contrast minima are determined by the difference in frequency Δ of the two lines. It can be shown that for symmetric spectra the fringe widths are constant in the whole interferogram. However, for asymmetric spectra, the fringe width varies for increasing longitudinal shifts of the wave packets slightly in the interferogram. By Fourier analysis of such an interferogram the spectrum can be recovered in a unique way.

The 'interferogram' given in figure 23 was obtained in the following way: on the extraction voltage at the cathode of the interferometer of 1700 V a square wave voltage with an amplitude of 22 V and a frequency of few hundred hertz was superimposed. The two fringe systems are added on the chip of the CCD camera. The extinction of the lines at both sides of the center fringes is clearly visible.

3.5.4. 'Visibility spectroscopy' of electron waves. In the following model experiment the spectrum of a field emission electron gun has been measured. The contrast of the interference fringes was recorded quantitatively as a function of the longitudinal shift in the whole interference field consisting of about 15 000 fringes for the experimental parameters used in our low voltage interferometer (a few kiloelectronvolts of total energy of the field emitted electrons

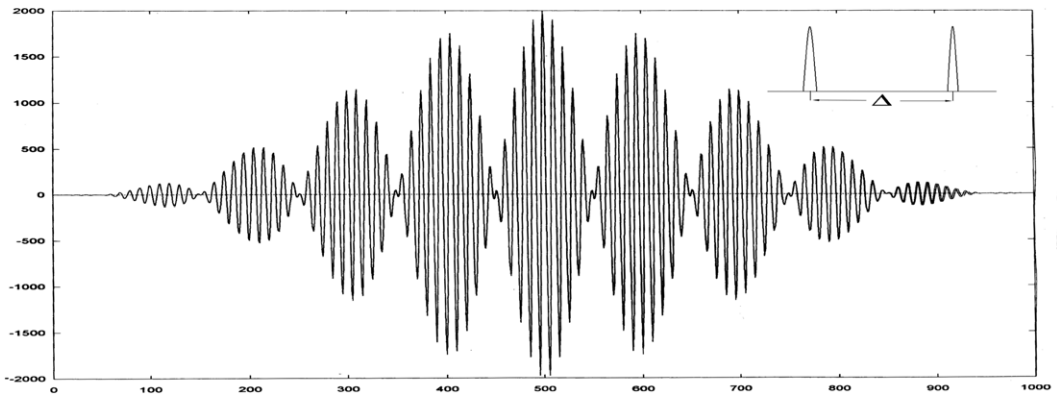

Figure 22. Computer simulation of an interferogram of a spectrum consisting of two Gaussian shaped spectral lines of equal intensity separated by an energy Δ (see inset).

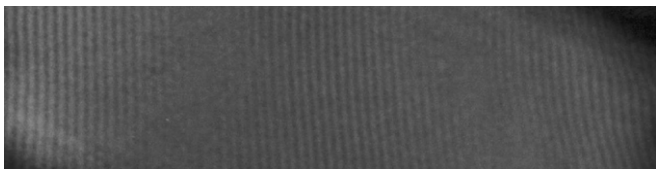

Figure 23. Electron interferogram corresponding to the central part of the simulated interferogram in figure 22. The energy of the electron 'lines' was 1700 eV and 1722 eV ($\Delta E = 22$ eV).

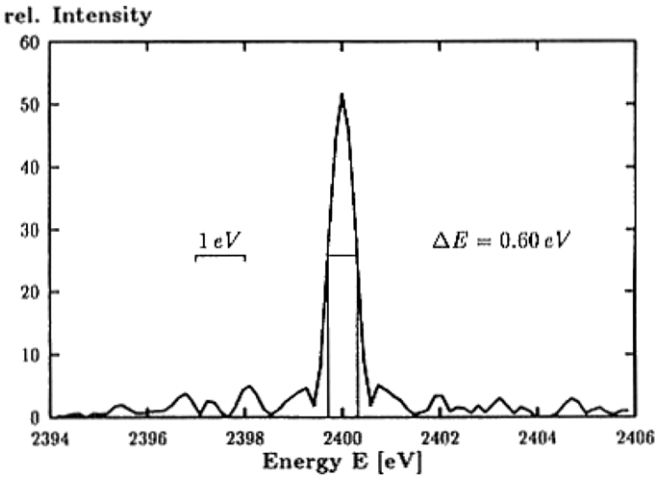

Figure 24. Spectrum of a field electron emitter obtained by visibility spectroscopy, total energy of the electrons: 2.4 keV, FWHM 0.6 eV ±80 mV.

at an energy spread of about 0.4 eV). This has been done by recording the whole interference field in sets of, e.g. 10 fringes successively with our CCD-camera densitometer. The digitized data sets were corrected for the (small) cylinder lens action of the Wien filter, put together with matched phases in a personal computer and subsequently transferred to a VAX computer for Fourier analysis. In the first experiment [102, 106, 114] a resolution of about 0.6 eV has been obtained. The state of the art is about 80 meV [107, 116]. As an example, the energy spectrum of field emitted electrons measured by this method is given in figure 24. This result was obtained by taking into account 12 300 interference fringes with a contrast of $\geqslant$10%. About 2000 low contrast ($C \leqslant 10\%$) fringes were neglected which results in an error of less than 40 meV of the FWHM of the spectrum given in figure 24. The total error of 80 meV contains 40 meV of error due to sampling of data (which can largely be avoided in future experiments). It is caused by the fact that from the recorded 128 sample points per fringe only 16 sample points per fringe could be used for Fourier transformation due to a limited main memory of the VAX computer. This resolving power of 80 meV surpasses that of many electron spectrometers which are used in analytical electron microscopes.

3.5.5. Further steps to reach the full capability of Fourier spectroscopy of charged particle waves. The following problems remain to be solved to reach this goal.

(a) *For spectral lines symmetric to the center (visibility spectroscopy).* The distance of the fringes in this case is constant in principle. Only the undesired focusing property (weak cylinder lens action) of the Wien filter has to be compensated. This disturbance of the fringe distances has to be corrected dynamically, i.e. the different values of excitation of the Wien filter for every set of fringes has to be taken into account and corrected for, before Fourier analysis of the interferogram is executed [116]. There are two choices to do this: the cylinder lens action could be counteracted electron optically by a suitably excited cylinder or quadrupole lens or it could be corrected mathematically by taking into account that the fringe spacing s becomes narrower with increasing excitation of the Wien filter according to $s \simeq s_0 - s_2 E^2$ where E is the electric field strength [115]. In other words, this advanced evaluation does neither use E or N—which has been used so far [116]—but take E/s as a transformation variable. E is obtained from the voltage of the Wien capacitor and the distance of the capacitor plates, the fringe spacing from the recorded fringe patterns. The proportionality factor can be gained from a calibration measurement. With this correction the high precision of visibility spectroscopy shall be fully exploited.

(b) *For spectral lines not symmetric to their center (Fourier spectroscopy).*

In addition to the correction which takes into account the focusing action of the Wien filter in a correct way, secondly the fringe system has to be recorded with high resolution in order to

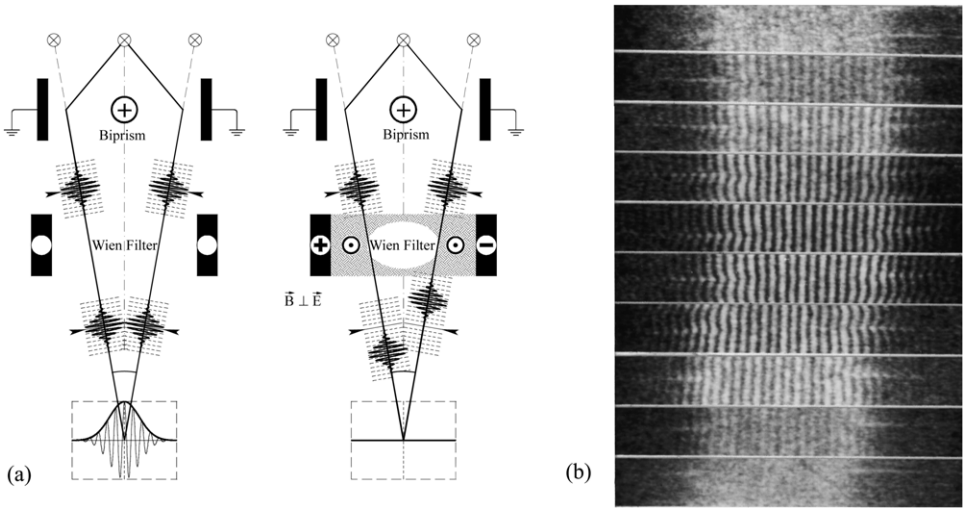

Figure 25. (*a*) Electron biprism interferometer with Wien filter switched off (left) and Wien filter in its excited state (right). The wave packet shift exceeding the coherence length leads to the disappearance of interference. (*b*) Restoration of contrast by a Wien filter. The longitudinal shift of the wave packets caused by electrostatic deflection elements (top) can be compensated (middle) and overcompensated (bottom) with the Wien filter [99, 100]. As we have seen the contrast in a system of interference fringes decreases when it is deflected due to the now different path lengths, e.g. to the 0th order fringe. When for aligning the electron interferometer the deflectors have to be excited strongly, it can happen, that no fringes are seen on the screen of the interferometer. Only after exciting the Wien filter in the appropriate direction the fringes become visible (as demonstrated in (*b*)).

capture the slight variations of the fringe spacings caused by the asymmetry of the spectral line. With this additional correction Fourier spectroscopy with matter waves should exhibit the same excellent resolving power as for electromagnetic waves.

In order to suppress the intensity modulation of the biprism fringes caused by diffracted waves at the edges of the biprism filament and avoid associated complications, the recently developed methods to record interferograms 'without', Fresnel fringes can be applied.

Today, limited memory size and speed of the computer are overcome. Data acquisition can be done computer controlled on the order of minutes or faster. As we have seen the Wien filter is an extremely simple and easy to include electron optical component, e.g. into analytical electron microscopes. These microscopes are frequently already equipped with biprisms and video systems for holograpic applications and could be upgraded (by addition of a simple Wien filter, a fast computer for control of the Wien filter and evaluation visibility spectra) into spectroscopic instrument at moderate costs.

3.5.6. In a nutshell. The Wien filter has proven to be a versatile instrument to measure coherence lengths on the one hand and spectra of charged particle beams on the other. The last-mentioned possibility, the visibility/Fourier spectrometer for charged particles (experimentally realized for electrons), is the *first spectrometer for massive particles that fully relies on quantum mechanics, i.e. the wave properties of matter*. It is remarkable that *this experiment proves that the quantum mechanical probability waves exhibit the same features as 'real' waves*, e.g. those of an electromagnetic field. All *conventional* spectrometers for charged particles are based on the dispersion of particle trajectories in electromagnetic fields.

After these applications of the Wien filter to applied problems, we now turn our attention to the solution of fundamental problems in quantum mechanics with the Wien filter. As we will see in the next section, an electron interferometer equipped with a Wien filter is suited for which-path experiments, as a quantum eraser and to investigate decoherence.

4. The Wien filter as a tool to investigate the fundamentals of quantum mechanics

4.1. The Wien filter as a 'Welcher Weg' experiment

In an interferometer, the Wien filter acts on a wave packet for which the *matching condition is fulfilled* merely as a wave packet shifter and leaves the phase difference unchanged (see arrows pointing at the center of the wave packets in figure 25(*a*)). The wave packet shift is caused by different electric potentials on the two laterally separated paths in the Wien filter leading to different group velocities, the vanishing phase difference is due to opposite and equal phase shifts caused by the electric scalar and the magnetic vector potential. The decreasing overlap of the two parts of the wave packets with increasing excitation of the Wien filter (compensated magnetic and electric A–B phase shifts) leads to a continuously decreasing fringe contrast while the fringes within their envelope remain stationary (figure 25(*b*)). The deflection by the electric field is exactly compensated by that of the magnetic field.

It should be noticed that for the Wien filter, phase relations between different energy components building up the wave packet do not matter—at least for *narrow* energy distributions. Therefore, e.g. for a mixed state which can be decomposed into monochromatic waves the contrast-reducing effect on the interference pattern turns out to be the same, provided that the energy spectrum equals that of the pure state of the wave

packet, only the mechanism of the reduction of contrast being different: in the case of the ensemble of monochromatic waves with statistically distributed phases it is the displacement of the incoherently superimposed intensity distributions relative to each other whereas for the wave packet it is the decrease in overlap or the non-stationarity of the phase difference between the two parts of the wave packet. It should be noted that the spreading of the wave packets with time (i.e. downstream the interferometer) does not affect the coherence length [100].

For the Wien filter, the reason for the loss of contrast in the interference pattern is the same as in a light interferometer with different lengths of the arms. And of course the loss of contrast can *also* be interpreted as being due to the increasing possibility of getting which-path information arising from the different times of flight of the two wave packets—though in present experiments we cannot really *get* this information because of the lack of knowledge of the instant of time when the electron was emitted.

By increasing the excitation of the Wien filter we get a continuous transition from complete interference to complete which-path information (see figure 25(*b*)) (cf [100, 218–220]. This allows to test the inequality

$$\mathcal{V}^2 + \mathcal{D}^2 \leqslant 1 \tag{4.1}$$

between visibility $\mathcal{V}$ and distinctiveness $\mathcal{D}$ derived for the first time by Glauber [217] (similar relations were found in [221–223] and [245] based on information theory resp. coherence considerations). But because the spreading of the wave packets leads to an increasing overlap between them, the time of arrival becomes more and more unsuitable as an observable W for measuring the distinctiveness [221] when the distance to the source is increased.

The delay between the two wave packets caused by the Wien filter can, loosely speaking, also be seen as a kind of entanglement: if we write the ordinary state space of the particle as a tensor product of the state space $\mathcal{X}$ of positions on the detection screen and of the state space $\mathcal{Z}$ of positions orthogonal to that screen (i.e. along the optical axis z), then because of the longitudinal distance Δz of the positions of the maxima of the partial wave packets we have entanglement with states in the space $\mathcal{Z}$. Yet this is only fully justified if the state of the split wave packet before entering the Wien filter is itself not an entangled state but a direct product state in $\mathcal{X} \otimes \mathcal{Z}$, but in this case we really have entanglement with increasingly orthogonal states in $\mathcal{Z}$ when the excitation of the Wien filter is increased.

4.2. The Wien filter as a decoherence free quantum eraser

By combining two Wien filters with opposite excitation, the effect of the first of these can be undone. Again, this can be interpreted in different ways, either by the loss of 'Welcher Weg' information or by the fact that the z-coordinates of the maxima of the two parts of the wave packet are made equal again. The second Wien filter can be looked upon as a quantum eraser, but with the difference that we do not loose intensity by this process. This is because we do not project onto—or at least detect in correlation with—a 'labeling space' state (of which both packets have equal components), but instead equalize the two labeling states.

Furthermore, *this demonstrates that coherence is not lost but only hidden after the first Wien filter. Figure 25(b) shows how interference which is absent on the top of figure 25(b)*[4] *is restored by the Wien filter. This makes it evident that there is no irreversible interaction of the electron with the electromagnetic fields or with the environment, i.e. no decoherence has taken place.*

5. Interferometric measurement of decoherence of electron waves and visualization of transition from quantum to classical behavior

The quantum mechanical behavior of microscopic particles characterized by the fact that they can be in superpositions of macroscopically distinct states (like Schrödinger's cat) contradicts our every day experience. This riddle has been solved with the advent of the theory of *decoherence* founded by Zeh in 1970 [224] and Zurek and Joos [225–227]. Decoherence, i.e. classical behavior, emerges as a consequence of unavoidable and in general irreversible interaction with the environment. Macroscopic objects, in particular, can never be sufficiently isolated from their environment due to their closely spaced energy levels, i.e. they constitute an open quantum system. Objects interacting with an environment get entangled with this environment, thereby phase relations between the formerly superposed object states are distributed over the total system. Then by looking on the object alone, no phase relations can be observed—phase coherence seems to be lost. Consequently, the object state appears to be an incoherent mixture instead of a superposition, i.e. one seems to deal with a classical ensemble.

In order to study the transition from quantum to classical behavior a microscopical object is the only choice. Only these quantum objects do not decohere instantaneously due to the fact that their energy levels are not closely spaced and a large gap between their ground state and the excited states exists. In order to decohere such a microscopic quantum object it has to be coupled deliberately to an environment of adjustable strength. Quantum mechanical behavior is characterized by the existence of interference fringes. The disappearing of these fringes with increasing coupling to the environment is the signature of the set in of decoherence. This onset of decoherence has been demonstrated in matter-wave interferometers caused by the emission (e.g. [228, 229]) and escape of photons [230], due to collisions with gas molecules (e.g. [231]) of the environment or decoherence through coupling of a single trapped ion to three types of different engineered quantum reservoirs: by coupling to a high temperature amplitude reservoir, to a phase reservoir and to quantum noise at zero temperature (spontaneous emission reservoir) [232, 233].

The electron interferometric experiment presented here [234–236] traces back to a proposal of Anglin and Zurek

[4] In the case of figure 25(*b*) it was caused by longitudinal shifts of the wave packets in electrostatic deflection fields for alignment of the interferometer and not by an additional Wien filter.

[237, 239] in which a novel mechanism of decoherence is investigated, Coulomb interaction with a truly macroscopic and dissipative environment, namely the electron and phonon gas inside a resistive plate. This experiment resembles the action of decoherence in the 'real' world. As a quantum mechanical object a free electron is used. The electron is one of the most elementary particles, and due to the absence of magnetic fields in the set-up, its spin is irrelevant. Consequently no inner degrees of freedom can be excited and entangled with the center of mass coordinates. Decoherence is exclusively caused by electromagnetic interaction through irreversible deposition of energy into the environment made up of the resistive decoherence plate.

5.1. Experimental set-up

For the experiment a biprism electron interferometer [22] of the compact rigid type [67] was used. As environment, a semiconducting plate (see figure 26) is employed, namely a piece of an n-doped silicon wafer with a resistivity of 1.5 Ω cm and a length of 10 mm. The electron beam emerging from a cold tungsten field emitter (diode system; acceleration voltage 1.665 kV) is split into two parts by a negatively charged electron optical biprism filament (diameter less than 1 μm) which also deflects them apart from each other. They are redirected toward each other by an electrostatic quadrupole with its electrodes in the plane of the beams negatively charged (see figure 26; only the beam path of an electron impinging on a certain point in the primary interference plane is shown in the figure). Before the two parts of the beam meet again, they travel over the resistive plate with a lateral separation Δx at exactly the same, small height z. Fine adjustment of the beams with respect to the plate is achieved by deflectors and coils (not given in figure 26). Where the two beams merge, an interference pattern is formed which is then magnified by electrostatic quadrupoles (also not shown in figure 26). Its intensity is amplified by a dual-stage channel plate image intensifier, transferred to a CCD camera by tapered fiber optics and evaluated with an image processing system.

When an electron passes a conducting plate (see figure 26), it induces charges in the plate. As the electron moves, so does the induced charge. According to Anglin and Zurek [237, 239], the resulting current inside the plate encounters ohmic resistance; this leads to dissipation, there is Joule heating which quantum mechanically means that the state of the electron and phonon gas inside the plate is disturbed. However, in his quantum theoretical calculation, Machnikowski [244] came to the conclusion that already the process of formation of the image charge is to a large extent dissipative, even if there is no carrier-phonon scattering and heating is due to excitations of the electron gas alone. But in any case, the heating, respectively disturbance, is located at different places for the two parts of the electron beam. This can equivalently be interpreted either [239, 244] in terms of the availability of which-path information (which is not actually read out in the experiment) or in terms of entanglement between beam electron and plate. Because dissipation is an irreversible process, a record of the electron's path remains even when the electron has passed the plate. As a consequence, the visibility of the interference fringes is reduced when the two parts of the beam are recombined. The disturbance of the electron (and phonon) gas is the stronger the closer the beam electron passes the plate, and the two disturbed states corresponding to the two paths of the electron are the more orthogonal to each other the larger their lateral separation is (until the disturbed regions are sufficiently separated). So decoherence is expected to increase with decreasing height z above the plate and with increasing lateral separation Δx between the two interfering paths. Varying Δx and z allows one to investigate the dependence of decoherence on two parameters. By sending electrons in different heights through the interferometer and accumulating the arrival sites at the image intensifier, the transition from quantum to classical becomes directly observable in a single interferogram: the fringe contrast decreases continuously with decreasing distance z from the plate (see figures 26 and 27). The lateral separation between the beams can be varied by adjusting the biprism voltage.

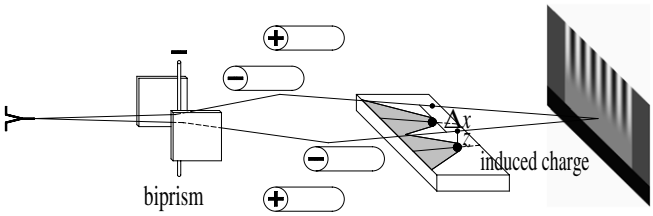

Figure 26. Sketch of the decoherence experiment. Electron waves emerging from the source are split by the negatively charged biprism filament, placed between earthed plates, and deflected apart from each other. The electrostatic quadrupole directs them toward each other again. Before they meet, they travel over a resistive plate at the same, small height z, but with a lateral separation Δx. The induced charges moving with the beam electron lead to a disturbance in the electron (and phonon) gas inside the plate. For the two electron trajectories, the corresponding disturbance (shaded areas) is located in different regions. Therefore entanglement between beam electron and plate is formed. The available which-path information increases with decreasing height over the plate, leading to decreasing fringe contrast in the interferogram (rhs). On the bottom of the fringe pattern the shadow of the plate is visible in black.

5.2. Results

Figure 27 shows the interference fringes in heights above the plate ranging from $z \approx 0\,\mu$m (bottom) to $z \approx 28.5\,\mu$m (top), for different values of the lateral separation Δx between the interfering beams. The decrease in fringe visibility with decreasing height above the plate is due to decoherence alone. The decrease in visibility from (a) to (h) is caused by both increasing decoherence and decreasing angular coherence for smaller fringe spacings. The latter effect had to be corrected for in the quantitative analysis of decoherence (figure 28). The values for the height z were calibrated by mechanically moving the plate with a micrometer screw. The values for the lateral separation Δx (at the position of the plate) were taken from ray-tracing simulations using transfer matrices [238].

In order to extract quantitative data out of the set of interference patterns given in figure 27 corrections to

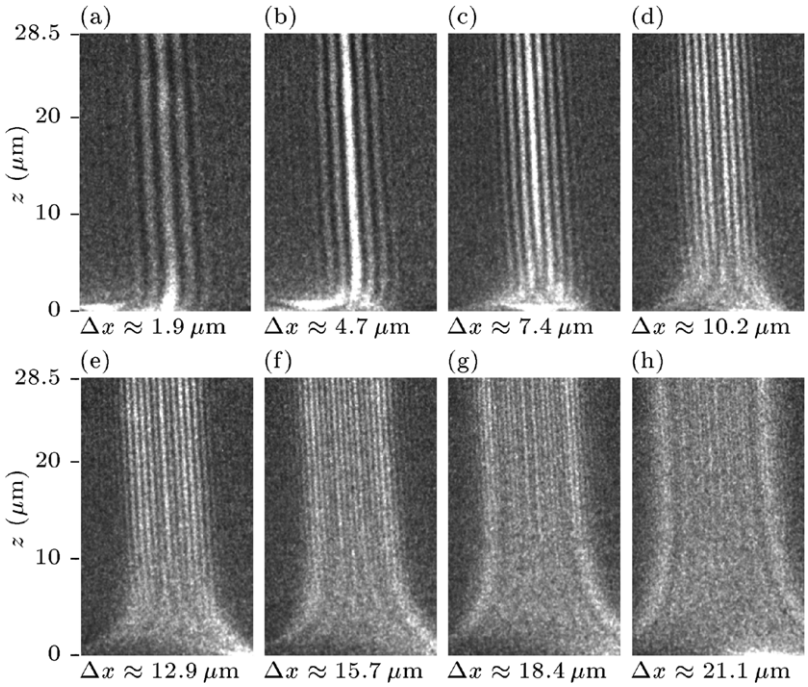

Figure 27. Electron interferograms showing continuously increasing decoherence with decreasing height z above the plate. The lateral separation Δx between the interfering beams increases from (a) to (h), causing both increasing decoherence and decreasing angular coherence. The bending of the area of overlap between the two parts of the beam and also of the interference fringes in the vicinity of the plate is due to the charging of dust particles on the surface of the plate. As this effect occurs only for very small heights in which fringe visibility is already nearly zero, it does not deteriorate the results. The shown CCD images are flat and dark corrected.

exclude deficiencies of the image acquisition system, the background of scattered electrons, modulation of the intensity interference fringes by Fresnel diffraction, the influence of angular coherence etc—in order to mention only the most important ones—are indispensable. Detailed discussion of all of these corrections may be found in [235, 236]. An effect that is not taken into account is decoherence due to vacuum fluctuations in empty space or in the vicinity of a perfectly conducting boundary. The Casimir effect [240] would likewise reduce fringe contrast, but this effect is much smaller [240] than the observed decrease in visibility. To conclude, in the present experiment decoherence due to dissipation in the semiconducting plate is the only possible explanation for the observed decrease in 'relative' visibility shown in figure 28.

In the original proposal by Anglin and Zurek [237, 239] a classical estimation of the expected strength of decoherence is given, based on the dissipation rate. Using the connection between relaxation time and decoherence time [241] in the form given by Joos [242], Breuer and Petruccione [243], and Zurek [227], the decoherence time should be $\tau_{\mathrm{d}} = 4h^2z^3/(\pi e^2 k_{\mathrm{B}} T\rho\,(\Delta x)^2)$ where h is Planck's constant, e is the elementary charge, k_{B} is the Boltzmann constant, T is the temperature (our experiment was conducted at room temperature) and ρ is the resistivity of the plate. The formula should be valid for $z \gg 4\pi\epsilon_0\rho v$, where ϵ_0 is the permittivity of vacuum and v the velocity of the beam electron. The relative visibility should then be given by $\mathcal{V}_{\mathrm{rel}} = \exp(-t_{\mathrm{flight}}/\tau_{\mathrm{d}})$ with t_{flight} being the time of flight of the electron over the plate. The fits (fit parameter b) to the experimental data with $\exp(-b/(z/\mu\mathrm{m})^3)$ are also shown in figure 28 (dashed lines), together with the values for b. The agreement between fit and experimental values is not perfect, but reasonable. b is expected to be a quadratic function of Δx, which is very well fulfilled (figure 28(h)), giving a fit factor [235] $a = 10.9$ for the fit $b = a \cdot (\Delta x/\mu\mathrm{m})^2$. The numerical strength of decoherence, however, is smaller in the experiment by a factor of 106; calculation of errors [235], accounting for uncertainties in $\mathcal{V}_{\mathrm{rel}}$, Δx and z, yields $a = 10.9^{+13.6}_{-5.8}$ while the value resulting from Anglin and Zurek's calculation for the parameters in the experiment is $a_{\mathrm{theor}} = 1159 \pm 353$. Stimulated by our experiment, Machnikowski [244] has done a calculation using the many-body quantum description of the electron gas. Although his theory is worked out for metals, the decoherence effect is expected to be qualitatively similar for semiconductors [244]. Machnikowski predicts a dependence of visibility according to $\mathcal{V}_{\mathrm{rel}} = \exp(-f \cdot \gamma(\Delta x/z))$ with the 'geometrical' function $\gamma(\Delta x/z) \approx (\pi/16) \cdot (\Delta x/z)^2$ and a prefactor f not yet known for semiconductors. The fits with this function yield slightly different parameters f for the individual values of Δx. Calculation of errors [235], again accounting also for uncertainties in $\mathcal{V}_{\mathrm{rel}}$, Δx and z, gives $f = 4.13^{+4.59}_{-2.01}$. The normalized visibility function $v_{\mathrm{rel}} = \exp(-f \cdot \gamma(\Delta x/z))$ with $f = 4.13$ is plotted as solid lines in figure 28 and is in really good agreement with the experimental data.

In conclusion, pictures of the continuous transition from quantum to classical behavior have been recorded. The results confirm the main features of the theory of decoherence. Quantitatively, the decrease in visibility and the corresponding decoherence times are in reasonable to very good agreement

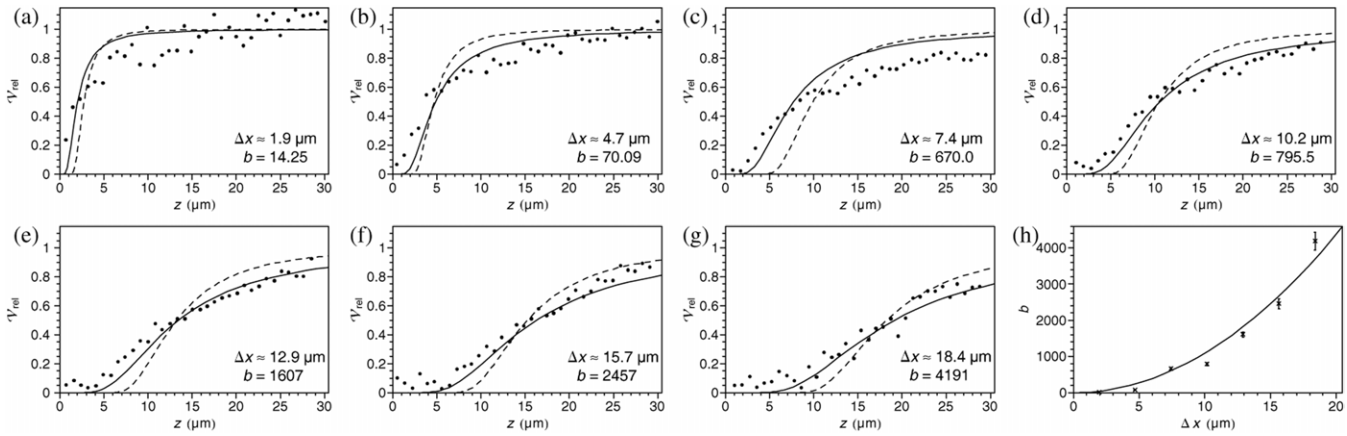

Figure 28. Quantitative results of the decoherence experiment. (a)–(g) 'Normalized' visibility $\mathcal{V}_{\rm rel}$ (corrected for the influence of angular coherence, etc, see text) as a function of height z, for different lateral separations Δx between the interfering beams. Dots: visibility determined from experimental data; dashed line: fit with $\exp(-b/(z/\mu\mathrm{m})^3)$ according to Anglin and Zurek's calculation [239, 237]; full line: $\exp(-f \cdot \gamma(\Delta x/z))$ with $\gamma(\Delta x/z) \approx (\pi/16) \cdot (\Delta x/z)^2$ and $f = 4.13$ resulting from the fits corresponding to Machnikowski's calculation [244]. The fluctuations of visibility are mainly due to shot noise (especially in (a)), and for (g) due to the fact that fringe spacing is not much larger than the pixel size. The magnitude of the visibility fluctuations for (a)–(g) is 0.101, 0.054, 0, 028, 0.039, 0.040, 0.057 and 0.067, respectively. The interferogram in figure 27(h) was not used for evaluation because of its low signal-to-noise ratio, caused by lack of angular coherence at large lateral separation of the interfering beams. (h) Δx dependence of the parameter b in the fits (a)–(g) according to Anglin and Zurek's calculation: data points and fit with $b = a \cdot (\Delta x/\mu\mathrm{m})^2$.

with existing theoretical results. Last but not least, the data will also be valuable for the advancement of current theoretical models—the initial purpose intended by Anglin and Zurek's proposal [239, 237] and one of the reasons why they called this experiment a 'precision test of decoherence'. An interesting extension and continuation of the experiment would be to substitute the present resistive environment by a superconductor or a high temperature superconductor and observe the decoherence as a function of this 'environment' as a function of temperature particularly near the transition point from normal to superconductivity.

6. Biprism interferences with charged atoms, He^+-ions

While diffraction of atoms has been realized [4] shortly after de Broglie's hypothesis that matter is associated with a wave, the first atom interferometers were put into operation only in the early 90s [369, 370]. One cause for this long delay has been the missing technology necessary to develop optical components for neutral particles. On the other hand, powerful optics for charged particle interferometers have been available since the 1950s (with the corresponding ease of manipulation of these). In 1964 a first attempt to realize an ion biprism interferometer ventured by Rösch in Tübingen [192] failed due to the lack of a concept of a highly stable interferometer for charged particles. This is not really surprising, having in mind that the wavelength of lightest ions at 20 keV is in the range of a tenth of a picometer or less, and as a consequence, extreme requirements on mechanical stability must be satisfied. With the miniaturized type of interferometer [67] Maier dared an experiment and realized the diffraction at the edge and biprism interferences with helium ions [190, 191, 193]. Ion interferometers are expected to supplement and—taking into account the additional parameter 'charge'—complement atom interferometry. They supplement fundamental tests of quantum mechanics and relativity, multiparticle interferometric effects [371], development of inertial sensors with unprecedented sensitivity [145, 146]. For the latter experiments waveguides and coherent beam splitters, which are available for ions already, are under development for atoms. *Charged atoms* couple to the electromagnetic field and therefore complement atom interferometry in a unique way. For example, due to the internal structure of ions an ionic A–B experiment will be the crucial test whether the phase shift caused by electromagnetic potentials depends on internal degrees of freedom of ions or is the same as for structureless 'point' particles as electrons.

6.1. Experimental set-up

The experimental set-up of the interferometer for ions is presented in figure 29. It uses wavefront division by an ion optical biprism whereby a true physical separation of the coherent ion wave packets in space is achieved. In essence, it is a modified type of our electron interferometer [67], which has proved to be extraordinarily rugged, insensitive to vibrations and electronically stable. The requirements which must be met in an ion interferometer with respect to mechanical stability and insensitivity to vibrations are even more stringent than that in atom interferometers. While in atom interferometers thermal beams with wavelengths on the order of an angstrom are used, in the present experiment the wavelengths of the ions of some kiloelectronvolts in energy are a fraction of a picometer only. An advantageous feature of the field ion source incorporated in the instrument is that it can be switched between ion and electron emission. Since all optical components of the interferometer are electrostatic, this gives us the possibility of a rough prealignment of the interferometer optics with a high intensity beam of field emitted electrons.

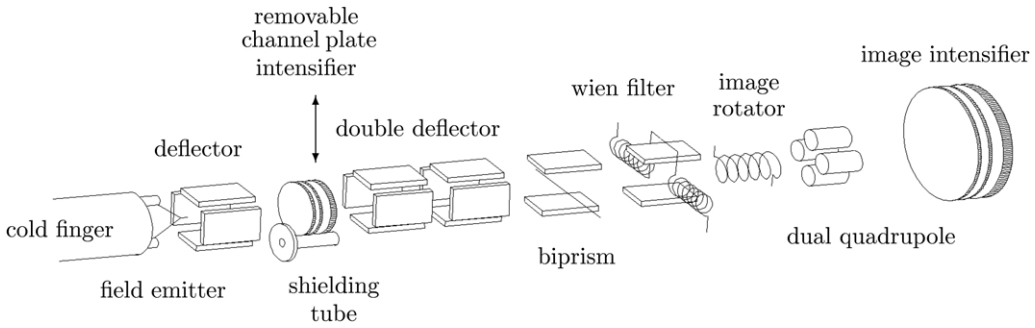

Figure 29. Schematic set-up of the ion interferometer.

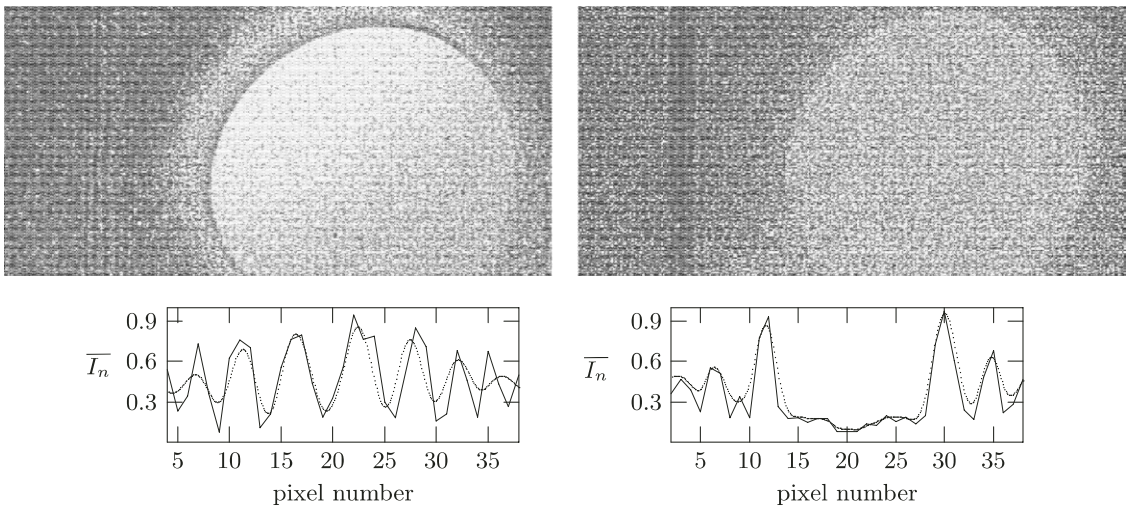

Figure 30. Biprism interferences (left) and diffraction at both edges of the biprism filament (right) with 3 keV helium ions. The lines are raw data summed-up over 50 pixel lines, the dotted line scans are low-pass filtered and spline-interpolated data. $\overline{I_n}$ is the normalized mean intensity.

The very small part of the current of ions which is emitted into the tiny angle where the interference fringes are formed ($\sim 10^{-7}$) and the—according to the literature about supertips not expected—very low brightness of our field ion emitter leads to exposure times as long as 30 min. The primary interference pattern is magnified by two cascaded electrostatic quadrupole lenses (without drift space in between) and intensified by two cascaded channel plates. The fringe pattern is transferred by a tapered fiber optic from the fluorescent screen to a cooled slow scan CCD camera.

6.1.1. The field ion source. In order to maximize the coherent flux of He^+-ions emitted by the field ion source, we use a specially treated 'supertip' [309], cooled down during operation to 77 K. The 'supertip', i.e. a protrusion consisting of a small number of tungsten atoms on a [1 1 1]-oriented tungsten field emission tip, which has a relatively large radius of curvature of the apex, is prepared *in situ* in the interferometer. During preparation, its emission pattern can be controlled on the screen of a channel plate image intensifier, which is inserted temporarily between ion source and interferometer (figure 29). After preparation, the source is emitting into a single spot of angular diameter of about 1° only. The brightness of our present source is rather low (10^3 A cm^{-2} sr^{-1} at 77 K). More details about the ion source are given in [190, 193]. In order to achieve a substantially improved brightness as a next step, we will lower the temperature of the tip to about 10 K.

Besides brightness, to achieve stable emission from one single site with atomic dimensions during the whole exposure time of about 30 min and a lifetime of the 'supertip' of at least 60 min turned out to be one of the greatest problems. More than 100 differently processed [1 1 1]-oriented and [1 0 0]-oriented tungsten field emission tips were evaluated experimentally. The ion biprism interference fringes and the diffraction of ions at both edges of the biprism filament given in figure 30 were obtained with a [1 1 1]-oriented tip with a total lifetime of about 2 h.

6.1.2. Image pick-up and processing. An ideal detector for our purpose has high detection efficiency and detective quantum efficiency (DQE) [372] for single ions. Exposure times of about 1 h, live observation of incoming single ions and simultaneous presentation of the events integrated in time on the screen of the image processing system should be possible. The DQE describes the reduction of the signal-to-noise ratio of a detector system and characterizes its quality. For our present system of two cascaded channel plates the DQE is limited to $\leqslant 0.5$ by the pulse-height distribution caused by the statistically varying scintillation intensities of the fluorescent

screen. Standard acquisition schemes, e.g. on-chip integration, do not surmount this low value of the DQE.

Fortunately, for a small number of events per second (low ion current), a normalization technique can be applied which improves the DQE of our detection system to about 0.8 for low mass ions with an energy of 2 keV. This image pick-up technique is applicable only if, within the exposure time of a frame, multiple events in a single pixel can be excluded (about 400 ms for our system). It works as follows: due to the statistics of the multiplication process in the channel plates the intensity of single event scintillations varies. Usually it exposes not a single, but a small number of adjacent pixels of the CCD chip with different intensities. The pixel intensities are digitized and stored in the frame grabber. The frames are corrected by subtraction of a mean dark current frame. Then, the intensity stored in every single pixel has to pass an adjustable threshold which suppresses remaining dark current and read-out noise. Only real signals survive this process and contribute to the frame. For each single event, the pixel with maximum exposure is localized and normalized to the minimal discernible intensity step: one gray level. The localized and normalized pixels are written into the corresponding pixels of a second frame memory. This process is repeated, until a frame with an exposure time of, say 20 min is accumulated in this second memory. This processing completely suppresses dark current noise, signal independent noise and pulse height statistics of the channel-plates for bright single-event scintillations (which can be achieved by high channel plate gain). Therefore, in addition to the improved DQE of about 0.8, dynamic range and spatial resolution of the frames are superior to those taken with the standard procedure.

6.2. Results and discussion

After several test series with the purpose to optimize the brightness and stability of the ion source and some tests of the interferometer stability we succeeded in recording diffraction at both edges of the biprism filament and biprism interference fringes [190, 191, 193]. The results are shown in figure 30. The bright round area in the middle of the pictures is a shadow of a diaphragm located near the field ion emitter and is either caused by beam ions neutralized near the field emitter tip, ultraviolet recombination radiation or excited neutral atoms releasing electrons at the entrance of the channel plate image intensifier. In reality, this area is much brighter than is seen in the pictures. By introducing an upper brightness threshold the intensity is cut to the intensity visible in figure 30. Within the bright area ion interferences are impossible to be recovered even with our normalization technique. Only by aligning the interferometer in such a way that the ion fringes are formed outside the bright areas could they be detected.

The first ion fringe patterns presented here are rather noisy. In order to develop this ion interferometer into a reliable research tool, the stability of the ion source and its brightness has to be improved substantially. We hope to reach this goal by going from emitter temperatures of 77 K down to about 10 K and by using slightly higher beam voltage (∼15 kV).

7. Second order coherence experiments with electron waves

7.1. Measurement of second order coherence of electron waves: observation of Hanbury Brown–Twiss correlations for free electrons.

Hanbury Brown and Twiss (HB–T) have shown that for photons coherence manifests itself, in addition to the existence of interference fringes (first order coherence) in correlations of signal intensities in two coherently illuminated independent detectors (second order coherence). They herewith measured the angular sizes of chaotic astronomical radio sources and stars [339–344] and laid, as early as 1954, the foundation of an entire new field of physics: the discipline of quantum optics. Already in 1960 in their seminal papers Goldhaber *et al* [345, 346] and Goldberger *et al* [347] realized the significance of the HB–T effect for two particle correlations in nuclear and high energy particle physics. As in the present experiment with electrons, in high energy physics, the HB–T effect probes the many-body spatial wave function of the final state of indistinguishable particles (see, e.g. [348] and citations therein). It is one of the few processes in elementary particle detection that depends on the wave mechanics of the produced particles and gives—in the words of Baym—a deep insight into how the detectors 'do quantum mechanics' on the incoming particle waves, i.e. how the atoms of the detectors process to the amplitudes and phases of the waves into electronic signals [349, 350]. The bosonic HB–T effect has been studied in atomic beams in 1995 [351] and only recently the fermionic and bosonic HB–T effect has been experimentally realized in the same apparatus using two different isotopes of helium: ^{3}He (a fermion) and ^{4}He (a boson) [352]. Since ordinary attractive or repulsive interactions between the atoms are negligible, the bunching and antibunching behavior that the authors observed can be attributed to the different quantum statistics of each atom species.

Antibunching of free neutral fermionic ^{40}K atoms in a degenerate Fermi gas released from an optical lattice by suddenly switching off the optical potentials has been observed recently: when a particle is released with a crystal momentum of $\hbar q$ (q is the crystal wave vector) from the lattice potential it can be detected at equally spaced detector positions ($\Delta l = 2\hbar K t/m$ where m is the atomic mass). Owing to the single occupancy of each Bloch state dictated by the Pauli principle the output of two detectors will be anticorrelated [353].

Let us go back in history to 1956 when Purcell defended in his beautiful paper [354] the results of HB–T, which were controversially disputed by a large number of physicists at that time. He showed that the HB–T effect can be understood as a consequence of quantum interference between two indistinguishable photons (interference between two different particles) obeying Bose–Einstein statistics and resulting in an increased noise in a beam of coherent photons compared with the classical Boltzmann particles. He likewise showed that for fermions the antisymmetric two particle wave function excludes—in contrast to the symmetric wave function of bosons—overlapping wave trains and consequently should lead to anticorrelations in the arrival times of coherent

fermions which manifests itself in a—compared with classical particles—reduced, respectively, a vanishing shot noise in a fully degenerate fermionic beam of particles. This has been proven experimentally in 1999 for the limiting case of a fully degenerate flow of fermions in semiconductor devices, where such highly degenerate beams of electrons are conveniently available [355, 356]. In the early days after HB–T's invention only thermionic electron emitters with a degeneracy hopelessly small to prove antibunching were available. With the advent of high-brightness field electron emitters with degeneracies on the order of 10^{-4}, very fast detectors and coincidence electronics an experiment with free fermions has become feasible [328, 329, 357, 358, 365, 366] and is presented here [361].

Purcell's interpretation of the HB–T effect contains for the first time the perception that in the HB–T effect two individual particles interfere with one another when they arrive simultaneously in the coherence volume in front of the two detectors. Bunching and antibunching means that we observe interferences resolved in time which are stationary only for very short time interval of about a coherence time. This finding was revolutionary at that time if one takes into account the statement of PAM Dirac: 'Each photon interferes only with itself. Interference between two different photons never occurs'. On the other hand, already in 1909, Albert Einstein deduced with Planck's radiation formula, that the fluctuations of the energy of radiation in a volume is made up of two parts: shot noise and wave noise, caused by the dual nature of light, particle and wave [359]. Einstein writes later: 'One can interpret part of the fluctuations in an analogous way by attributing to a gas some kind of radiation in a suitable way and by calculation the interference fluctuations. I go into further details because I believe this is more than an analogy. Mr L de Broglie has shown, in a very remarkable thesis, how one can attribute a wave field to a material particle'.

It is well known that within the coherence time the phases of electromagnetic waves of a wave packet are correlated and described mathematically by the first-order correlation function $g^{(1)}(\tau)$. Therefore, the squares of the amplitudes, the intensities given in equation (7.1) are correlated as well and characterized by the second order correlation function $g^{(2)}(\tau)$ (look up, e.g. in Wikipedia[5] the key-word 'degree of coherence' or the paper of Tyc on electronic-field correlation functions [368]). The existence of these intensity correlations are an additional signature of coherence of the wave field. Simply by recording the arrival times of photons with two independent detectors within the coherently illuminated area, these second order correlations which are given by equation (7.1) can be proven:

$$g^{(2)}(\tau) := \frac{\langle I(t)I(t+\tau)\rangle}{\langle I(t)\rangle^2} = \frac{\langle U^*(t)U^*(t+\tau)U(t+\tau)U(t)\rangle}{\langle U^*(t)U(t)\rangle^2}$$
$$= 1 \pm \mid g^{(1)}(\tau) \mid^2 . \qquad (7.1)$$

While the relative phases of the components making up the wave packet are hidden in the second order correlation function, an up to now not available third, extraordinary important parameter of a wave field can be extracted by measuring the second order coherence correlations: the statistics of the wave field and in turn the corresponding symmetry of the wave function. At two detectors positioned within the coherence volume we either observe simultaneously arriving quantum particles or we never observe coincidences in their arrival times. For bosonic wave fields with their symmetric wave function coincident arrivals are allowed (+ sign in equation (7.1)) and by a factor of 2 more probable than for classical particles obeying the Poisson statistics, while for fermionic ones coincident arrivals are forbidden (− sign in equation (7.1)). So, the observation of second order correlations gives us information about the coherence of the wave fields *and the statistics of the involved quantum particles*. There are only two choices, either that a single or two (or more) quantum particles are within one coherence volume. For the case of a single (fermionic) one, the particles will be more homogeneously distributed in space and time, since the distances of these particles in space must exceed a coherence length (corresponding to a certain coherence time) and the diameter of the coherently illuminated area. That is, in principle, the illumination of an area with fermions (e.g. in an electron microscope) is more homogeneous than the same area illuminated with bosons (in a light microscope) [362]. Additionally, in a beam of fermions of certain dimensions an upper maximum of the total current flow exists which corresponds, e.g. to the theoretically existing maximum brightness of electron emitters [326]. In a beam of bosons (photons) such a limit does not exist.

The Michelson stellar interferometer uses first-order coherence (interference fringes) as a tool to measure the coherently illuminated diameter by a star on the surface of the earth. Unavoidable phase fluctuations caused by fluctuations of the index of refraction in the atmosphere and mechanical instabilities of this phase sensitive interferometer limits its applications to distances of the accepting mirrors of about 5 m, i.e. to the measurement diameters of relatively large and not too far stars. The advantage of the use of second order coherence to measure the area, which is coherently illuminated by a star, is that the correlations i.e. the fluctuations of the intensity of the arriving photons, are not disturbed by phase fluctuations in the beams. It extends the possibility of measuring diameters of stars which are by orders of magnitude smaller. The newest intensity interferometer SUSI (Sydney University Star Instrument) which went into operation in 1991 in Culgoora NSW Australia allows distances of the mirrors up to 640 m which corresponds to 0.0005 arcsec. It is located next door to the famous HB–T Narrabi intensity interferometer where mirror distances up to 200 m were possible.

7.2. An experiment on 'antibunching' of free electrons

The coincidence method chosen in the present 'antibunching' experiment is an alternative to HB–T's correlation procedure for gathering information about correlations in a stream of particles: two detectors are coherently illuminated by an electron field emitter. According to the Pauli principle no two electrons having a certain spin direction are allowed to be in the same quantum state, that is they cannot arrive at both detectors

[5] http://en.wikipedia.org/wiki/Degree_of_coherence

simultaneously[6]. In other words, if our detectors had a time resolution corresponding to the coherence time T_c which is on the order of 10^{-14} s, no coincidences would be observed. The time resolution of our fast coincidence counter of $T_r = 26$ ps was about three orders of magnitude less. For incoherent illumination of the detectors the electrons behave like classical particles. Owing to the insufficient time resolution a certain random coincidence rate is observed. When we change the illumination from incoherent to coherent we expect a reduction in the random coincidences (by a factor T_c/T_r of about 10^{-3} in the present experiment) because no second electron is allowed to arrive within 10^{-14} s after the arrival of the first electron. This reduction is our signature of antibunching.

7.2.1. Experimental set-up. Our experimental set-up corresponds to HB–T's stellar interferometer: the tiny effective virtual source of an electron field emitter illuminates, by means of magnifying quadrupoles two small collectors (figure 31, rhs). With increasing angular magnification the effective lateral distance of the collectors decreases and their illumination changes from incoherent to totally coherent. In turn, a continuous increase in anticorrelations of arrival times of the electrons at the collectors is expected.

The collectors (figure 31), 4 mm in diameter with an impedance of 50 Ω inserted between the exit of the two cascaded microchannel plates and the fluorescent screen, collect the electron avalanches initiated by single electrons. Into the actual electron optical set-up[7] an electron biprism (inset on the lhs, of figure 31) is integrated. It allows one to examine the state of coherence of illumination of the collectors[8] by observing the overlap of the fringes with the shadows cast by the collectors on the fluorescent screen. By this means the magnification factors which are necessary for coherent, partially coherent and incoherent illumination of the collectors are determined. The antibunching experiments are performed without biprism in the beam path at these predetermined magnifications.

Features of our cold [1 0 0]-oriented tungsten field emitter are extraction voltage 900 V, total current 1.5 μA, energy width ΔE_{FWHM} of 0.3 eV which corresponds to a standard deviation ΔE of 0.13 eV (calculated under the assumption of a Gaussian energy distribution), virtual source diameter ∼36 nm, brightness 4.4×10^7 A cm^{-2} sr^{-1}, coherence time $T_c = 3.25 \times 10^{-14}$ s, coherent particle current 4.7×10^9 s^{-1}, degeneracy 1.6×10^{-4}.

In spite of a vacuum of 10^{-10} mbar and a constant emission current during the data accumulation times T_M (see table 4), the counting rates of the detectors sometimes increased by more than a factor of 2 or fell below 0.5 of the desired value. In these cases a reduction, respectively an increase in coherence of illumination of the collectors took place. Therefore, time spectra with counting rates outside these limits were discarded. $T_{M_{eff}}$ is the data accumulation time resulting after subtraction of times of unstable emission.

[6] The fluctuations in orthogonal polarizations respectively spin directions are independent. Therefore, when the experiment is performed with unpolarized light/electron beams, enhancement respectively suppression of the extra fluctuations is reduced by a factor 1/2 compared with polarized beams.

[7] Its construction principles may be found, e.g. in [67].

[8] At least in the direction perpendicular to the fringes.

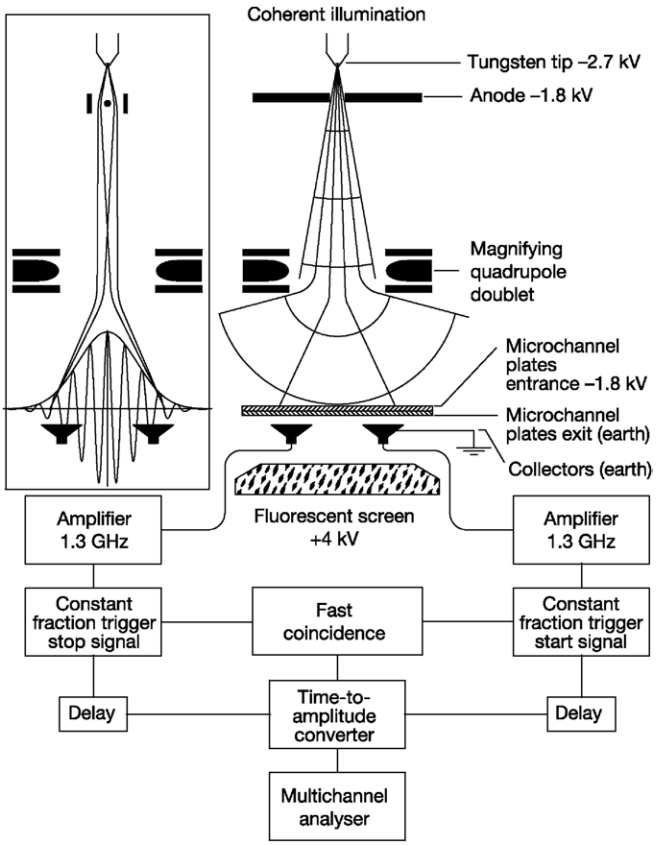

Figure 31. Electron optical set-up (top) and fast coincidence electronics (bottom) to measure electron anticorrelations. The quadrupoles produce an elliptically shaped beam of coherent electrons (schematically shown in the pictograms of figure 32). For geometrical reasons, fewer coherent electrons miss the collectors than for isotropic magnification. This greatly reduces the measuring time T_M. The parts of the spherical cones emerging from the cathode represent single coherence volumes. Between the electron source and the quadrupole a biprism (inset) is inserted temporarily to check the coherence of illumination of the collectors. The very short electron avalanches (rise time and width of about 0.5 ns) leaving the channel plates are transferred coaxially from the collectors via microwave amplifiers (bandwidth 1.3 GHz) to modified constant fraction trigger modules that extract timing signals with low variance of transit time resulting in a very good time resolution. A fast coincidence circuit preselects events within a time window of ±3 ns and opens the gate of the time-to-amplitude converter. The time spectra with a resolution of 26 ps are accumulated in a multichannel analyzer. Capacitive crosstalk between the collectors was well below 1% and does not cause spurious coincidences.

Table 4. Summary of results. S, S_{rel} are the absolute and relative coincidence reduction, respectively, S/N the signal-to-noise ratio, T_M the total measuring time and $T_{M_{eff}}$ the effective measuring time after subtraction of times of instable emission of the field emitter.

	Illumination		
	Part. Coh.	Coh.	Part. Coh.
$S = \Delta N$	8.292	16.942	4.567
$S_{rel}(10^{-3})$	0.61	1.26	0.34
S/N	2.2	3.0	1.4
T_M (min)	1402	1690	4531
$T_{M_{eff}}$ (min)	1402	1642	4450

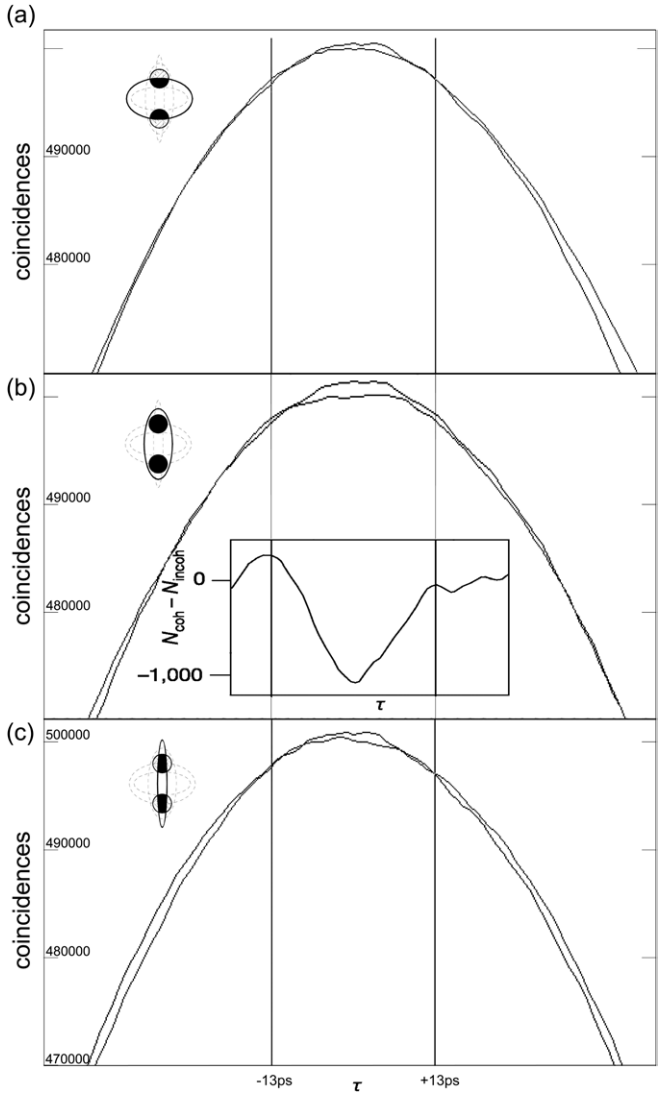

Figure 32. Antibunching as a function of coherence of illumination of the collectors. The coincidences per channel (channel width 0.99 ps) for incoherent illumination (upper curves in (*a*), (*b*) and (*c*)) are compared with that for partially coherent (*a*), coherent (*b*) and again partially coherent (*c*) illumination. In the inset to (*b*) the difference, fully coherent illumination $N_{\text{coh.}} - N_{\text{incoh.}}$, is given. In the pictograms the ellipses represent the coherently illuminated areas, the circles the collector areas. The coherently illuminated parts of the collectors are marked in black.

7.3. Results

In order to prove antibunching a total of four spectra were accumulated for about 30 h each (figure 32). The first for incoherent illumination of the detectors, the following for partially, totally and the last again for partially coherent illumination.

The evaluation procedure of the experimental time spectra consisted of smoothing and normalizing the spectra followed by visually superimposing the incoherent with the coherent and partially coherent spectra, respectively. The results [360, 361] are summarized in figure 32 and table 4. The antibunching signal S, that is the missing coincidences ΔN in the coherent and partially coherent spectra versus the incoherent spectrum becomes visible as a flattening of the peak in figure 32 within the time resolution window of ±13 ps. The measured relative reduction in coincidences for coherent illumination amounts to $S_{\text{rel}} = 1.26 \times 10^{-3}$ with a signal-to-noise ratio $S/N = 3$ and agrees well with the theoretically expected value from the characteristic features of our cold tungsten field emitter. As expected, the reduction in coincidence rate and the signal-to-noise ratio are smaller for partially coherent illumination (figures 32(*a*) and (*c*))[9].

7.3.1. Conclusion. Antibunching, i.e. interference between a system consisting of two particles, respectively second order coherence, has been observed for *massive free fermions*. This experimental technique opens a gateway to new fundamental tests of quantum mechanics and quantum statistics; for example, observation of quantum statistics on interference phenomena and experimental tests of interaction of fields and potentials with charged two-fermion systems [364, 365, 367].

Acknowledgments

I wish to thank all my students and co-workers for helpful discussions, namely in place of all other members of the group: Gerhard Wohland, Marc Nicklaus, Andreas Schäfer, Harald Kiesel, Uwe Maier, Peter Sonnentag, Henrike Prochel, Hilmar Wittel and Reimar Beierlein. Thanks to Professor Lenc of the University of Brno and Professor A Oed from Institute Laue-Langevin in Grenoble for theoretical and experimental advice, respectively. We have benefited from the ideas and enthusiasm of the guest scientists in my team, Tomas Tyc from the University in Brno, the Humbold awardee Richard Neutze and Professor G Stedman, both from Christchurch University in New Zealand and Professor Marc Silverman from Trinity College, Hartford, USA. We are indebted to the Deutsche Forschungsgemeinschaft for continuous, generous financial support of our projects.

References

[1] Elsasser W 1925 *Naturwissenschaften* **13** 711
[2] Davisson C and Germer L H 1927 *Nature* **119** 558–9
[3] de Broglie L 1924 *Phil. Mag.* **47** 466
[4] Estermann I and Stern O 1930 *Z. Phys.* **61** 95–125
[5] Boersch H 1940 *Phys. Z.* **44** 32–8
[6] Boersch H 1943 *Phys. Z.* **44** 202–11
[7] Gabor D 1948 *Nature* **197** 777–8
[8] Gabor D 1949 *Proc. R. Soc.* A **197** 454–87
[9] Gabor D 1951 *Proc. R. Soc.* B **64** 449–69
[10] Haine M E and Dyson J 1950 *Nature* **166** 315
[11] Haine M E and Mulvey T 1951 *Proc. NBS Semicentennial Symp. on Electron Physics (5–7 November 1951) NBS Circular 527, issued March 17th 1954* (Gaithersburg, MD: National Bureau of Standards) vol 527 pp 247–50

[9] In the original paper on this experiment [361] the time spectrum incoherent versus fully coherent illumination, corresponding to figure 32(*b*) in this paper, was erroneously presented with a 25% larger magnification in the direction of the time axis compared with sub-figures (*a*) and (*c*) in [361]. In this paper the value of magnification of all three plots is the same as it is in the PhD thesis of Kiesel [360].

[12] Haine M E and Mulvey T 1950 *Congress on Electron Microscopy Paris 1950* Edition de la Revue d'Optique, Paris (1952) p 73
[13] Haine M E and Mulvey T 1954 *J. Sci. Instrum.* **31** 326
[14] Haine M E and Mulvey T 1954 *Proc. Int. Conf. on Electron Microscopy (London, UK, 1954)* (London: Royal Microscopical Society) p 698 and plates 188–9
[15] Cosslett V E 1951 *Proc. NBS Semicentennial Symp. on Electron Physics (5–7 November 1951), NBS Circular 527, issued March 17th 1954* (Gaithersburg, MD: National Bureau of Standards) vol 527 pp 291–303
[16] Marton L 1952 *Phys. Rev.* **85** 1057–78
[17] Marton L, Simpson J A and Suddeth J A 1954 *Phys. Rev.* **90** 490–1
[18] Simpson J A 1954 *Rev. Sci. Instrum.* **25** 1105–9
[19] Marton L, Simpson J A and Suddeth J A 1954 *Rev. Sci. Instrum.* **25** 1099–104
[20] Simpson J A 1956 *Rev. Mod. Phys.* **28** 25–260
[21] Möllenstedt G and Düker H 1955 *Naturwissenshaften* **42** 41
[22] Möllenstedt G and Düker H 1956 *Z. Phys.* **145** 377–97
[23] Düker H 1956 *Z. Naturf.* a **10** 256–7
[24] Faget J and Fert C 1957 *Cah. Phys.* **83** 286–96
[25] Faget J 1961 *Rev. D'Opt.* **40** 347–81
[26] Borrmann G 1941 *Z. Phys.* **42** 157–62
[27] Bonse U and Hart M 1965 *Appl. Phys. Lett.* **6** 155–7
[28] Klein A G and Werner S A 1983 *Rep. Prog. Phys.* **46** 259–335
[29] Rauch H and Werner S A 2000 *Neutron Interferometry: Lessons in Experimental Quantum Mechanics* (*Oxford Series on Neutron Scattering in Condensed Matter* 12) (New York: Oxford University Press)
[30] Greenberger D M and Overhauser A W 1979 *Rev. Mod. Phys.* **51** 43–78
[31] Rauch H 2004 *Phys. J.* **3** 39–45
[32] Greenberger D M 1983 *Rev. Mod. Phys.* **55** 875–905
[33] Rauch H, Treimer W and Bonse U 1974 *Phys. Lett.* A **47** 369–71
[34] Rauch H 1986 *Contemp. Phys.* **27** 345–60
[35] Jönsson C 1961 *Z. Phys.* **161** 454–74
[36] Jönsson C 1974 *Am. J. Phys.* **42** 4–11
[37] Physics World 2002 *Physicsworld* September 2002 p 15
[38] Möllenstedt G and Keller M 1957 *Z. Phys.* **148** 34–7
[39] Buhl R 1959 *Z. Phys.* **155** 395–412
[40] Ehrenberg W and Siday R E 1949 *Proc. Phys. Soc.* **62** 8–21
[41] Aharonov Y and Bohm D 1959 *Phys. Rev* **115** 485–91
[42] Franz W 1939 *Phys. Berichte* **21** 686
Franz W 1939 *Verh. Deutsch. Phys. Ges.* **20** 65–6
[43] Chambers R G 1960 *Phys. Rev. Lett.* **5** 3–5
[44] Möllenstedt G and Bayh W 1962 *Phys. Bl.* **18** 299–305
[45] Boersch H, Hamisch H and Grohmann K 1962 *Z. Phys.* **169** 263–72
[46] Tonomura A, Osakabe N, Matsuda T, Kawasaki T, Endo J, Yano S and Yamada H 1986 *Phys. Rev. Lett.* **56** 792–5
[47] Drahos V and Delong A 1964 *Opt. Acta* **11** 173–81
[48] Komrska J, Drahos V and Delong A 1964 *Opt. Acta* **11** 145–57
[49] Komrska J, Drahos V and Delong A *Opt. Acta* **14** 147–67
[50] Komrska J and Vlachova B 1973 *Opt. Acta* **20** 207–15
[51] Möllenstedt G and Wahl H 1968 *Naturwissenschaften* **55** 340–1
[52] Tonomura A 1969 *J. Electron Microsc.* **18** 77–8
[53] Tomita H, Matsuda T and Komoda T 1970 *Japan. J. Appl. Phys.* **9** 719
[54] Munch J 1975 *Optik* **43** 79–99
[55] Crewe A V, Eggenberger D N, Wall J and Welter L M 1968 *Rev. Sci. Instrum.* **39** 576–83
[56] Crewe A V, Wall J and Welter L M 1968 *J. Appl. Phys.* **39** 5861–8
[57] Crewe A V, Wall J and Langmore J 1970 *Science* **168** 1338–40
[58] Crewe A V and Wall J 1970 *J. Mol. Biol.* **48** 375–93
[59] Crewe A V 1980 *Rep. Prog. Phys.* **43** 621–39
[60] Brünger W 1968 *Naturwissenschaften* **55** 295–6
[61] Brünger W 1972 *Z. Phys.* **250** 263–72
[62] Leavitt J A and Bills F A 1969 *Am. J. Phys.* **37** 905–12
[63] Herrmann K H, Krahl D, Kübler A and Rindfleisch V 1969 *Siemens Rev.* **36** 6–10
[64] Merli P G, Missiroli G F and Pozzi G 1976 *Am. J. Phys.* **44** 306–7
[65] Wohland G 1977 *Diploma Thesis* University of Tübingen (unpublished, in German)
[66] Hasselbach F 1979 *19. Tagung der Deutschen Gesellschaft für Elektronenmikroskopie, Tübingen* Abstract 7L1, p 90
[67] Hasselbach F 1988 *Z. Phys. B—Condens. Matter* **71** 443–9
[68] Tonomura A, Endo J, Matsuda T and Kawasaki T 1989 *Am. J. Phys.* **57** 117–20
[69] Missiroli G F, Pozzi G and Valdre 1981 *J. Phys. E: Sci. Instrum.* **14** 649–71
[70] Tonomura A 1987 *Rev. Mod. Phys.* **59** 639–69
[71] Tonomura A 2003 *J. Electron Microsc.* **52** 11–9
[72] Nicklaus M 1989 *Dissertation* University of Tübingen (unpublished, in German)
[73] Aschmoneit E K 1985 *Elektronik* **80** 79–81
[74] Herrmann K H 1984 *Brochure on the New Type of Electron Interferometer* ed University of Tübingen for the Hannovermesse
[75] Hasselbach F and Nicklaus M 1993 *Phys. Rev.* A **48** 143–51
[76] Wu T T and Yang C N 1975 *Phys. Rev.* D **12** 3845–56
[77] Möllenstedt G and Bayh W 1962 *Naturwissenschaften* **49** 81–2
[78] Bayh W 1962 *Z. Phys.* **169** 492–510
[79] Schaal G, Jönsson C and Krimmel E F 1966 *Optik* **24** 529–38
[80] Schmid H 1985 *Dissertation* Universität Tübingen (unpublished, in German)
[81] Yamamato K, Tanji T and Hibino M 2000 *Ultramicroscopy* **85** 35–49
[82] Yamamoto K, Kawajiri I, Tanji T and Hibino M 2000 *J. Electron Microsc.* **49** 31–9
[83] Yamamoto K, Hirayama T, Tanji T and Hibino M 2003 *Surf. Interface Anal.* **35** 60–5
[84] Fujita T, Yamamoto K, McCartney M R and Smith D 2006 *Ultramicroscopy* **106** 486–91
[85] Akashi T, Harada K, Matsuda T, Kasai H, Furutsu T, Moriya N, Yoshida T, Kawasaki T, Kitazawa K and Koinuma H 2002 *Appl. Phys. Lett.* **81** 1922–4
[86] Harada K, Akashi T, Togawa Y, Matsuda T and Tonomura A 2005 *J. Electron Microsc.* **54** 19–27
[87] Harada K, Tonomura A, Togawa Y, Akashi T and Matsuda T 2004 *Appl. Phys. Lett.* **84** 3229–31
[88] Harada K, Tonomura A, Matsuda T, Akashi T and Togawa Y 2004 *J. Appl. Phys.* **96** 6097–102
[89] Speidel R and Kurz D 1977 *Optik* **49** 173–85
[90] Harada K, Matsuda T, Tonomura A, Akashi T and Togawa Y 2006 *J. Appl. Phys.* **99** 113502
[91] Kawasaki T, Missiroli G F, Pozzi G and Tonomura A 1996 *Eur. J. Phys.* **18** 7–14
[92] Möllenstedt G and Wohland G 1980 Electron microscopy *7th European Congress on Electron Microscopy Foundation (Leiden, Netherlands, 1980)* ed P Bredoro and G Boom vol 1 pp 28–9
[93] Werner F G and Brill D R 1960 *Phys. Rev. Lett.* **4** 344–7
[94] Peskin M and Tonomura A 1989 *The Aharonov–Bohm Effect* (*Lecture Notes on Physics* vol 340) (Berlin: Springer)
[95] Wohland G 1981 *Dissertation* Universität Tübingen (unpublished, in German)
[96] Rang O 1964 *Optik* **21** 59–65
[97] Rang O 1977 *Ultramicroscopy* **2** 149–51
[98] Hasselbach F 1992 Recent contributions of electron interferometry to wave–particle duality *Wave–Particle Duality* ed Franco Sellerie (New York: Plenum) pp 109–25
[99] Nicklaus M and Hasselbach F 1993 *Phys. Rev.* A **48** 152–60

[100] Hasselbach F 1995 Experiments with coherent electron wave packets *Fundamental Problems in Quantum Physics* ed M Ferrero and A van der Merve (Dordrecht: Kluwer) pp 123–39
[101] Hawkes P W 1978 *Adv. Opt. Electron Microsc.* **7** 101–84
[102] Hasselbach F and Schäfer A 1990 Interferometric (Fourier-spectroscopic) measurement of electron energy distributions *Proc. 12th. Int. Congress for Electron Microscopy (Seattle 1990)* vol 2 ed L D Peachey and D B Williams (San Francisco, CA: San Francisco Press, Inc.) pp 10–11
[103] Klein A G, Opat G I and Hamilton W A 1983 *Phys. Rev. Lett.* **50** 563–65
[104] Comsa G 1987 *Phys. Rev.* **58** 2274
[105] Daberkow I, Gauch H and Hasselbach F 1983 Measurement of the longitudinal coherence of electrons from a fieldemission source *Joint Meeting on Electron Microscopy (Antwerpen, Belgium)* Program and Abstract Book p 100
[106] Schäfer A 1989 Fourierspektroskopie mit Elektronenwellen *Diploma Thesis* Institut für Angewandte Physik der Universität Tübingen (in German)
[107] Wachendorfer H 1993 Fourierspektroskopie mit Elektronenwellen *Diploma Thesis* Institut für Angewandte Physik der Universität Tübingen (in German)
[108] Bauer M and Hasselbach F 1995 *Optik* (Suppl. 6) **100** 7
[109] Bauer M, Hasselbach H, Kiesel H, Kraus H, Maier U and Schäfer A 1996 Quantum interferometry *Proc. Adriatico Workshop (Trieste, Italy, March 1996)* ed F de Martini *et al* (Weinheim: VCH) pp 349–60
[110] Michelson A A 1891 *Phil. Mag.* **31** 256–9
[111] Michelson A A 1891 *Phil. Mag.* **31** 338–46
[112] Michelson A A 1892 *Phil. Mag.* **34** 280–92
[113] Rubens H and Wood R W 1911 *Phil. Mag.* **34** 280–99
[114] Hasselbach F and Schäfer A 1990 *German Patent* DE4024624 A1
[115] Sonnentag P, Kiesel H and Hasselbach F 2000 *Micron* **31** 451–6
[116] Hasselbach F, Schäfer A and Wachendorfer H 1995 *Nucl. Instrum. Methods Phys. Res.* A **363** 323–38
[117] Boersch H, Hamisch H, Wohlleben D and Grohmann K 1960 *Z. Phys.* **159** 397–404
[118] Merzbacher E 1962 *Am. J. Phys* **30** 237–47
[119] Erlichson H 1970 *Am. J. Phys.* **38** 162–73
[120] Olariu S and Popescu I I 1985 *Rev. Mod. Phys.* **57** 339–436
[121] Horvathy P A 1985 *Phys. Rev.* A **31** 1151–3
[122] Silverman M P 1995 *More Than One Mystery, Explorations in Quantum Interference* (Berlin: Springer)
[123] Tonomura A 1998 *The Quantum World Unveiled by Electron Waves* (Singapore: World Scientific)
[124] Aharonov Y and Carmi G 1973 *Found. Phys.* **3** 493–8
[125] Aharonov Y and Carmi G 1974 *Found. Phys.* **3** 75–81
[126] Nicklaus M and Hasselbach F 1995 *Ann. New York Acad. Sci.* **755** 877–9
[127] Rizzi G and Ruggiero L 2003 *Gen. Rel. Grav.* **35** 1745–60
[128] Sakurai J J 1980 *Phys. Rev.* D **21** 2993–4
[129] Post E J 1967 *Rev. Mod. Phys.* **39** 475–93
[130] Zimmermann J E and Mercereau J E 1965 *Phys. Rev. Lett.* **14** 887–8
[131] Becker R, Sauter F and Haller C 1933 *Z. Phys.* **85** 772–87
[132] London F 1960 *Superfluids* (New York: Dover) vol 1 pp 78–83
[133] Hildebrandt A F 1964 *Phys. Rev. Lett.* **12** 190–1
[134] Brickman N F 1969 *Phys. Rev.* **184** 460–5
[135] Rystepanick R G 1976 *Am. J. Phys.* **44** 647–8
[136] Michelson A A and Gale H G 1925 *Astrophys. J.* **61** 137–45
[137] Heer C V 1961 *Bull. Am. Phys. Soc.* **6** 58
[138] Heer C V 1959 *Disclosure of Invention, Docket 208* Space Technology Laboratories Inc. (8th October 1959)
[139] Page L A 1975 *Phys. Rev. Lett.* **35** 543
[140] Kobe D H 1979 *Ann. Phys.* **123** 381–410
[141] Colella R, Overhauser A W and Werner S A 1975 *Phys. Rev. Lett.* **34** 1472–4
[142] Anandan J 1977 *Phys. Rev.* D **15** 1448–57
[143] Rauch H 1985 *Phys. Bl.* **41** 190–5
[144] Atwood D K, Horne M A, Shull C G and Arthur J 1984 *Phys. Rev. Lett.* **52** 1673–6
[145] Hasselbach F 1986 *German Patent* DE 3504278 C2, Anmeldetag 8.2.1985, Offenlegungstag 14.8.1986, Patenterteilung 10.12. 1987
[146] Clauser J F 1988 *Physica* B **151** 262–72
[147] Anderson R, Bilger H R and Stedmann G E 1994 *Am. J. Phys.* **62** 975–85
[148] Hasselbach F and Nicklaus M 1988 *Physica* B **151** 230–4
[149] Semon M D 1982 *Found. Phys.* **12** 49–57
[150] Cerdonio M and Vitale S 1984 *Phys. Rev.* B **29** 481–3
[151] Hess G B 1992 *Nature* **359** 192–3
[152] Varoquaux E *et al* 1992 *Physica* B **178** 309–17
[153] Packard R E and Vitale S 1992 *Phys. Rev.* B **46** 3540–9
[154] Avenel O, Hakonen P and Varoquaux E 1997 *Phys. Rev. Lett.* **78** 3602–5
[155] Avenel O and Varoquaux E 1985 *Phys. Rev. Lett.* **55** 2704
[156] Avenel O and Varoquaux E 1987 *Japan. J. Appl.* Phys. (Suppl. 26-3) **26** 1798
[157] Avenel O, Hakonen P and Varoquaux E 1998 *J. Low Temp. Phys.* **110** 709–18
[158] Avenel O, Mukharsky Y and Varoquaux E 2004 *J. Low Temp. Phys.* **135** 745–73
[159] Avenel O and Varoquaux E 1996 *Czech. J. Phys.* (Suppl. S6) **46** 3319
[160] Schreiber U, Schneider M, Stedman G E, Friesch A, Hasselbach F, Ruder H and Schlüter W 1999 *Journées 1999, Systèmes de Référence Spatio-Temporels& IX Lohrman-Kolloquium (Dresden, Germany, 13–15 September 1999)* ed M Soffel and N Capitaine pp 221–32
[161] Gupta S, Murch K W, Moore K L, Purdy T P and Stamper-Kurn D M 2005 *Phys. Rev. Lett* **95** 143201
[162] Robins N P, Figl C R, Jeppesen M, Graham R, Close D and Close J 2008 *Nature Phys.* **4** 731–6
[163] Levy S, Lahoud E, Shomroni I and Steinhauer J 2007 *Nature* **449** 579–83
[164] Lodge O 1893 *Phil. Trans. R. Soc.* A **184** 727
[165] Lodge O 1897 *Phil. Trans. R. Soc.* A **189** 149
[166] Lodge O 1931 *Past Years: An Autobiography* (London: Camelot)
[167] Harress F 1912 *PhD Thesis* Jena
[168] Sagnac M G 1913 *Compt. Rend.* **157** 708–10
[169] Sagnac M G 1913 *Compt. Rend.* **157** 1410–3
[170] Sagnac M G 1914 *J. Phys.* (Paris) **4** 177
[171] Michelson A A 1904 *Phil. Mag.* **8** 716–9
[172] Einstein A 1914 *Astron. Nachr.* **199** 7–10
[173] Harzer P 1914 *Astron. Nachr.* **198** 377–92
[174] Laue M 1920 *Ann. Phys.* **62** 448–63
[175] Malykin G B 1997 *Phys.—Usp.* **40** 317–21
[176] Malykin G B 2000 *Phys.—Usp.* **43** 1229–52
[177] Schwab K, Bruckner N and Packard R E 1997 *Nature* **386** 585
[178] Mukharsky Y, Avenel O and Varoquaux E 2000 *Physica* B **284–288** 287–8
[179] Stedman G E, Schreiber K U and Bilger H R 2003 *Class. Quantum Grav.* **20** 2527–40
[180] Anandan J 1984 *Gen. Rel. Grav.* **16** 33–41
[181] Stedman G E 1997 *Rep. Prog. Phys.* **60** 615–88
[182] Riehle F, Kisters Th, Witte A, Helmcke J and Bordé Ch J 1991 *Phys. Rev. Lett.* **67** 177–80
[183] Chow W W, Gea-Banacloche J, Pedrotti L M, Sanders V E, Schleich W and Scully M O 1985 *Rev. Mod. Phys.* **57** 61–104

[184] http://en.wikipedia.org/Wiki/Very_Long_Baseline_Interferometry/Scientific_Results
[185] Gustavson T L, Bouyer T and Kasevich M A 1997 *Phys. Rev. Lett.* **78** 2046–9
[186] Gustavson T L, Landragin A and Kasevich M A 2000 *Class. Quantum Grav.* **17** 2385–98
[187] Misner C W, Thorne K S and Wheeler J A 1973 *Gravitation* (San Francisco, CA: Freeman)
[188] Durfee D S, Shaham Y K and Kasevich M A 2006 *Phys. Rev. Lett.* **97** 240801
[189] Dubetsky B and Kasevich M A 2006 *Phys. Rev.* A **74** 023615
[190] Hasselbach F and Maier U 1996 *Quantum Coherence and Decoherence* ed K Fujikawa and Y Y Ono (Amsterdam: Elsevier) pp 69–72
[191] Hasselbach F and Maier U 1999 *Quantum Coherence and Decoherence—ISQM-Tokyo 98* ed Y Y Ono and K Fujikawa (Amsterdam: Elsevier) pp 299–302
[192] Rösch E 1964 *Diploma Thesis* Institut für Angewandte Physik der Universität Tübingen
[193] Maier U 1997 *PhD Thesis* Universtät Tübingen Institut für Angewandte Physik (unpublished, in German)
[194] Dowling J P 1998 *Phys. Rev.* A **57** 4736–46
[195] Thirring H 1918 *Phys. Z.* **19** 33–9
[196] Thirring H 1921 *Phys. Z.* **22** 29–30
[197] Lense J and Thirring H 1918 *Phys. Z.* **19** 156–63
[198] Mashoon B, Hehl F W and Theiss D S 1984 *Gen. Rel. Grav.* **16** 711–50
[199] Everitt CWF Gravity Probe B: countdown to launch *Clocks, Interferometers: Testing General Relativistiv Gravity in Space* ed C Lämmerzahl *et al* (Heidelberg: Springer)
[200] Dimopoulos S, Graham P W, Hogan J M and Kasevich M A 2007 *Phys. Rev. Lett.* **98** 111102
[201] Delgado A, Schleich W P and Süssmann G 2002 *New J. Phys.* **4** 37.1–37.8
[202] Overhauser A W and Colella R 1974 *Phys. Rev. Lett.* **33** 1237–9
[203] Werner S A, Staudemann J L and Collela R 1979 *Phys. Rev. Lett.* **42** 1103–6
[204] Bonse U and Wroblewski T 1983 *Phys. Rev. Lett.* **51** 1401–4
[205] Hasselbach F and Nicklaus M 1986 *Proc. Int. Symp. on Electron Optics (Beijing, China 1986) J. Electron Microsc.* **35** 691
[206] Haefele J C 1970 *Nature* **227** 270–1
[207] Haefele J C 1971 *Nature Phys. Sci.* **229** 238–9
[208] Haefele J C 1972 *Am. J. Phys.* **40** 81–5
[209] Haefele J C and Keating R E 1972 *Science* **177** 166–8
[210] Haefele J C and Keating R E 1972 *Science* **177** 168–70
[211] 1971 *Nature News and Views* vol 233 October 1971 p 519
[212] Chiao R Y 1990 *Proc. Int. Conf. on Fundamental Aspects of Quantum Theory to Celebrate 30 Years of the Aharonov–Bohm Effect* ed J S Anandan (Singapore: World Scientific) pp 107–121
[213] Dieks D 1990 *Found. Phys. Lett.* **3** 347–57
[214] Dieks D and Nienhuis G 1990 *Am. J. Phys.* **58** 650–5
[215] Neutze R and Hasselbach F 1998 *Phys. Rev.* A **58** 557–65
[216] Dürr S, Nonn T and Rempe G 1998 *Nature* **395** 33–7
[217] Glauber R J 1986 *Proc. Conf. New Techniques and Ideas in Quantum Measurement Theory Ann. New York Acad. Sci.* **480** 336–72 (here p 369)
[218] Herzog T J, Kwiat P G, Weinfurter H and Zeilinger A 1995 *Phys. Rev. Lett.* **75** 3034–7
[219] Dürr S, Nonn T and Rempe G 1998 *Phys. Rev. Lett.* **81** 5705–9
[220] Dopfer B, Weinfurter H and Zeilinger A 1998 *Verh. Deutsch. Phys. Ges.* **33** 191
[221] Englert B G 1996 *Phys. Rev. Lett.* **77** 2154–7
[222] Wootters W K and Zurek W H 1979 *Phys. Rev.* D **19** 473–84
[223] Zeilinger A 1986 *Physica* B **137** 235–44
[224] Zeh H D 1970 *Found. Phys.* **1** 69–76
[225] Zurek W H 1981 *Phys. Rev.* D **24** 1516–25
[226] Joos E *et al* 2003 *Decoherence and the Appearance of a Classical World in Quantum Theory* 2nd edn (Berlin: Springer)
[227] Zurek W H 2003 *Rev. Mod. Phys.* **75** 715–75
[228] Pfau T *et al* 1994 *Phys. Rev. Lett.* **73** 1223–6
[229] Hackermüller L *et al* 2004 *Nature* **427** 711
[230] Brune M *et al* 1996 *Phys. Rev. Lett.* **77** 4887–90
[231] Hornberger K, Uttenthaler S, Brezger B, Hackermüller L, Arndt M and Zeilinger A 2003 *Phys. Rev. Lett.* **90** 160401
[232] Schleich W P 2000 *Nature* **403** 256
[233] Myatt C J, Turchette Q A, Sackett C A, Kielpinski D, Itano W M, Monroe C and Wineland D J 2000 *Nature* **403** 269–73
[234] Sonnentag P and Hasselbach F 2005 *Brazil. J. Phys.* **35** 385–90
[235] Sonnentag P 2006 *PhD Thesis* Universität Tübingen
[236] Sonnentag P and Hasselbach F 2007 *Phys. Rev. Lett.* **98** 200402
[237] Anglin J R, Paz J P and Zurek W H 1997 *Phys. Rev.* A **55** 4041–53
[238] Hawkes P 1966 *Quadrupole Optics* (Berlin: Springer)
[239] Anglin J R and Zurek W H 1996 *Dark Matter in Cosmology—Quantum Measurements—Experimental Gravitation* ed R Ansari *et al* (Gif-sur-Yvette: Editions Frontières) pp 263–70
[240] Ford L H 1993 *Phys. Rev.* D **47** 5571–80
[241] Zurek W H 1986 *Frontiers of Nonequilibrium Statistical Physics* ed G T Moore and M Scully (New York: Plenum) pp 145–9
[242] Joos E 1996 *Decoherence and the Appearance of a Classical World in Quantum Theory* ed D Giulini *et al* (Berlin: Springer)
[243] Breuer H P and Petruccione F 2002 *The Theory of Open Quantum Systems* (Oxford: Oxford University Press) chapter 4.3
[244] Machnikowski P 2006 *Phys. Rev.* B **73** 155109
[245] Mandel L 1991 *Opt. Lett.* **16** 1882–83
[246] Sokolovskaia I L 1956 *Sov. Phys.—Tech. Phys.* **26** 1147–54
[247] Hasselbach F, Nicklaus M and Zeuner K 1986 *J. Phys.* (Colloque C7, Suppl. 11) **47** 453–8
[248] Janssen A P and Jones J P 1971 *J. Phys. D: Appl. Phys.* **4** 118–23
[249] Müller E W 1938 *Z. Phys.* **108** 668–80
[250] Veneklasen L H and Siegel B M 1972 *J. Appl. Phys.* **43** 1600
[251] Binh V T, Piquet A, Roux H, Uzan R and Drechsler J 1976 *Physica* E **9** 377
[252] Kim H S, Yu L U, Staufer U, Muray L P, Kern D P, Chang T P H 1993 *J. Vac. Sci. Technol.* B **11** 2327–31
[253] Kubby J A and Siegel B M 1986 *J. Vac. Sci. Technol.* B **4** 120–5
[254] Nagaoka K, Fujii H, Matsuda K, Komaki M, Murata Y, Oshima C and Sakurai T 2001 *Appl. Surf. Sci.* **182** 12–19
[255] Fu T Y, Cheng L C, Nien C H and Tsong T T 2001 *Phys. Rev.* B **64** 113401
[256] Martinez J C and Polatdemir E 2004 *Appl. Phys. Lett.* **84** 1320–2
[257] Kuo H S, Hwang T Y, Fu J Y, Chang C C and Tsong T T 2004 *Nano Lett.* **4** 2379
[258] Kuo H S, Hwang I S, Fu T Y, Lin Y C, Chang C C and Tsong T T 2006 *Japan. J. Appl. Phys.* **45** 8972–83
[259] Nagaoka K, Yamashita T, Uchiama S, Yamada M, Fijii H and Oshima C 1998 *Nature* **396** 557–9
[260] Gadzuk J W 1969 *Surf. Sci.* **15** 466–82
[261] Oshima C 1997 *Adv. Colloid Interface Sci.* **71–72** 353–69
[262] Ogawa H, Arai N, Nagaoka K, Uchiama S, Yamashita T, Itoh H and Oshima C 1996 *Surf. Sci.* **357–8** 371–5
[263] Cho B, Ichimura T, Shimizu R and Oshima C 2004 *Phys. Rev. Lett.* **92** 246103

[264] Oshima C, Rokuta E and Cho B 2005 *Chin. J. Phys.* **43** 145–53
[265] Cumings J, Zettl A and McCartney M R 2004 *Microsc. Microanal.* **10** 420–4
[266] Prigent M and Morin P 2000 *J. Microsc.* **199** 197–207
[267] Oshima C, Mastuda K, Kona T, Mogami Y, Komaki M, Murata Y, Yamashita T, Kuzumaki T and Horiike Y 2002 *Phys. Rev. Lett.* **88** 038301
[268] Summhammer J and Schmiedmayer J 1990 *Phys. Scr.* **42** 124
[269] Cho B, Ogawa T, Ichimura T, Ichinokawa T, Amakusa T and Oshima C 2004 *Rev. Sci. Instrum.* **75** 3091–6
[270] Cho B, Ishikawa T and Oshima C 2007 *Appl. Phys. Lett.* **91** 163102
[271] Komrska J 1971 *Adv. Electron. Electron Phys.* **30** 139
[272] Cho B, Itagaki T, Ishikawa T, Rokuta E and Oshima C 2007 *J. Vac. Sci. Technol.* B **25** 1420–3
[273] Rokuta E, Kuo H S, Itagaki T, Nomura K, Ishikawa T, Cho B L, Hwang I S, Tsong T T and Oshima C 2008 *Surf. Sci.* **602** 2508–12
[274] Birk H, de Jong M J M and Schönenberger C 1995 *Phys. Rev. Lett.* **75** 1610–13
[275] Escovitz H W, Fox T R and Levi-Setti R 1975 *Proc. Natl Acad. Sci. USA* **72** 1826–8
[276] Scipioni L, Stern L and Notte J 2007 *Microscopy Today* **15** 12–15
[277] Morgan J, Notte J, Hill R and Ward B 2006 *Microscopy Today* **14** 24–31
[278] Ward B W, Farkas L, Notte J A and Randall G P 2007 *US Patent No* US2007/0228287 A1 4 October 2007
[279] Ward B W, Farkas L, Notte J A and Randall G P 2007 *US Patent No* US0215802 A1, 20 September 2007
[280] Tamaki S, Inoue T, Kim H and Sugata E 1974 *8th Int. Congress on Electron Microscopy (Canberra, Australia 1974)* vol 1 p 114
[281] Fink H W 1986 *IBM J. Res. Dev.* **30** 460
[282] Fink H W 1988 *Phys. Scr.* **38** 260–3
[283] Binh V T, Purcell S T, Garcia N and Doglioni J 1992 *Phys. Rev. Lett.* **69** 2527
[284] Binh V T and Garcia N 1992 *Ultramicroscopy* **42–44** 80–90
[285] Yu M L, Lang N D, Hussey B W, Chang T P H and Mackie W A 1996 *Phys. Rev. Lett.* **77** 1636–9
[286] Gohda Y and Watanabe S 2001 *Phys. Rev. Lett.* **87** 177601
[287] Gohda Y, Nakamura Y, Watanabe K and Watanabe S 2000 *Phys. Rev. Lett* **85** 1750–53
[288] Gohda Y and Watanabe S 2003 *J. Vac. Sci. Technol.* B **21** 2461
[289] Nagaoka K, Fujii H, Matsuda K, Komaki M, Murata Y, Oshima C and Sakurai T 2001 *Appl. Surf. Sci.* **12** 182
[290] Song K J, Demmin R A, Dong C, Garfunkel E and Madey T E 1990 *Surf. Sci. Lett.* **L79** 227
[291] Song K J, Dong C Z and Madey T E 1991 *Langmuir* **7** 3019
[292] Chen S P 1992 *Surf. Sci. Lett.* **274** L619–25
[293] Williams E D and Bartelt N C 1991 *Science* **251** 393–400
[294] Che J G, Chan C T, Kuo C H and Leung T C 1997 *Phys. Rev. Lett.* **79** 4230–3
[295] Madey T E, Nien C-H, Pelhos K, Kolodziej J J, Abdelrehim I M and Tao H S 1999 *Surf. Sci.* **438** 191–206
[296] Jonge de N and Bonard J M 2004 *Phil. Trans. R. Soc. Lond.* A **362** 2239–66
[297] Fransen M J, Rooy van ThL and Kruit P 1999 *Appl. Surf. Sci.* **146** 312–27
[298] Müller E W 1956 *J. Appl. Phys.* **27** 474
[299] G R and Siegel M 1979 *J. Vac. Sci. Technol.* **16** 1875–8
[300] G R and Siegel M 1981 *J. Vac. Sci. Technol.* **19** 1176–81
[301] Hofmann H G 1989 *Diploma Thesis* Institut für Angewandte Physik der Universität Tübingen (in German)
[302] Cavaillé J Y and Drechsler M 1978 *Surf. Sci.* **75** 342–54
[303] Dranova Z I and Mikhailowskii I M 1972 *Sov. Phys.—Solid State* **12** 104
[304] Boersch H 1954 *Z. Phys.* **139** 115–46
[305] Speidel R and Gaukler K H 1968 *Z. Phys.* **208** 419–26
[306] Rose H and Spehr R 1980 *Optik* **57** 339–64
[307] Schwoebel P R and Hanson G R 1984 *J. Appl. Phys.* **56** 2101
[308] Schwoebel P R and Hanson G R 1985 *J. Vac. Sci. Technol.* B **3** 214–9
[309] Schwoebel P R and Hanson G R 1986 *J. Phys.* (Colloque C2, Suppl. 3) **47** 59–66
[310] Schwoebel P R and Hanson G R 1987 *J. Vac. Sci. Technol.* B **5** 195–6
[311] Jousten K, Böhringer K, Börret R and Kalbitzer S 1988 *Ultramicroscopy* **26** 301–12
[312] Börret R, Jousten K, Böhringer S and Kalbitzer S 1988 *J. Phys. D: Appl. Phys.* **21** 1835–7
[313] Böhringer K, Jousten K and Kalbitzer S 1988 *Nucl. Instrum. Phys. Res.* B **30** 289–92
[314] Börret R, Böhringer K and Kalbitzer S 1990 *J. Phys. D: Appl. Phys.* **23** 1271–7
[315] Maisch T, Wilbertz C, Miller T and Kalbitzer S 1993 *Nucl. Instrum. Methods Phys. Res.* B **80/81** 1288–91
[316] Miller T, Knoblauch A, Wilbertz C and Kalbitzer S 1995 *Appl. Phys.* A **61** 99–100
[317] Young R, Ward J and Scire F 1972 *Rev. Sci. Instrum.* **43** 999–1011
[318] Simmons J G 1963 *J. Appl. Phys.* **34** 1793
[319] Fink H W, Stocker W and Schmid H 1990 *Phys. Rev. Lett.* **65** 1204–6
[320] Fink H W, Schmid H, Kreuzer H and Wierzbiki A 1991 *Phys. Rev. Lett.* **67** 1543–46
[321] Spence J H C and Qian W 1992 *Phys. Rev.* B **45** 10271–9
[322] Qian W, Scheinfein M R and Spence J C H 1993 *J. Appl. Phys.* **73** 7041–4
[323] Scheinfein M R, Qian W and Spence J C H 1993 *J. Appl. Phys.* **73** 2057–68
[324] Qian W, Scheinfein M R and Spence J C H 1993 *Appl. Phys. Lett.* **62** 315–7
[325] Garcia N and Rohrer H 1989 *J. Phys.: Condens. Matter* **1** 3737
[326] Gabor D 1961 Light and information *Progress in Optics vol 1* ed E Wolf (Amsterdam: North-Holland) pp 109–53
[327] Silverman M P, Strange W and Spence J H C 1995 *Am. J. Phys.* **63** 800–13
[328] Zeitler E 1975 *Scanning Electron Microsc.* **1975** 671–8
[329] Zeitler E 1987 *Optik* **77** 13–4
[330] Spence J C H and Silverman M P 1994 *J. Vac. Sci. Technol.* A **12** 542–6
[331] Schmid H, Fink H W and Kreutzer J 1995 *J. Vac. Sci. Technol.* B **13** 2428–31
[332] Ohtsuki M and Zeitler E 1977 *Ultramicroscopy* **2** 147–8
[333] Spence J H C 1997 *Micron* **28** 101–16
[334] Binh V T 1995 *Ultramicroscopy* **58** 307–15
[335] Spence J H C 1992 *Optik* **92** 57–68
[336] Joy C and Frost B G 2004 *e-J. Surf. Sci. Nanotechnol.* **2** 81–8
[337] Spence J C H, Qian W and Melmed A J 1993 *Ultramicroscopy* **52** 473–7
[338] Spence J C H, Zhang X and Qian W 1995 *Electron Holography* ed A Tonomura *et al* (Oxford: Elsevier) pp 267–79
[339] Hanbury Brown R and Twiss R Q 1954 *Phil. Mag.* **45** 663–82
[340] Hanbury Brown R and Twiss R Q 1956 *Nature* **177** 27–9
[341] Hanbury Brown R and Twiss R Q 1956 *Nature* **178** 1447–8
[342] Hanbury Brown R and Twiss R Q 1957 *Proc. R. Soc. Lond.* **242** 300–24
[343] Hanbury Brown R and Twiss R Q 1958 *Proc. R. Soc. Lond.* **243** 291–319
[344] Mandel L 1963 *Progress in Optics* vol 2 ed E Wolf (Amsterdam: North-Holland) p 181
[345] Goldhaber *et al* 1959 *Phys. Rev. Lett* **3** 181–3

[346] Goldhaber G, Goldhaber S, Lee W and Pais S 1960 *Phys. Rev.* **120** 300–12
[347] Goldberger M L, Lewis H W and Watson K M 1963 *Phys. Rev.* **132** 2764–87
[348] Hoang T F, Cork B and Crawford H J 1982 *Z. Phys. C—Particles Fields* **12** 345–57
[349] Baym G 1998 arXiv:nucl-th/9804026v2 24 April 1998
[350] Ayala A, Baym G and Popp J L 1999 *Nucl. Phys.* A **660** 101
[351] Yasuda M and Shimizu F 1996 *Phys. Rev. Lett.* **77** 3090–3
[352] Jeltes T *et al* 2007 *Nature* **445** 402–5
[353] Rom T, Best Th, van Oosten D, Schneider U, Fölling S, Paredes B and Bloch I 2006 *Nature* **444** 733–6
[354] Purcell E M 1956 *Nature* **178** 1449–50
[355] Henny M, Oberholzer S, Strunk C, Heinzel T, Ennslin K, Holland M and Schönenberger C 1999 *Science* **284** 296–8
[356] Oliver W D, Kim J, Liu R C and Yamamoto Y 1999 *Science* **284** 299–301
[357] Yurke B 1988 *Physica* B **151** 286–90
[358] Kodama T, Osakabe N, Endo J, Tonomura A, Obaysashi K, Urakami T, Ohsuka S, Tsuchiya H, Tsuchiya Y and Uchikawa Y 1998 *Phys. Rev.* A **57** 2781–5
[359] Einstein A 1909 *Phys. Z.* **10** 185–93
[360] Kiesel H 2000 *PhD-Thesis* Universtät Tübingen (unpublished, in German)
[361] Kiesel H, Renz A and Hasselbach F 2002 *Nature* **418** 392–4
[362] Scherzer O 1980 *Optik* **56** 333–52
[363] Twiss R Q and Little A G 1959 *Aust. J. Phys.* **12** 77–93
[364] Silverman M P 1988 *OSA Proc. on Photon Correlation Techniques and Applications* vol 1 ed J B Abbiss and E A Smart (Washington, DC: OSA) pp 26–34
[365] Silverman M P 1987 *Il Nuovo Cimento* **99** 227–45
[366] Silverman M P 1987 *Phys. Lett.* A **120** 442–6
[367] Silverman M P 1986 *Phys. Lett.* A **118** 155–8
[368] Tyc T 1998 *Phys. Rev.* A **58** 4967–71
[369] Carnal O and Mlynek J 1991 *Phys. Rev. Lett.* **66** 2689–92
[370] Keith D W, Ekstrom Ch R, Turchette Q A and Prichard D E 1991 *Phys. Rev. Lett.* **66** 2693–6
[371] Shimizu F 1997 *'Atom Interferometry'* ed P R Berman (New York: Academic) p 153
Gustavson T L, Bouyer P and Kasevich M A 1997 *Phys. Rev. Lett.* **78** 2046–9
[372] Hermann K-H and Krahl D 1984 *Adv. Opt. Electron Microsc.* **9** 1–64